DISSERTATION | DOCTORAL THESIS

Titel | Title

Using the high-entropy approach to obtain multimetallic nanozymes

verfasst von | submitted by

Thương Phan Xuân MSc

angestrebter akademischer Grad | in partial fulfilment of the requirements for the degree of

Doktor der Naturwissenschaften (Dr.rer.nat.)

Wien | Vienna, 2024

Studienkennzahl lt. Studienblatt | Degree programme code as it appears on the student record sheet:	UA 796 610 449
Dissertationsgebiet lt. Studienblatt | Field of study as it appears on the student record sheet:	Pharmazie
Betreut von | Supervisor:	Univ.-Prof. Dr. Lea Ann Dailey

Acknowledgement

Pursuing a PhD is a lengthy and challenging journey, but it is also an incredible privilege. I have been fortunate to meet wonderful colleagues and friends who have made my journey a rewarding experience.

First and foremost, I would like to express my heartfelt gratitude to my supervisor, Lea Ann Dailey, for all the support you've provided both academically and personally. I still vividly remember the day you picked me up at the airport, took me to the dormitory, and helped me settle into life in Vienna. Someone once said, "It's not about how famous your supervisor is; what truly matters is how much time they dedicate to you," and Lea Ann, you have always made yourself available to every student. Thank you for your invaluable support on this project, offering great ideas and advice, and for guiding me in developing critical thinking and becoming an independent scientist. I wouldn't be where I am today without your unwavering dedication.

My journey would not be complete without acknowledging my group members and colleagues. I would like to extend special thanks to Dr. Gianluca Bello for his valuable time and advice on the experiments. I am also grateful to Dr. Ben Breitung and Dr. Simon Schweidler from Karlsruhe Institute of Technology for providing materials, and to Steffen Hirte from the University of Vienna for his insights and assistance in building computational models. A heartfelt thank you goes to all members of AG Dailey-Dr. Richard Harvey, Dr. Itziar Otazo Aseguinolaza, Dr. Gabriela Hädrich, Dr. Feng Li, My Vanessa Nguyen Hoang, Lukas Wimmer, and Jacqueline Schwarzinger-for fostering a relaxed working environment and for the enjoyable conversations and activities during lunch and other group events.

I would like to express my gratitude to my Vietnamese friends in Austria, especially Phan Canh Trinh and Le Vu Khanh Trang, for the time we spent traveling together, sharing joys and sorrows, and making my time in Europe truly unforgettable.

I am deeply thankful to my father and my aunt for their hard work in providing me with educational opportunities and for their unwavering support in every decision I've made. Finally, I want to extend special thanks to my girlfriend, My Linh, for her patience, encouragement, and acceptance of my imperfections. I'll be coming home soon.

"Con xin cảm ơn sâu sắc đến Ba và cô Hai vì đã làm việc hết sức vất vã để cho con có được cơ hội học tập cũng như luôn ủng hộ mọi quyết định của con. Cuối cùng, anh muốn dành tặng lời cảm ơn đặc biệt đến Mỹ Linh, vì đã luôn kiên nhẫn chờ đợi, động viên và chấp nhận những khuyết điểm của anh. Anh sẽ về nhà sớm thôi."

List of publications

1. Phan-Xuan, T.; Schweidler, S.; Hirte, S.; Schüller, M.; Lin, L.; Khandelwal, A.; Wang, K.; Schützke, J.; Reischl, M.; Kübel, C.; Hahn, H.; Bello, G.; Kirchmair, J.; Aghassi-Hagmann, J.; Brezesinski, T.; Breitung, B.; Dailey, L. A. Using the High-Entropy Approach to Obtain Multimetal Oxide Nanozymes: Library Synthesis, In Silico Structure-Activity, and Immunoassay Performance. *ACS Nano* **2024**. https://doi.org/10.1021/acsnano.4c03053.

2. Phan-Xuan, T.; Breitung, B.; Dailey, L. A. Nanozymes for Biomedical Applications: Multi-Metallic Systems May Improve Activity but at the Cost of Higher Toxicity? *Wiley Interdiscip Rev Nanomed Nanobiotechnol* **2024**, *16* (4). https://doi.org/10.1002/wnan.1981.

Abstract

Over the last decades, nanozymes-"nanomaterials with enzyme-like activity" have gained significant attention due to their advantages over natural enzymes such as high stability in hash conditions, simple synthesis, tunable activity and low cost. These materials have shown promise as surrogates to natural enzymes in a wide range of biomedical applications, including biosensors, antioxidant agents and anti-tumor therapeutics. Following the pioneering report of ferromagnetic Fe_3O_4 nanoparticles with intrinsic peroxidase like activity, various nanozymes have been demonstrated to mimic natural catalyst. Among the different types of nanozymes, metal and metal oxide-based nanozymes are the most widely studied. However, many of these exhibit lower catalytic reactivity than their natural counterparts, which limits their widespread use in biomedicine. To address this challenge, several strategies have been explored, with extensive investigations in integrating multiple metallic elements into a single nanoparticle. As a result, various bi- and trimetallic nanozymes with enhanced catalytic performance have emerged, some even possessing multienzyme-like activity. Recently, the high-entropy materials, i.e., complex multicomponent alloys and ceramics like oxides (five or more elements) with unique properties have found use in a numerous applications across a wide variety of field as industrial catalysts. However, their suitability as nanozymes has only recently been explored.

This study aims to use the high-entropy approach to generate multimetal oxide-based nanozymes and investigate their enzyme-like activity. Inspired by Fe_3O_4 nanoparticles with intrinsic peroxidase-mimicking activity, a library of 81 materials, in which the A and B sites of magnetite structure, $(AA')(BB'B'')_2O_4$, were substituted with up to six different cations (Cu/Zn/Mg/Fe/Cr/Mn), was created. It was revealed that increasing the compositional complexity enhanced that peroxidase-like activity. Notably, materials with modifications in both AA' and BB'B'' sites showed better catalytic performance than those with only AA' site modifications. However, substitutions of single elements also caused drastic depletion of the peroxidase-like activity. It was also observed that different methods of production might have an impact on phase property as well as catalytic reactivity. Additionally, peroxidase-like activity behaved differently toward various substrates. The mechanistic studies showed that the peroxidase-like activity resulted from the co-contribution of superoxide radicals and the electron transfer process. Based on extensive material subset data, the generalised linear model using elemental concentration, oxidation state, coordination number, interaction term and inverse spinel indicator as descriptors was developed to gain insights into the structure-activity relationship. Synergistic or antagonistic binary interactions between elements were identified. Furthermore, a single parameter, the mean interaction term, was observed to correlate highly with the catalytic activity. This parameter can be seen as quantitative indicator for the cocktail effect which is believed to

contribute to superior catalytic performance of high entropy materials. In addition, it can serve as a valuable tool for the rational design of Fe_3O_4-based multimetal nanozymes with enhance catalytic activity.

Secondly, to evaluate the feasibility of these materials for biomedicine applications, the materials were conjugated with rabbit immunoglobulin (IgG) antibodies through conventional carbodiimide conjugation, and the activity of the conjugates was determined. It was observed that surface modification with IgG did not impose negative effect on the catalytic activity. The antigen-binding sites of IgG were still preserved, presenting activity in the ELISA. Lastly, our materials also possessed the catalase-like activity as observed with various multimetal nanozyme in literature. Similarly to the peroxidase-mimicking activity, the catalase-like activity varied depending on compositions. The dual enzyme-like activity of high entropy multimetal nanozymes suggests their potential use in in-vivo applications, such as chemodynamic therapy, which will be interesting to investigate in future work.

Zusammenfassung

In den letzten Jahrzehnten haben Nanozyme – „Nanomaterialien mit enzymähnlicher Aktivität“ – aufgrund ihrer Vorteile gegenüber natürlichen Enzymen, wie hohe Stabilität unter extremen Bedingungen, einfache Synthese, anpassbare Aktivität und niedrige Kosten, erheblich an Aufmerksamkeit gewonnen. Diese Materialien haben sich als Ersatz für natürliche Enzyme in einer Vielzahl biomedizinischer Anwendungen vielversprechend gezeigt, darunter Biosensoren, Antioxidationsmittel und therapeutische Mittel gegen Tumore. Seit dem bahnbrechenden Bericht über ferromagnetische Fe3O4-Nanopartikel mit intrinsischer Peroxidase-ähnlicher Aktivität wurden verschiedene Nanozyme entwickelt, die natürliche Katalysatoren nachahmen. Unter den verschiedenen Typen von Nanozymen sind Nanozyme auf Basis von Metallen und Metalloxiden die am häufigsten untersuchten. Viele von ihnen zeigen jedoch eine geringere katalytische Reaktivität als ihre natürlichen Gegenstücke, was ihre weit verbreitete Anwendung in der Biomedizin einschränkt. Um diese Herausforderung zu bewältigen, wurden verschiedene Strategien untersucht, darunter auch die umfassende Erforschung der Integration mehrerer metallischer Elemente in ein einziges Nanopartikel. Als Ergebnis sind verschiedene bi- und trimetallische Nanozyme mit verbesserter katalytischer Leistung entstanden, von denen einige sogar eine multienzymähnliche Aktivität aufweisen. Kürzlich haben hochentropische Materialien, d.h. komplexe Mehrkomponentenlegierungen und -keramiken wie Oxide (fünf oder mehr Elemente) mit einzigartigen Eigenschaften, in zahlreichen Anwendungen in verschiedenen Bereichen als Industriekatalysatoren Verwendung gefunden. Ihre Eignung als Nanozyme wurde jedoch erst kürzlich untersucht.

Diese Studie zielt darauf ab, den Hochentropie-Ansatz zu nutzen, um Nanozyme auf Basis von Multimetalloxiden zu erzeugen und ihre enzymähnliche Aktivität zu untersuchen. Inspiriert von Fe_3O_4-Nanopartikeln mit intrinsischer Peroxidase-nachahmender Aktivität wurde eine Bibliothek von 81 Materialien erstellt, bei denen die A- und B-Stellen der Magnetitstruktur, $(AA')(BB'B'')_2O_4$, mit bis zu sechs verschiedenen Kationen (Cu/Zn/Mg/Fe/Cr/Mn) substituiert wurden. Es stellte sich heraus, dass eine Erhöhung der Zusammensetzungskomplexität die peroxidase-ähnliche Aktivität verstärkte. Insbesondere zeigten Materialien mit Modifikationen sowohl an den AA’- als auch an den BB’B’’-Stellen eine bessere katalytische Leistung als solche mit nur AA’-Modifikationen. Allerdings führten auch Substitutionen einzelner Elemente zu einem drastischen Rückgang der peroxidase-ähnlichen Aktivität. Es wurde auch beobachtet, dass unterschiedliche Herstellungsmethoden die Phaseneigenschaften sowie die katalytische Reaktivität beeinflussen könnten. Darüber hinaus verhielt sich die peroxidase-ähnliche Aktivität gegenüber verschiedenen Substraten unterschiedlich. Die mechanistischen Studien zeigten, dass die peroxidase-ähnliche Aktivität auf der Mitwirkung von Superoxidradikalen und dem Elektronentransferprozess beruhte. Basierend auf umfangreichen Materialdatensätzen

wurde ein generalisiertes lineares Modell unter Verwendung der Elementkonzentration, des Oxidationszustands, der Koordinationszahl, des Wechselwirkungsterms und des inversen Spinell-Indikators als Deskriptoren entwickelt, um Einblicke in die Struktur-Aktivitäts-Beziehung zu gewinnen. Synergistische oder antagonistische binäre Wechselwirkungen zwischen den Elementen wurden identifiziert. Darüber hinaus wurde beobachtet, dass ein einziger Parameter, der mittlere Wechselwirkungsterm, stark mit der katalytischen Aktivität korreliert. Dieser Parameter kann als quantitativer Indikator für den „Cocktail-Effekt“ angesehen werden, der zu der überlegenen katalytischen Leistung hochentropischer Materialien beiträgt. Zudem kann er als wertvolles Werkzeug für das rationale Design von Fe3O4-basierten Multimetall-Nanozymen mit verbesserter katalytischer Aktivität dienen.

Zweitens, um die Eignung dieser Materialien für biomedizinische Anwendungen zu bewerten, wurden die Materialien durch konventionelle Carbodiimid-Kopplung mit Kaninchen-Immunglobulin (IgG)-Antikörpern konjugiert, und die Aktivität der Konjugate wurde bestimmt. Es wurde festgestellt, dass die Oberflächenmodifikation mit IgG keine negativen Auswirkungen auf die katalytische Aktivität hatte. Die Antigen-Bindungsstellen von IgG blieben erhalten und zeigten Aktivität im ELISA. Schließlich besaßen unsere Materialien auch katalase-ähnliche Aktivität, wie dies auch bei verschiedenen Multimetall-Nanozymen in der Literatur beobachtet wurde. Ähnlich wie die Peroxidase-nachahmende Aktivität variierte die katalase-ähnliche Aktivität je nach Zusammensetzung. Die duale enzymähnliche Aktivität hochentropischer Multimetall-Nanozyme deutet auf ihr Potenzial für In-vivo-Anwendungen hin, wie z.B. die chemodynamische Therapie, die in zukünftigen Arbeiten von Interesse sein wird.

List of Figures

List of Tables

List of Acronyms

Acronyms	Full form
ABTS	2,2'-azinobis [3-ethylbenzothiazoline-6-sulfonic acid]-diammonium salt
BON	peroxidase-mimetic boron oxynitride
BSA	bovine serum albumin
CAT	catalase
CDs	carbon dots
DAB	3,3′-diaminobenzidine
DEPDA	N,N diethyl-p-phenylenediamine sulfate
DFT	density functional theory
DMSO	dimethylsulfoxide
EDC	1-ethyl-3-(3-dimethylaminopropyl)carbodiimide
EDX	energy dispersive X-ray spectroscopy
ELISA	enyzme linked immunosorbent assay
EuTc	europium tetracyclin
FFT	fast Fourier transform
GLMs	generalised linear models
GOx	glucose oxidase
HAADF	high-angel annular dark-field
HEMs	high entropy materials
HEPES	2-[4-(2-hydroxyethyl)piperazin-1-yl]ethane sulfonic acid
HRP	horseradish peroxidase
HR-TEM	high resolution transmission electron microscopy
IgG	immunoglobulin G
IRR	increased reaction rate
Km	Michaelis-Menten constant
LFIAs	lateral flow immunoassays
LPE	lattice potential energy
MIntE	mean interaction effect
MMNs	multimetallic nanozymes
MNPs	magnetic nanoparticles
MOPS	sodium 4-morpholine propanesulfonat salt
Na_2TA	sodium terephthalate
NHS	N-hydroxysuccinimide
NPs	nanoparticles

NSA	4-hydroxyl-1-naphthalenesulfonic acid sodium salt
ODP	o-phenylendiamine
OXD	oxidase
PBS	phosphate buffer saline
PCR	polymerase chain reaction
PIS	partial inverse spinel
POC	point-of-care
POD	peroxidase
PS-g-PEG-COOH	Polystyrene-graft-polyethylene glycol with carboxy end groups
ROS	reactive oxygen species
SAED	selective area electron diffraction
SARS-CoV-2	severe acute respiratory syndrome coronavirus 2
SAzymes	single atom nanozymes
SOD	superoxide dismutase
TA	terephthalic acid
TMB	3,3’,5,5’-tetramethylbenzidine
TME	tumor microenvironment
TRIS	trizma base
Vmax	maximum reaction velocity
WAIC	widely applicable information criterion
XRD	X-Ray Diffraction

Table of Content

Chapter 1. Introduction

(Part of this chaper has been published by Phan-Xuan et al. in *WIREs Nanomed Nanobiotechnol*[1])

1.1 Nanozymes- "Nanomaterials exhibiting enzyme-like activity"

1.1.1 Nanozyme: definition and development

Natural enzymes play an important role in biochemical reactions in every living system. In addition, these enzymes have been utilized in various fields including the food industry, pharmaceutics, biofuels, biomedical applications, etc. Several enzymes such as alkaline phosphatase, glucose oxidase, beta-galactosidase, horseradish peroxidase (HRP) have been utilized as labels in enzyme immunoassays for a long time.[2,3]Among many enzymes, peroxidases are considered to be the driving force in clinical diagnostic kits to determine glucose, creatinine, uric acid, triglycerides, etc.[4] Despite their outstanding catalytic efficiency and substrate specificity, they are vulnerable to the harsh conditions of temperature, pH and ionic strength, resulting in protein denaturation, therefore losing their function. Furthermore, the high cost of preparation, purification, and storage also hinders their practical applications. Therefore, attempts to discover other stable alternatives with similar enzymatic activities have gained a great deal of attention.

The term "nanozyme" was first mentioned in 2004 with the transphosphorylation reaction catalyzed by triazacyclonane-functionalized gold nanoparticles[5] and referred to nanomaterials with enzyme-mimicking activity. Later in 2007, the landmark article published by Gao et al. revealed the intrinsic peroxidase-like activity of magnetic nanoparticles Fe_3O_4 which is 40-fold higher than HRP at the same concentration.[6] The following years have witnessed the blossoming research in this field with a diverse range of materials, for example metal-based NPs (Au,[7] Pt,[8] Ru,[9] etc.), metal oxide-based NPs (CuO,[10] CeO_2,[11] Co_3O_4,[12] etc.), carbon-based (single-walled carbon nanotubes,[13] graphene oxide,[14] carbon nanodots,[15] etc.) and metal complex-based nanoparticles (Cu-MOF,[16] Fe-MOF,[17] etc.). **Figure 1** depicts the exponential growth of nanozyme research in term of number of publications and proportion of each enzyme-like activity.

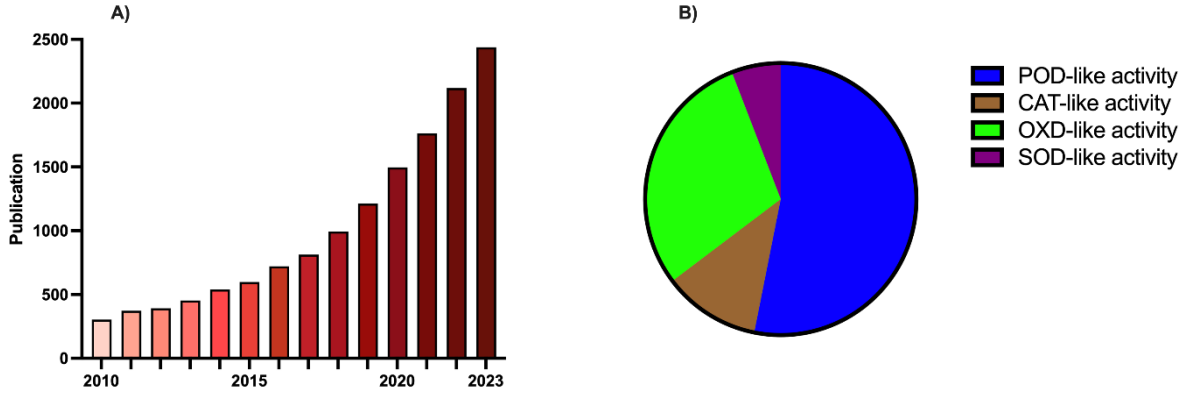

***Figure 1**. A) Number of publications in the nanozyme field from 2010 to2023. B) Proportion of the four main groups of reported enzyme-mimicking activity of nanozymes until May 2023. POD-:peroxidase, CAT-:catalase, OXD-: oxidase and SOD-superoxide dismutase. (Data was collected from Web of Science)*

Nanozymes offer several advantages over natural enzymes which makes them a topic of interest in biomedical applications (**Table 1**).

***Table 1**. Comparison between artificial nanozymes and natural nanozymes (adapted from Liang et al., Acc.Chem.Res (2021)* [18]

	Advantages	**Challenges**
Nanozymes	- highly catalytic activity - tunable catalytic activity and types - multienzyme mimicking activity - highly stable - recyclability - easy to mass produce - low cost - long term storage - robustness to harsh environment - easy to multi-functionalize (large surface area for bioconjugation) - controllable catalytic activity and types via external stimuli (such as light, ultrasound, heat, magnetic field, etc.) - unique physicochemical properties (such as fluorescence, electricity, paramagnetic properties, etc.)	- limited types of nanozymes - limited substrate selectivity - the ambiguous mechanism - size-, shape-, structure and composition-dependent catalytic activity - lack of standard and reference materials - potential nanotoxicity
Natural enzymes	- highly catalytic activity - highly substrate selectivity - good biocompatibility - wide range of biocatalysis - wide range of applications - rational design via gene and protein engineering	- high cost - limited stability - hard to store long term - hard to mass produce - time-consuming in preparation and purification - hard to use in a harsh environment (such as heat, extreme pH, salinity, UV irradiation, etc.)

1.1.2 Classification of nanozymes

Nanozymes can be categorized either based on their composition or on their enzyme-like activity. The first type of categorization includes metal oxide-based nanozymes, noble metal-based nanozymes, carbon-based nanozymes and metal-organic frameworks as the major groups. Perhaps more relevant or more often used, is the second classification method, which groups nanozymes based on their enzyme-mimicking activity. This section will therefore provide an overview of nanozymes based on their mode of activity (**Figure 2**).

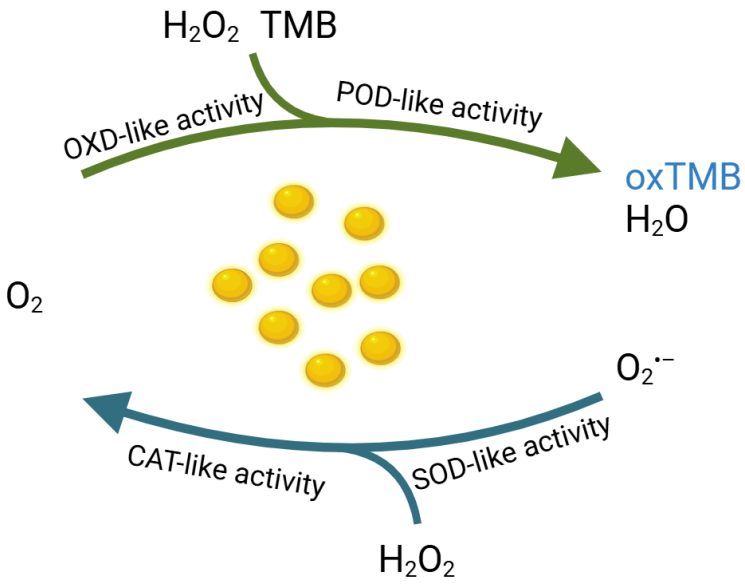

***Figure 2**. Schematic diagram of enzyme-mimicking activity of nanozymes*

1.1.2.1 Peroxidase-like activity nanozymes

Peroxidase is an enzyme that catalyzes the oxidation of substrates in the presence of hydrogen peroxides. Horseradish peroxidase (HRP) is the most well-known representative and has been used extensively in bioassays for the conversion of substrates into colored products, resulting in the detection of analytes. In 2007, Gao et al. reported the intrinsic peroxidase-like activity of Fe_3O_4 magnetic nanoparticles (MNPs) with several common substrates of HRP, including 3,3',5,5'-tetramethylbenzidine (TMB), 3,3'-diaminobenzidine (DAB) and o-phenylendiamine (OPD).[6] Further kinetics studies revealed that MNPs followed the Michaelis-Menten model similar to HRP. As a brief reminder, in Michaelis-Menten kinetics (**Figure 3**), the smaller Michaelis-Menten constant (K_m), the higher the affinity to the substrate. Interestingly, the Km value of Fe_3O_4 MNPs with TMB as the substrate was about four times lower than HRP, indicating that the Fe_3O_4 MNPs have a higher affinity for TMB than HRP. Moreover, Fe_3O_4 MNPs showed a better peroxidase activity over a wide pH (0-12) and temperature range (4-90 °C), compared to HRP, suggesting Fe_3O_4 MNPs may be suitable as a poten-

tial substitute for natural peroxidase in colorimetric assays. Since then, many different nanomaterials exhibiting peroxidase-like activity has been reported, such as Pt,[19] Cu,[20] Co_3O_4,[21] conducting polymers,[22] metal organic frameworks[23] etc.

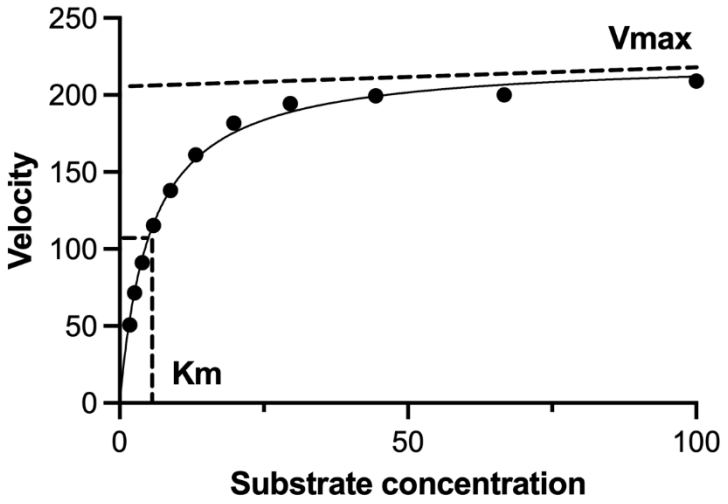

Vmax: maximum velocity
Km: Michaelis-Menten constant, a measure of the substrate binding affinity. Km is determined as substrate concentration at half Vmax

Figure 3. *Illustration of Michaelis-Menten kinetics*

1.1.2.2 Catalase-like activity

Natural catalase enzymes play a vital role in the decomposition of hydrogen peroxide into molecular oxygen and water. Both peroxidase and catalase use hydrogen peroxide as a substrate. However, no toxic reactive oxygen species (ROS) are produced in the catalase-driven reaction, which suggests this enzyme can act as an antioxidant. Catalase deficiency is associated with many diseases such as hypertension, diabetes, Alzheimer's disease, cardiovascular diseases, vitiligo, etc.[24] Up to now, many metal and metal oxide nanoparticles have been reported to exhibit catalase – like activity including Pt NPs, [25] iron oxide NPs,[26] ferrihydrite,[27] Au NPs,[28] Co_3O_4,[29] etc. The understanding of the catalase-like behavior of nanozymes is still limited. It was reported that the Ce^{3+}/Ce^{4+} ratio in ceria nanoparticles closely correlates to their catalytic activity, in other words, nanoceria can act as catalase mimetics in a redox-state dependent manner [30]. Nanoceria with higher Ce^{3+} levels did not as efficiently decompose H_2O_2 into oxygen, whereby in contrast, nanoceria with a higher proportion of surface atoms in the +4 oxidation state were catalytically active. The catalase-like activity of nanozymes was reported to be pH- and temperature dependent. Although neutral and alkaline conditions are more often more favorable, a few nanomaterials also display catalase-mimicking activity in slightly acidic environments.[31,32] The catalase-like activity of nanozymes has also been shown to follow Michaelis-Menten kinetics and many nanozymes display a higher affinity to H_2O_2 than the corresponding natural enzyme.[33]

1.1.2.3 Oxidase-like activity

Oxidase catalyzes the oxidation of substrates into oxidized products and $H_2O/H_2O_2/O_2^{\bullet-}$ in presence of molecular oxygen or other oxidizing agents.[34] In contrast to peroxidase catalysis, the reaction carried out by oxidases does not require H_2O_2. Instead, they produce H_2O_2 and in some cases superoxide radicals. Over the past few years, several nanomaterials have been reported to display oxidase-mimicking properties such as Tb_4O_7,[35] NiO,[36] Co_3O_4,[37] Pt,[38] carbon nitride,[39]etc. Several studies demonstrated that the oxidase-mimicking nanoparticles also followed the Michaelis-Menten kinetics.[40–44]

1.1.2.4. Superoxide dismutase-like activity

Superoxide dismutases (SOD) are a group of metalloenzymes that are present in most living creatures. They participate in the antioxidant defense against oxidative stress by catalyzing the dismutation of superoxide anion free radical (O_2^-) which causes cell damage into molecular oxygen and hydrogen peroxide.[45] Various nanomaterials have been reported as SOD mimics, such as Co_3O_4,[31] MnO_2,[46] CeO_2,[47] Au NPs,[48] Ag NPs.[49] Among them, ceria nanoparticles have been extensively studied.

1.1.3 Mechanism of enzyme-like activity

The mechanisms of enzyme-mimicking activity which have been reported so far include reactive oxygen species formation and electron transfer processes. In the first pathway, reactive oxygen species such as hydroxyl ($^{\bullet}OH$) and superoxide anion ($O_2^{\bullet-}$) radicals participate in the catalytic process. For example, Song et al. used electron paramagnetic resonance spectroscopy to reveal that the POD-like activity of FeS_2 NPs was attributable to the generation of $^{\bullet}OH$ radicals.[50] In reaction mechanisms involving the electron transfer process, the nanozymes act as an electron transfer mediator between TMB and H_2O_2: Specifically, nanozymes receive electrons from TMB, then transfer them to H_2O_2, resulting in oxidation of TMB. The reduction potential of the nanozymes displaying this mechanism lies in between that of TMB and H_2O_2 which facilitates electron transfer and TMB oxidation.[51] The mechanism for various enzyme-like activities is summarized in **Table 2**.

***Table 2**. Summary of reported mechanisms of different enzyme-mimicking activities*

Enzyme-like activity	**Mechanism**	**Specific functions**	**References**
POD-like activity	Reactive oxygen species (ROS) generation	Oxidation of substrates by ROS such as $^{\bullet}OH$, $O_2^{\bullet-}$ generated via Fenton, Haber Weiss reactions	50,52–54
	Electron transfer process	Enrichment and transfer of electrons without produc-	31,51,55,56

		tion (or even an inhibition) of $^{\bullet}OH$	
CAT-like activity	Adsorption activation	Accelerate the decomposition of H_2O_2 due to high adsorption energy	[57]
	Redox reaction	H_2O_2 decomposition by redox reaction	[55,58]
	Electron transfer	Redistribution of surface electron, more robust electron donating capability, lowering energy barrier for H_2O_2 decomposition	[59]
OXD-like activity	Reactive oxygen species (ROS) generation	Oxidation of substrate by ROS ($^{\bullet}OH$, $O_2^{\bullet-}$ and $^1O_2$) produced by absorbed O_2	[60–62]
	Electron transfer process	Enrichment and transfer of electrons	[63–65]
SOD-like activity	Adsorption activation	Protonation of $O_2^{\bullet-}$ and adsorption and rearrangement of $HO_2^{\bullet}$ on the metal surfaces	[66]
	Electron transfer process	Transfer of electrons between nanoparticles and $O_2^{\bullet-}$	[67]
	Eley-Rideal mechanism	Direct impingement of a gas phase atom on an absorbed species.	[68]

1.1.4 Applications of nanozymes

Owing to the high stability, low cost and unique physicochemical properties including high surface-to-volume ratio for functionalization and tunable catalytic activity, nanozymes have shown a wide spectrum of potential applications such as biosensors, antibacterial agents, anti-inflammation agents, *in vivo* imaging, cancer therapy, etc.

1.1.4.1 Nanozymes as biosensors

Nanozymes have been proven themselves as potential analytical platforms to detect various analytes. After the report of Fe_3O_4 NPs with peroxidase-like activity, a test strip based on this material was formulated and applied to detect Ebola virus. The nanozyme-strip test showed a superior sensitivity which is 100-fold higher than the standard colloidal gold strip. Furthermore, the sensitivity of the test was comparable to ELISA, but much faster and simpler.[69] The integration of nanozymes in conventional analytical platforms could be a promising tool for the detection of target substances. Indeed, the previous decade has witnessed the development of different nanozyme-based biosensors in detecting various substances ranging from metal ions, small molecules (glucose, H_2O_2) to biomolecules (proteins, nucleic acid) and pathogens (bacteria, virus) (**Table 3**).

***Table 3**. Nanozyme-based biosensors and analytical methods*

Enzyme-like activity	**Detection technique**	**Nanozyme**	**Target of interest**	**Reference**
POD	Colorimetric assay	MoS_2/N-rGO	Glucose in human blood and urine	[70]
		FO@ZMFO@FM-MOG	H_2O_2, citric acid, gallic acid, norfloxacin	[71]
		FDG20	Simazine	[72]
		IIM-Fe-SASC	H_2O_2	[73]
		Co_3O_4	Cd^{2+}	[74]
		MnFeO	Hg^{2+}	[75]
		Au	Avian influenza virus (H5N1)	[76]
		Dop-Fe_3O_4	Bacillus subtilis Escherichia coli	[77]
	Chemiluminescent assay	Co-Fe@Hemin	SARS-CoV-2 antigen	[78]
	Fluorescent assay	AuAMP NCs	Alkaline phosphatase	[79]
	Electrochemical assay	Co3O4-Au polyhedron	MiRNA-141	[80]
		MoS2 QDs@Cu NWs	Amyloid-beta oligomers	[81]

OXD	Colorimetric assay	FeMnzyme Fe-N-C SAzymes $LaMnO_{3.26}$	Ascorbic acid Ascorbic acid, glutathione T4 DNA ligase	[41] [82] [83]
	Fluorescent assay	Cu-BDC-NH_2 MnO_2	Catechol Glutathione	[84] [85]
	Electrochemical assay	Ni-MOFs h-Mn/Ni LDHs	Galantamine HBr Uracil DNA glycosylase	[86] [87]
CAT	Electrochemical assay	MB-peptide	H_2O_2	[88]
	Drainage device	AA-PtNPs	Ag(I) and Ag NPs	[89]
	Atomic flame/molecular colorimetry	PtNPs	Hela cells	[90]
SOD	Electrochemical assay	$Mn_x(PO4)_y$ modified MWCNTs	$O_2^{\bullet-}$ in HepG2 cells	[91]

1.1.4.2 Nanozymes as antibacterial agents

Nanozymes exhibiting POD and OXD-like activity can catalyze the formation of harmful ROS such as hydroxyl radicals or superoxide, and exert an antimicrobial effect. For example, Fe_3O_4 NPs with POD-like properties could decompose H_2O_2 to produce toxic $^{\bullet}OH$ for treatment of bacterial infection.[92] Similarly, Xi et al. revealed that hollow carbon spheres modified with a high content of Cu (Cu-HCSs) can trigger the death of several bacteria including *E.Coli, P.Aeruginosa, S.typhimurium* via ROS generation.[93] The antibacterial effect against methicillin-resistant *S.aureus* of Au NCs was seen as a combination of cell membrane destruction, DNA damage and ROS formation.[94] Various nanozyme platforms such as CeO_2 NPs,[95] CuO nanorods,[96] $MoSe_2$ NSs,[97] Tb_4O_7,[98] etc. were reported with bactericidal performance.

1.1.4.3 Nanozymes as anti-inflammatory agents

The overproduction of ROS is an important characteristic of chronic inflammation, resulting in redox imbalance. This can be controlled by antioxidant mechanisms which involve enzymes like superoxide dismutase, catalase and glutathione peroxidase.[99] Therefore, nanomaterials that mimic these enzymes might be potential candidates to reduce local inflammatory damage. Kim at el. utilized the dual enzyme-like activity (SOD and CAT) of CeO_2 to reduce ROS formation, preventing the initiation of

microglia and lipid peroxidation, protecting tyrosine hydroxylase to treat Parkinson's disease.[100] Mn_3O_4 nanoflowers with multienzyme-mimicking activity could modulate the cellular redox status by protecting biomolecules from protein oxidation, lipid peroxidation and DNA damage caused by ROS. In addition, these nanoflowers also protected cells from ROS-mediated inflammation injury and prevented neurological diseases caused by ROS imbalance without affecting endogenous antioxidant systems.[101,102] Similar antioxidant properties were also observed in gold-, platinum-[103] or carbon-based NPs,[104] RuO_2 NPs[105] etc.

1.1.4.4. Nanozymes as in-vivo imaging agents

By employing the unique physicochemical properties (such as fluorescence, X-ray absorption, electricity and paramagnetic properties), nanozymes have been studied for in vivo monitoring and imaging of diseases. Fan et al. achieved the visualization of tumour tissues by using the peroxidase-like activity of magnetoferritin nanoparticles without the use of any targeting ligands or contrast agents. Furthermore, these particles distinguished between cancer cells and normal cells with a sensitivity of 98% and specificity of 95% on clinical specimens.[106] Qin et al. developed Fe-coordinated carbon nanozyme dots (Fe-CDs) which showed good magnetism properties and provided promising magnetic resonance imaging of tumors with excellent biocompatibility.[107] Moreover, the discovery of multifunctional properties of nanozymes has benefited the implementation of nanozymes for multimodality imaging. For example, Tian and co-workers produced bovine serum albumin-iridium oxide NPs with catalase-mimicking activity, superior photothermal conversion efficiency and a high X-ray adsorption coefficient which provided them as promising candidate for tumor phototherapy and simultaneous photoacoustic/thermal imaging and computed tomography.[108]

1.1.4.5 Nanozymes in cancer therapy

Recently, nanozymes have been reported with therapeutic potential in oncology. The intrinsic catalytic activities of nanozymes modulated the tumor microenvironment (TME) via in situ generation of reactive species or elimination of hypoxia, resulting in an effective cancer therapy. For example, peroxidase-mimetic boron oxynitride (BON) nanoparticles could reduce the viability of 4T1 cancer cells by 82% after 48 hours of treatment by the formation of cytotoxic hydroxyl radicals. In addition, results of 14-day post treatment revealed that the tumor growth was inhibited by 97%, compared to PBS control samples.[109] In another study, Wang et al. loaded zinc phthalocyanine on $Pd@TiO_2$ to obtain PTZCs nanomotor which could decompose endogenous H_2O_2 to O_2, alleviating tumor hypoxia. Furthermore, generated O_2 could also propel PTZCs movement to expand the reach of the nanoparticles, therefore enhancing the treatment efficiency.[110]

Noble metal-containing nanomaterials are also extensively studied as photothermal agents due to their strong near IR absorption and capability to convert light to heat in photothermal therapy. For

instance, by covalent linking photosensitizer chlorin e6 (Ce6) with Fe_3O_4@C@Pt, Xu's group was able to obtain MCPtCe6 nanozymes with a high photothermal conversion efficiency. This material could effectively inhibit tumors both in vitro and in vivo as a result of the combined effect of catalytic, photothermal and photodynamic therapy.[111]

1.2 Limitations of nanozymes and how to improve performance

Despite substantial progress in nanozyme research, there are still many challenges which need to be addressed in order to widely utilize these materials in various fields, especially in biomedical applications. First, many nanozymes display lower reactivities than the corresponding natural counterparts.[112,113] Secondly, while natural enzymes have well-arranged binding pockets for accommodating substrates, nanozymes do not. As a result, they present a poor substrate specificity.[114–116] In addition, diversity in surface compositions and facet structures of nanozymes result in multiple catalytic pathways.[117,118] Therefore, improving activity and specificity of nanozymes has been a topic of interest. **Table 4** summarizes various strategies to close the gap between natural enzymes and nanozymes.

***Table 4**. Strategies to overcome limitations of nanozymes.*

Limitation	**Strategies**	**Aim**	**References**
Activity	Increasing surface-to-volume ratio or expose more active facets	More surface area for catalytic reaction	[119–121]
	Confine substrate in binding pockets	Facilitating mass transfer and minimize decomposition of intermediates	[122–124]
	Single atom approach	Atomically dispersed elements on the surface, low coordination environment, providing more active sites and facilitating charge transfer effect	[82,125–127]
	Surface modifications	Modulating surface charge/acidity/redox potential, mimicking the chemical structure of active sites in natural enzymes	[128–130]
	Incorporating (doping) more active elements	Synergistic effect of individual elements	[131–134]
	Adding cofactors	Mimicking cofactors of natural enzymes, accelerating catalytic	[135–137]

		cycles	
Specificity	Molecular imprinting polymer coating	Polymer-formed recognition cavities that can selectively bind to substrates.	[138–140]
	Enantioselective nanozymes	Modifying nanozymes with chiral ligands for enantioselective catalysis	[141–143]
	Aptananozyme reactors	Modifying nanozymes with aptamers to selectively recognise targets	[144–146]

1.3 Multi-metal doping strategy for enhanced catalytic activity

1.3.1 Recent studies in multi-metallic nanozymes

The previous section introduced various approaches to improve catalytic performance of nanozymes. Among them, metal doping has been extensively investigated and presented as an effective way to enhance the enzymatic activity of these materials. The first report by Gao et al. demonstrating the peroxidase-like effect of Fe_3O_4 nanoparticles kicked off a race to enhance the catalytic performance of this material.[6] The earliest studies used magnetite ($Fe(II)Fe(III)_2O_4$) as a starting material and substituted the ferrous iron with a different di- or trivalent cations in the spinel lattice to create bimetallic nanozymes. For example, the addition of Mn^{2+}, Co^{2+} or Cr^{3+} led to significantly higher catalytic activities compared to magnetite. However, both the choice of element and oxidation state were shown to be crucial, [147] since not all substitutions led to improved activity. In particular, Ni^{2+} had a negative impact on the activity of iron oxide-based bimetallic nanozymes. [147–149] Later studies of bimetallic nanozymes investigated both cobalt-oxide and ceria-based nanomaterials as the starting materials, among others. This was followed by multi-metallic systems incorporating up to five different metals (**Table 5**).

Table 5*. Summary of the catalytic properties of selected bimetallic/trimetallic alloys/ oxides and high entropy nanomaterials with enzyme-like activities. The Michaelis-Menten constant (Km) and the maximum velocity of an enzymatically catalyzed reaction (Vmax) are listed for various substrates (TMB: 3,3´,5,5´-tetramentylbenzidine; H_2O_2: hydrogen peroxide; OPD: o-phenylenediamine dihydrochloride; ABTS: 2,2'-azinobis [3-ethylbenzothiazoline-6-sulfonic acid]-diammonium salt; BSA: bovine serum albumin). The class of enzyme-like activity is abbreviated as peroxidase- (POD), catalase- (CAT) and oxidase-(OXD)-like, respectively.*

Materials	**Enzyme-like activity**	**Substrate**	**K_m (mM)**	**V_{max} (10^{-8} M/s)**	**Reference(s)**
Iron oxide-based NPs					

$CoFe_2O_4$	POD	TMB	0.007	0.083	[150]
		H_2O_2	0.036	0.502	
$CoFe_2O_4$	POD	H_2O_2	0.075	-	[151]
$ZnFe_2O_4$	POD	TMB	0.509	9.18	[152]
		H_2O_2	490.72	6.32	
$CuFe_2O_4$	Protease	BSA	0.380	-	[153]
		Casein	0.74	-	
$CuFe_2O_4$	POD	TMB	2.26	2.07	[154]
		H_2O_2	0.5	2.61	
Cu-$CuFe_2O_4$		TMB	0.69	16.87	
		H_2O_2	0.087	32.18	
$MnFe_2O_4$	POD	OPD	27.5	10.4	[149]
$CoFe_2O_4$			32.7	7.8	
$NiFe_2O_4$			8.4	0.86	
$ZnFe_2O_4$			22.6	0.82	
$MgFe_2O_4$	POD CAT	TMB	0.67	2.09	[155]
		ABTS	0.14	12.54	
		H_2O_2	4.61	13.46	
$NiFe_2O_4$		TMB	0.55	4.57	
		ABTS	0.46	17.48	
		H_2O_2	2.6	14.11	
$Co@Fe_3O_4$	POD	TMB	1.17	37.9	[156]
		H_2O_2	0.19	71.5	
Fe_3O_4-MnO_2	POD	TMB	0.101	0.57	[157]
		H_2O_2	0.041	2.94	
PtFe@ Fe_3O_4	POD CAT	TMB	0.213	5.477	[158]
		H_2O_2	53.55	10.78	
Fe_3O_4@SiO2@CuO	POD	TMB	3.69	47.6	[134]
		H_2O_2	9.89	202.2	
MnFeO	POD	TMB	0.11	-	[75]
		H_2O_2	0.01	-	
	OXD	TMB	0.04		
Cobalt oxide-based NPs					

Mo-Co_3O_4	POD	TMB	0.0558	9.54	[159]
		H_2O_2	22.48	5.245	
Co_3O_4/MoO_3	POD	TMB	0.0352	2.83	[160]
		H_2O_2	0.134	2.91	
Mn@ Co_3O_4	POD	TMB	0.15	5.0	[161]
		H_2O_2	0.025	2.5	
Pt@ Co_3O_4	POD	TMB	0.0705	-	[162]
$ZnCo_2O_4$	POD	ODP	0.4	5.9	[163]
		H_2O_2	0.23	4.75	
Ce-$ZnCo_2O_4$	POD	TMB	0.0886	18.796	[164]
	OXD	H_2O_2	0.553	2.618	
$CdCo_2O_4$	POD, OXD, CAT	TMB	0.317	2.19	[165]
		H_2O_2	0.325	3.75	
$NiCo_2O_4$	POD	TMB	0.23	59.665	[166]
	OXD	H_2O_2	28.33	26.773	
$NiCo_2O_4$-Au		TMB	0.1523	56.163	
		H_2O_2	13.17	29.25	
Ceria-based NPs					
Au@CeO_2	POD	TMB	0.29	3.9	[167]
		H_2O_2	44.69	2.23	
Pr-doped CeO_2	OXD	-	-	-	[168]
	Phosphatase				
Bi-doped CeO_2	Haloperoxidase	Phenol red	0.177	1.76	[169]
Cr-doped CeO_2	POD	TMB	0.08	13.8	[170]
		H_2O_2	0.867	15.9	
Fe-doped CeO2	POD	TMB	0.087	14.36	[171]
		H_2O_2	29.37	14.05	
Co-doped CeO2		TMB	0.0554	29.29	
		H_2O_2	52.88	25.06	
Mn-doped CeO2		TMB	0.1048	21.60	
		H_2O_2	59.61	12.32	
Other bimetallic and trimetallic NPs					
$Co_{1.5}Mn_{1.5}O_4$	POD	TMB	0.016	1.88	[172]

		H_2O_2	14.46	8.76	
	OXD	TMB	0.0029	1.894	
	CAT	H_2O_2	210		
	Laccase	Dopamine	0.0128	7.92	
$Cu_{1.5}Mn_{1.5}O_4$	POD	H_2O_2	1.453	714.09	[132]
Co-MnO2	Uricase	Uric acid	0.022	0.0148	[173]
LaNiO3	POD	TMB	0.105	36.2	[174]
		H_2O_2	90.05	260	
PtPdCu	POD	OPD	0.091	7.53	[175]
		H_2O_2	1	23.18	
	CAT	H_2O_2	50.172	9.62×10^{-4}	
CoAlCe	POD	TMB	0.273		[176]
		H_2O_2	32.9		
PtRuTe	POD	TMB	0.037	58.1	[133]
		H_2O_2	2.272	116.7	
PdIr	POD	TMB	0.4	89	[177]
PdPtIr	POD	TMB	0.08	31.7	[178]
		H_2O_2	4.08	85.9	
PdPt	OXD	TMB	0.058	11.4	[179]
AgPt	POD	OPD	0.129	8971	[180]
		H_2O_2	76.05	12849	
	CAT	H_2O_2	62.98	610	
FePt	OXD	TMB	0.03	1.42	[181]
Au@Pt	POD	TMB	2.431×10^{-3}	4.425	[182]
		H_2O_2	4.076×10^{-3}	6.013	
Au@Pd@Pt	POD	TMB	0.065	24.78	[131]
		H_2O_2	4.59	19.82	
Pd@Pt	POD	TMB	0.0865	6.228	[183]
		H_2O_2	2.231	5.0	
RuCu	POD	H_2O_2	0.25	0.146	[184]
CuFeMn-ATP	POD	TMB	0.046	4.3	[185]
		H_2O_2	0.14	10	
Fe_xCu_ySe	POD	TMB	1.837	12.75	[186]

		H_2O_2	8.525	4.738	
PdCuAu	POD	TMB	0.54	17	[187]
		H_2O_2	0.16	12	
High entropy NPs					
FeCuAgCeGd	POD	TMB	6.6	16.9	[188]
		H_2O_2	765	9.65	
MnFeCoNiCu	POD	TMB	0.07	6.26	[189]
		H_2O_2	0.6	16.62	
PtPdRuRhIr	POD	TMB	0.034	24.57	[190]
		H_2O_2	4094	18.82	

Since nanozyme activity follows Michaelis-Menten kinetics, most studies evaluate and report the Michaelis-Menten constant (K_m; [mM]) and the maximum velocity (V_{max}; [M/s]) of the catalyst for a defined substrate to enable comparisons with the literature. As a general rule, a lower Km and higher Vmax indicate a better performance of the nanozyme material. A comparison of the reported values for the peroxidase-like activity of the materials in **Table 5** when using TMB as a substrate provides some interesting insights (**Figure 4**). First, it should be noted that K_m values reported in the literature can vary greatly, sometimes over 2-3 magnitudes of order, making relative comparisons between literature values difficult to interpret. Secondly, it is also essential to note that the reaction temperatures used to determine K_m can also vary substantially (typically between 20-40°C)[6,191–193], which will have a distinct impact on the K_m and V_{max}. Higher reaction temperatures typically result in lower K_m values. One of the reasons for the variation in reaction temperatures is that many nanozyme systems may be designed for use in cell culture or *in vivo* models, where body temperature (37°C) represents the relevant physiological condition. In other studies, ambient room temperature may be chosen as relevant. Within this selected data set, the iron oxide-based bimetallic nanozymes generally showed a lower overall performance compared to other classes. However, this observation should be taken with caution, since **Table 5** does not include a fully comprehensive list of all nanozyme studies published in the literature.

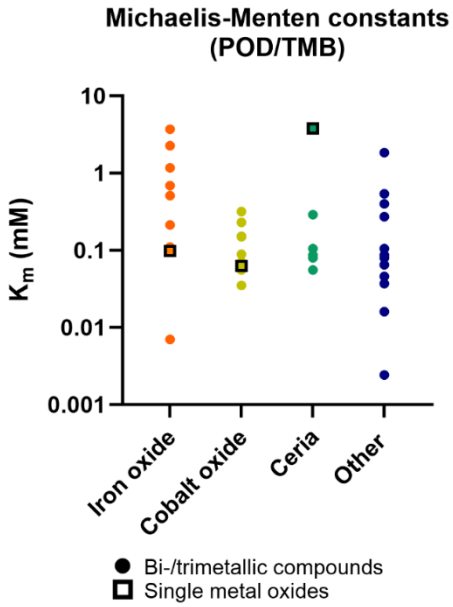

Figure 4. *Comparison of the Michaelis-Menten constants reported for selected multi-metallic nanozymes when investigated for POD-like activity using TMB as a substrate. Values are presented according to the respective groups listed in Table 5.*

1.3.2 A summary of mechanisms relevant for multi-metallic catalytic activity

Researchers investigating the effects of increasing the diversity of nanozyme composition have listed a variety of putative mechanisms which may explain enhanced catalytic performance. Doping multiple elements resulted in changes in electronic structure such as *d-band* center position, thus affecting the catalytic activity of nanozymes as it was observed by Kong and co-workers in trimetallic AuAgPd nanozymes.[194] In another study, incorporating different metals could lead to the generation of oxygen vacancies on the surface which act as active sites for effective heterogeneous catalytic reactions.[164] **Table 6** summarized investigated or postulated mechanisms which were attributed to enhanced catalytic activity as a result of multi-metallic doping.

Table 6*. Summary of various mechanisms which are responsible for improvement in enzyme-mimicking activity of multi-metallic nanozymes*

Mechanisms	**Reference(s)**
Increases in the specific surface area and the number of surface hydroxyl groups via doping with different transition metal cations	149,195,196
Oxidation state of the doped cations	197
Distribution of metal ions among tetrahedral and octahedral sites of spinel lattice	198,199
Interactions (e.g., electrostatic, π-π and coordinate interactions) and molar ratios between individual metal components	184,200–202
Number of oxygen vacancies on the surface, which act as active sites for	160,164,168,173,203–207

effective heterogeneous catalytic reactions	
Changes in the electronic structure (e.g., changes to d-band center position as a result of incorporating transition metals)	[194,208–213]
Changes in the phase structure (e.g., crystalline to amorphous transitions)	[133]

The reported mechanisms provide important insights into the impact of multi-metal doping which can be used as guide to prepare multi-metallic nanoparticles with enhanced catalytic activity. For example, cerium can be considered as a metal of choice due to its high capacity to form oxygen vacancies. Variation of elemental concentration may also be a promising strategy to modify the affinity towards a certain substrate.[194]

1.4. Multienzyme-like activity of multimetallic nanozymes

With the rapid progress and advancement of nanotechnology, nanomaterials with enzyme-mimicking activity have been gaining a great deal of attention. Various nanozymes with diverse range of catalytic properties such as peroxidase-, oxidase-, catalase- and superoxide dismutase-like activity have been unveiled.[214,215] In addition to single enzyme-mimicking activity, a variety of nanomaterials has also been reported with multienzyme-like property.[18,216] In biological systems, maintaining a proper function of the living organism usually requires the involvement of multiple enzymes. For example, several antioxidant enzymes such as CAT, SOD and glutathione peroxidase work together to build up an efficient antioxidant defense system.[217] Therefore, developing nanozymes with multiple enzyme-like activities to mimic complex natural living systems would be of interest for biomedical applications. For instance, trimetallic $AuPt_3Cu$ nanozyme with multienzyme-like property including OXD, POD and CAT triggered a cascade reaction in tumor environment, offering a remarkable chemodynamic therapy performance.[218] Various multimetallic nanomaterials possessing multifunction catalytic property have shown their potential in biomedical applications (**Table 7**).

Table 7*. Multimetallic nanozymes with bi-, tri- and tetraenzyme-like activity and their applications. The class of enzyme-like activity is abbreviated as peroxidase- (POD), catalase- (CAT), superoxide dismutase- (SOD), oxidase- (OXD) and glucose oxidase- (GOx) like activity, respectively.*

Nanozymes	**Activities**	**Application**	**Reference**
PtPdMo	CAT/POD	Brain injury repair	[219]
RhRu	CAT/POD	Osteosarcoma therapy	[220]
Fe_3O_4-Au@SiO_2	GOx/POD	Sensing	[221]
$Ce_{0.7}Zr_{0.3}O_2$	CAT/SOD	Therapeutics	[222]
ZnCe-LRH	CAT/SOD	Therapeutics	[223]
AuPd	GOx/POD	Sensing	[224]

CoO@AuPt	POD/OXD/CAT	Chemodynamic therapy	[225]
PtPdCu	CAT/POD/OXD	Sensing, antioxidant	[175]
Au@Pt	CAT/POD/OXD	Sensing	[226]
FeO_x@$ZnMnFeO_y$@Fe-Mn	CAT/POD/OXD	Sensing	[227]
PVP/IrPt	CAT/POD/OXD	Sensing	[228]
NiPd	CAT/POD/OXD	Sensing	[229]
CuPd@H-C_3N_4	CAT/SOD/OXD	Sensing	[230]
Pd@Pt	CAT/SOD/OXD	Sensing	[231]
Au/CeO_2	CAT/POD/SOD	Sensing	[167]
PtCu	CAT/POD/SOD	Therapeutics	[232]
$Cu_3V_2O_7(OH)_2.2H_2O$	POD/OXD/Laccase	Sensing	[233]
$CoFe_2O_4$/H_2PPOP	CAT/SOD/OXD/POD	Sensing	[234]
PtCu	CAT/SOD/POD/AAO	Sensing	[235]
ZIF-67/$Cu_{0.76}Co_{0.24}O_4$	SOD/POD/Glutathione POD/Laccase	Sensing	[236]
$Co_{1.5}Mn_{1.5}O_4$	CAT/POD/OXD/Laccase	Sensing	[172]

1.5 High entropy materials – An upgrade to the multi-metallic doping strategy

1.5.1 Definition and core effects

Over the last decade, high entropy materials (HEM) have been becoming as promising catalysts in a variety of applications. In essence, they are consisting of five or more cations in equimolar ratios with maximized configurational entropy $S_{config} \geq 1.5R$ (where R is the universal gas constant). What makes these materials interesting are their unique effects as a result of incorporating multiple elements, including the high entropy effect, severe lattice distortion, sluggish diffusion, and cocktail effect. These effects proved to be vital for the activity and selectivity of HEM in different catalytic reactions.[208]

Firstly, the high entropy effect plays important role in the phase stability of these materials. Generally, the phase stability of multi-metallic systems can be determined through the Gibbs free energy equation. The difference in Gibbs free energy between reactants and products (ΔG, **Equation 1**) often allows conclusions to be drawn about the stability of the formed material phase stability of multi-metallic systems.

$$\Delta G = \Delta H - T\Delta S \quad \textit{(Equation 1)}$$

where ΔG, ΔH and ΔS are changes in the Gibbs free energy, mixing enthalpy and mixing entropy, respectively and T is the thermodynamic temperature.[237] As can be seen, the Gibbs free energy is directly related to systemic enthalpy and entropy. The negative value of ΔG_{mix} suggests that the system is favorable toward a single phase with random distributions while the positive one indicates phase separation.

It is clear that when $\Delta H \leq 0$, the free energy of mixing becomes negative. However, when mixing different components with varied atomic sizes or electronegativities, ΔH becomes positive. In that case, the entropic contribution TΔS should be high enough to compensate ΔH and maintain the negative value of ΔG. The mixing entropy in an ideal case can be calculated as follow:

$$\Delta S = -R \sum x_i \ln x_i \quad \textit{(Equation 2)}$$

where R is the universal gas constant and x_i is the mole fraction of the i^{th} component. [237] It can be seen that the configurational entropy will become the driving factor for the phase stability of the multielement system at sufficiently high temperatures when including many different elements in one single phase crystal structure. The value of mixing entropy scales with the number of components and reaches the maximum value when the components are in an equimolar ratio. From a catalysis point of view, maintaining a single-phase state may be vital since the formation of phase impurities with different surface properties may interfere with the active sites which are necessary for the catalytic reaction. [238] The high entropy effect allows the miscibility of multiple components in the same lattice, taking advantage of the synergistic effect of individual components, therefore offering better catalytic performance. For example, Co and Mo are rarely miscible but the combination of these two elements is believed to be important to increase catalysis efficiency in the decomposition of ammonia. By adding another three transition metals, namely Fe, Ni, and Cu, Chao and colleagues, obtained quinary CoMoFeNiCu nanoparticles in a single solid-solution phase with 20-fold higher catalytic activity than a Ru catalyst, the most active metal for ammonia decomposition. [239]

Secondly, the incorporation of multiple components with differing atomic sizes results in an inevitable lattice distortion in high entropy materials (**Figure 4**). In addition to the atomic size differences, different bonding energy and crystal structure tendencies among constituent components are also believed to cause even higher lattice distortion because of asymmetrical binding and electronic structure between an atom and its first neighbors.[240] This deformation behavior can induce a thermodynamic nonequilibrium state,[209] which may reduce the energy barrier for the adsorption, activation, and conversion of molecules. [238] The distortion also has a significant impact on modifying the energy levels of bound intermediates [241] or changes the mechanical, electrical, thermal, optical and chemical properties of materials. [238] In high entropy oxides, this effect also produces oxygen defects which have been shown to improve the catalytic performances in various oxidation reactions. [206,207]

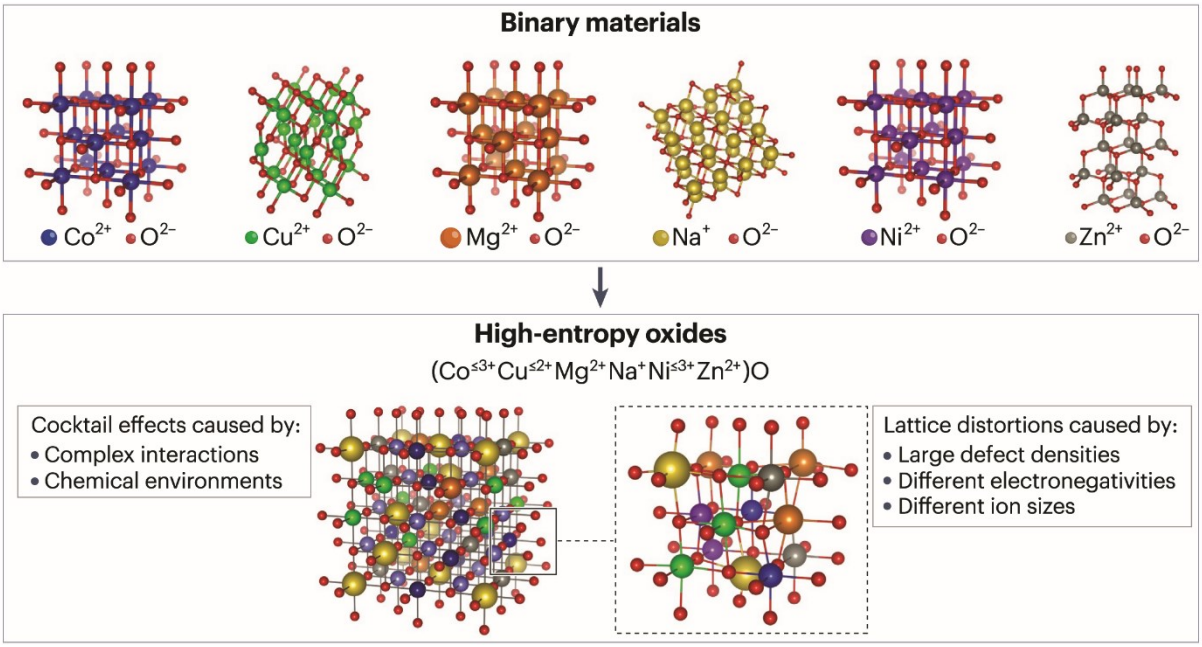

Figure 4. *Comparison of the lattice structures of six common binary materials (top panel) to the structure of a high entropy oxide comprised of equimolar concentration of the six elements (Co, Cu, Mg, Na, Ni, Zn). The complex interactions in the high entropy structure give rise to the so-called "cocktail effect", i.e., the feature that a mixture of elements results in greatly altered properties as compared with the binary materials. Further, changes in the chemical environment, crystal structure (including lattice distortions) and oxidation state have a strong effect on the material properties of HEMs. Reprinted with permission from* [242] *Copyright 2024, Springer Nature.*

Thirdly, the different diffusion rates of different types of elements, the divergence of potential energy and the change in chemical bonds trigger a lower diffusion rate of atoms in HEM than the conventional metallic alloys.[243] The higher diffusion activation energies of HEM lead to sluggish diffusion kinetics, which is considered the main driving force for enhanced mechanical, thermal, and chemical stabilities.[238,244] It is proposed that the high activation energy and the low diffusion rate are due to the large fluctuation of lattice potential energy (LPE) between crystal lattice sites.[244] A large number of low LPE sites could act as traps to hinder the atomic diffusion, resulting in the diffusion retardation effect.[208] In a study by Hu and colleagues, they performed a molecular dynamics simulation to calculate the self-diffusion coefficient of Ru element in a binary Ru-Ni alloy and a quinary system. [245] They found that Ru atoms in RuRhCoNiIr diffuse about two orders of magnitude slower than those in the bimetallic alloy, indicating the contribution of sluggish diffusion to enhanced thermal stability. In addition, the sluggish diffusion because of lattice distortion when mixing different elements can prevent phase separation and elemental segregation. [246,247]

Lastly, the "cocktail effect" (**Figure 4**) may be an essential property of the nanozyme activity of HEMs. The concept was first proposed by Ranganatha et al [248] to emphasize that the performance of multi-component systems does not simply result from the properties of individual primary components but the totality of their inter-element interactions. In other words, mixing multiple elements can offer unexpected properties which are not manifested by using a single independent component. The

cocktail effect can be considered as a complex synergetic mechanism that is attributed to the outstanding catalytic performance of HEMs. An example is the case of $TiZrHfNbTaO_{11}$ which showed better light absorbance in the visible light region than individual oxides TiO_2, ZrO_2, HfO_2, Nb_2O_5, and Ta_2O_5, which suggests this material as a potential photocatalyst.[249] However, due to the complicated multicomponent context, the mechanism of inter-element interactions is still unknown. More in-depth investigations into electronic and lattice structures may be useful to determine the underlying mechanism.

1.5.2 Multimetallic nanozymes under investigation for biomedical applications

The use of multi-metallic nanozymes (MMNs) for a variety of biomedical applications is increasing rapidly. **Table 8** provides selected examples of different applications highlighting the variety of uses of nanozymes both in *ex vivo* and *in vivo* scenarios.

Table 8. *Selected examples of ex vivo and proposed in vivo applications of multi-metallic nanozymes*

Ex vivo **applications as biosensors or diagnostics**	**Nanozyme composition**	**Reference(s)**
Lateral flow immunoassay strip to detect SAR-CoV-2 nucleocapsid protein (detection limit = 0.207 ng/ml)	Au@Pd@Pt nanozymes with peroxidase-like activity	[131]
Point-of-care detection of human dopamine (detection limit = 0.77 µM)	FeCuAgCeGd high entropy nanozymes with peroxidase-like activity	[188]
ELISA-based detection of prostate specific antigen (detection limit = 38 fg/mL which is ~ 1500-fold lower than conventional ELISA)	Pd-Ir NPs@GVs nanozymes with peroxidase-like activity	[250]
Colorimetric and amperometric detection of p53 autoantibody (detection limit = 0.08 which is ~ 1500-fold lower than p53-ELISA kit)	Au-NPFe_2O_3NC nanozymes with peroxidase-like activity	[251]
Detection of alcohol (detection limit = 0.11mM which is comparable to commercial alcohol meters)	Au@PtRu nanozyme with peroxidase-like activity	[252]
Colorimetric detection of glucose in urine (detection limit = 3 x 10^{-7} M/L)	$ZnFe_2O_4$ nanozymes with peroxidase-like activity	[253]
Colorimetric detection of glucose, H_2O_2 and ascorbic acid (detection limit = 4 µM, 15.29	MnFeCoNiCu high entropy nanozymes with peroxidase-like	[189]

μM and 28.59 μM, respectively).	activity	
Proposed *in vivo* applications as therapeutics (examples from the literature with in vivo proof-of-concept data)	**Nanozyme composition**	**Reference(s)**
Brain injury repair	PtPdMo nanozymes with multi-enzyme-mimetic activity	[219]
Combination of chemodynamic therapy, magnetic hyperthermia therapy and magnetic resonance imaging against tumor	Ir@MnFe2O4 nanozyme with peroxidase-like activity	[254]
Chemodynamic anti-tumor therapy	CoO@AuPt nanozymes with multiple catalytic activities	[225]
Chemodynamic anti-tumor therapy	$AuPt_3Cu$ nanozymes with triple catalytic activity	[218]
Photodynamic anti-tumor therapy	MnCo-Pt nanozymes with catalase-like activity	[255]
Photothermal anti-tumor therapy	PtPdRuRhIr high entropy nanozymes with peroxidase-like activity	[190]
Synergistic therapy of chemodynamic-, photodynamic- and photothermal therapy on osteosarcoma	$RhRu/Ti_3C_2T_x$ with double enzyme-like activity	[220]

1.6 Study questions and purpose

Despite the remarkable progress in nanozyme research, poor catalytic performance and lack of selectivity have constrained the applications of these materials.[256,257] The idea of incorporating different metal ions into a single structure to obtain an enhanced catalytic activity has sparked a great deal of attention. Several studies have showed that the doping of certain metal ions resulted in either the improved or depleted catalytic performance in Fe_3O_4-based bimetallic nanoparticles.[258–260] Recently, several tertiary metallic nanoplatforms, such as PtCuCo,[261] AuAgPd,[194] and PdCuAu[187] have been reported with favorable catalytic activity.

Over the last decade, high entropy nanoparticles have gained significant interest in both academia and industry due to their multielement nature and homogenously mixed solid-solution state,[262] which provides a broad compositional space for material design and property optimization. The high entropy materials with more than five components can adjust the electronic and geometric structure of conventional bimetallic or tertiary metallic nanoparticles to a larger scale to obtain catalysts with

outstanding performance.[189] Of note, due to multiple components, there are diverse atomic arrangements on the surface thus offering possibility for fine-tuning high entropy nanomaterials with maximized catalytic activity. [190] In addition, the high entropy configuration may be beneficial to overcome the immiscible gap of elements, which is an obstacle to get a homogenous elemental distribution in conventional alloy nanoparticle, therefore ensuring a homogenous elemental distribution and diverse active sites.[263] As a result, high entropy materials have been employed as efficient catalysts in various types of reactions.[239,264,265] In contrast to the extensive research in industry and energy-related fields, the feasibility study of these materials in biomedical applications is in its infancy. Recently, a few studies have revealed the enzyme-mimicking of high entropy alloy nanoparticles and their use in anti-tumor therapy, biosensing and as antibacterial agents.[188–190,266] Considering the diversity of metals including noble and transition metals which can be integrated in high entropy alloy or oxide structure, this is obviously a promising direction.

Inspired by the discovery of Fe_3O_4 nanoparticles with peroxidase-like activity and the concept of high entropy, our study aims to address the following questions:

- Can the peroxidase-mimicking activity of Fe_3O_4 be improved by incorporating multiple metal ions in octahedral (A sites) and tetrahedral (B sites) in the context of a high entropy approach?
- Which mechanisms involve in the catalytic activity of these MMNs?
- By systematically designing a large material library and using computational modelling, is it possible to obtain any structure-activity relationship which can serve as guide for rational design of MMNs with improved peroxidase-like activity?
- Is there any difference in peroxidase-like activity of MMNs with different substrate systems?
- Do MMNs also display other enzyme-like activity, for example catalase-like activity?

Chapter 2 Methodology

(Part of this chaper has been published by Phan-Xuan et al. in *ACS Nano*[267] *)*

2.1 Materials

The metal oxide precursors FeO, CuO, Fe_2O_3, MgO, Cr_2O_3, Mn_2O_3 and ZnO (purity > 99%) were purchases from Sigma-Aldrich/Alfa Aesar/ABCR GmbH and used without further purification. The nitrate salts $Cu(NO_3)_3$. 2.5 H_2O (98%), $Cr(NO_3)_3$. 9 H_2O (99.99%), $Fe(NO_3)_3$. 9 H_2O (98%), $Mg(NO_3)_3$. $6H_2O$ (99.99%), $Mn(NO_3)_3$. $4H_2O$ (98%), and $Zn(NO_3)_2$. 6 H_2O (98%), 3,3',5,5' tetramethylbenzidine (TMB), hydrogen peroxide solution 30%, dimethylsulfoxide (DMSO), trizma base (> 99%), sodium acetate trihydrate (≥ 99%), glacial acetic acid, hydrochloric acid (37%), phosphate buffer saline (PBS), 2-[4-(2-hydroxyethyl)piperazin-1-yl]ethane sulfonic acid (HEPES) buffer, 1-ethyl-3-(3-dimethylaminopropyl)carbodiimide (EDC), N-hydroxysuccinimide (NHS), bovine serum albumin (BSA), Tween 20, rabbit IgG, goat anti-rabbit IgG, terephthalic acid (TA), sodium hydroxide, and p-benzoquinone, sodium 4-morpholine propanesulfonat salt (MOPS), europium (III) chloride, tetracyclin chloride, calatase, N,N diethyl-p-phenylenediamine sulfate (DEPDA) and 4-hydroxyl-1-naphthalenesulfonic acid sodium salt (NSA) were purchased from Sigma-Aldrich. Reduced cytochrome C was purchased from Abcam. Polystyrene-graft-polyethylene glycol with carboxy end groups (PS-g-PEG-COOH) was obtained from Polymer Source, Canada.

2.2 Methods

2.2.1 Synthesis of MMN library (kindly provided by collaborators at Karlsruhe Institute of Technology)

Ball-milling method: The respective metal oxide precursors (FeO, CuO, Fe_2O_3, MgO, Cr_2O_3, Mn_2O_3, ZnO) were used in the respective molar ratios to achieve a M_3O_4 stoichiometry. The corresponding oxides were mixed and ball milled at 500 rpm for 14-26 h in Argon atmosphere, using a high-energy planetary ball-milling machine (Retsch PM 100, Retsch GmbH). The ball-to-powder weight ratio was 50:1. WC vials (50 ml in volume) and WC balls (5 mm in diameter) were used. Milling conditions were adjusted such that the particle size and therefore surface area of all materials was comparable.

Co-precipitation: the aqueous nitrate salt precursor solutions (0.2 M in distilled water) of Cu, Cr, Fe, Mg, Mn and Zn were used for the synthesis of the respective spinel oxide compounds. In total, 70 different compositions were prepared using an automated pipetting robot (opentrons OT-2). The nitrate salt solutions were mixed in different combinations in a standard 360 µL 96-well plate. To initiate co-precipitation, the respective precursor solutions were mixed with ammonia (Sigma Al-

drich, 28-30%) at a ratio of 1:2 on a carrier substrate (two-sided polished (100) Si wafers, Macor® plates) suitable for calcination and further X-Ray Diffraction (XRD) analysis. In total, 25 µL of the desired precursor solution was deposited on each the XRD carrier substrate.

For the synthesis of larger amounts (~5mg), the respective precursor solutions were mixed with ammonia into custom-made glass crucibles. During co-precipitation, a temperature of 70 °C was maintained. Finally, the samples were dried for approximately 1 h at 70 °C, then transferred to an oven and calcinated at 700°C for 5 h in air. A constant heating rate of 5 °C/min and a naturally cooling down to room temperature inside the oven were used.

2.2.2 Characterisation of MMNs

Automated X-ray diffraction (XRD) was performed by collaborators at KIT: Automated XRD measurements were performed using a STOE Stadi P diffractometer equipped with a Ga-jet X-ray source (Ga-Kβ radiation, 1.2079 Å) and a custom built XY stage for automated sample measurement. XRD patters were obtained in transmission mode. Patterns were collected between 10° and 60° 2θ with a step size of 0.02°. The powder samples on the (100) Si-wafer were fixed with Kapton folie and the Si wafer is held by an in-house designed holder. MMN crystal structure, phase purity as well as spatial elemental distribution within crystal were determined by Transmission electron microscopy (TEM), Energy dispersive X-ray spectroscopy (EDS), Selective area electron diffraction (SAED). These studies were also conducted at KIT.

Particle size**:** Hydrodynamic diameters were measured with a Malvern Zetasizer ZS Nano equipped with 633 nm laser at a scattering angle of 173° and 25 °C. Samples (10 mg) were dispersed in 10 mL distilled water and sonicated prior to measurement. The sizes reported are mean values (± standard deviations) of number distributions of three independent dispersion experiments from a single production batch of MMNs.

2.2.3 Optimization of reaction conditions for POD-like activity assay

2.2.3.1 Effect of washing on catalytic activity

$(ZnCu)(FeMnCr)_2O_4$ was dispersed in distilled water, then centrifuged at 15000 g for 5 min and subsequently resuspended with fresh water. The cycle was repeated whereby the catalytic activity of the supernatants and redispersed samples were measured.

The catalytic activity of MMNs was evaluated via a POD-like activity assay which is based on measuring the reaction rate of TMB oxidation. TMB is a well-known chromogenic peroxidase substrate i.e. horseradish peroxidase in enzyme immunodiagnostic assays. Recently, it has been widely used to investigate the peroxidase-mimicking activity of nanozymes. Upon oxidation colorless TMB is transformed into blue colored product which can be detected at its absorbance maxima of 650 nm (**Figure**

5A). Since the presence of nanozymes accelerated the reaction rate compared to the baseline (H_2O_2 only), the increase in reaction rate (IRR; min^{-1}) above the peroxide control was used to express peroxidase-like activity (**Figure 5B**).

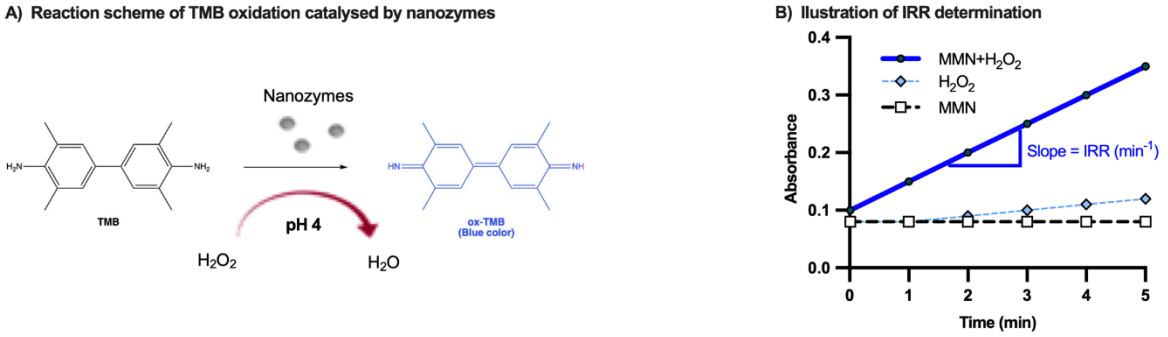

Figure 5. *A) Illustration of TMB oxidation calalysed by nanozymes withh peroxidase-like property. B) Illustration of IRR determination.*

2.2.3.2 Optimization of peroxide concentration

This step was determined in a previous study by a colleague in our group, Dr. Moritz Schüller. A TMB concentration of 800 µM was incubated with different concentrations of H_2O_2 in 0.2M sodium acetate buffer pH 4. TMB will react spontaneously with H_2O_2 without a catalyst and the reaction rate is dependent on the H_2O_2 concentration (**Figure 6**). The absorbance measured at 650 nm over 5 min. To assess the ability of nanozymes to catalyze this reaction, a H_2O_2 concentration which showed a very slow increase in the production of oxidized TMB (i.e. a flat slope for absorbance vs. time) was required. A 50 mM concentration of H_2O_2 induced a measurable TMB color development in the 5 min reaction period, but the slope was also low enough to detect increases in reaction rate resulting from nanozyme catalysis. Therefore, concentration of 50 mM was chosen for further studies.

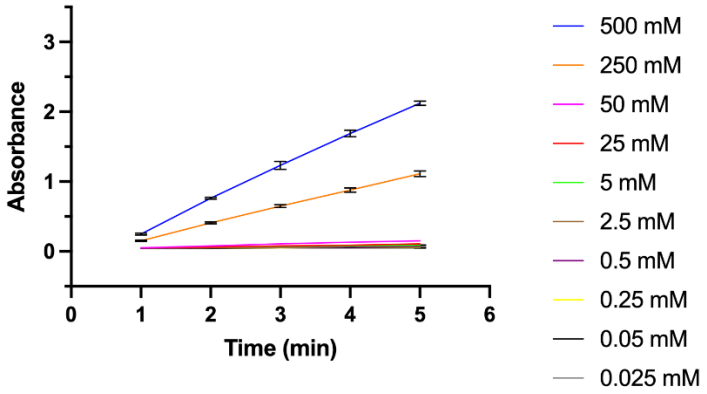

Figure 6*. Optimization of hydrogen peroxide concentration. Values present the mean ± standard deviation from n = 3 replicates*

2.2.3.3. Optimization of MMN concentration

Using the optimized concentrations of hydrogen peroxide and substrate, the MMN concentration required for measurable catalysis was investigated. $(ZnCu)(FeMnCr)_2O_4$, non-processed Fe_3O_4 and ball-milled Fe_3O_4 dispersed at concentrations of 0.4, 4 and 40 µg/mL were used to measure reaction rate. The absorbance values depicted have been corrected for background absorbance of the nanozymes at each concentration. Background samples also contained substrate but no hydrogen peroxide.

2.2.4 Catalytic activity of MMNs

Nanozymes were dispersed at 80 µg/mL in either distilled water, phosphate-buffered saline (PBS) or 50 mM Tris-HCl buffer pH 7.4, centrifuged, the supernatant removed and re-dispersed to same concentration. Washed nanozymes (100 µL) were added to a 96-well plate and then mixed with reaction solutions to get the final reaction condition (0.2M sodium acetate buffer pH 4) in which concentrations of TMB and H_2O_2 were 800 µM and 50 mM, respectively. Dye absorption was measured every minute at 650nm over 5 minutes via UV/Vis spectrophotometry (EPOCH2; Biotek). The absorbance values of control wells containing sample dispersions without H_2O_2 were subtracted from each time point to account for sample absorbance. Control wells containing H_2O_2 only (no nanozymes) were measured in parallel to determine baseline reaction rate without the catalyst. The reaction rate (min^{-1}) was calculated as the slope of the linear absorbance increase over 5 minutes. The increased reaction rate or IRR (min^{-1}) of the catalyst-mediated sample was calculated by subtracting the baseline reaction rate (H_2O_2 without catalyst) from the catalyst-mediated reaction rate. IRR (min^{-1}) values presented are the mean ± standard deviation of three independent experiments with n=4 replicates each from a single production batch.

2.2.5 Batch to batch variability and timeline stability

A second batch of selected MMNs i.e. $(ZnCu)(FeMnCr)_2O_4$ and $(ZnCuMg)(FeMnCr)_2O_4$ was produced and their catalytic activity was determined to evaluate batch to batch consistency. Stability test of MMNs i.e $(ZnCu)(FeMnCr)_2O_4$, $(FeCr)(FeCuCr)_2O_4$ and $(Fe)Fe_2O_4$ at different timepoints was also investigated.

2.2.6 Steady-state kinetics and mechanism of POD-like activity of MMNs

Steady state kinetics was investigated with $(ZnCu)(FeMnCr)_2O_4$, in comparison to Fe_3O_4 and horseradish peroxidase (HRP). The assays were carried out by varying concentrations of TMB at a fixed concentration of H_2O_2 and vice versa. The concentration of $(ZnCu)(FeMnCr)_2O_4$ and Fe_3O_4 was 40 µg/mL, concentration of HRP was 10 ng/mL. The apparent kinetic parameters, K_m and V_{max}, were obtained

by fitting data with SigmaPlot where K_m is the Michaelis constant and V_{max} is the maximum reaction velocity. A smaller K_m value indicates higher affinity between substrate and enzyme.

Hydroxyl radical detection: Terephthalic acid (TA) was used as a fluorescent probe for tracking of •OH. A standard solution of sodium terephthalate (Na_2TA) with the concentration of 0.625 mM was prepared by dissolving 10.4 mg of TA in 100 mL of NaOH (1.25 mM). 200 µL of Na_2TA solution was added into a mixture of 0.2M sodium acetate buffer pH 4 with 40 µg of MMNs and 50 mM H_2O_2. The total reaction volume was 600 µL. Then the mixture was incubated at room temperature for 8 h and the resulting solution was centrifuged prior to fluorescent measurement (Tecan Infinite M200). The excitation and emission wavelengths were 315 and 425 nm, respectively.

To investigate the impact of the radicals on the reaction rate, 50 µL of Na_2TA 0.625mM or p-benzoquinone 0.1mM (as superoxide radical scavenger) was added to reaction mixture containing 40 µg MMNs and 800 µM TMB/ 50 mM H_2O_2. Influence of radical scavengers on the reaction rate expressed as the ratio of the mean IRR without scavenger : mean IRR with scavenger.

Electron transfer process: 45 µL of reduced cytochrome C solution (1mg/mL) was added into an eppendoft, followed by the addition of 140 µL of sodium acetate buffer pH 4.0, 350 µL of MMNs dispersion (80 µg/mL) and 165 µL of distilled water. The mixture was incubated for an hour in the dark at room temperature, then centrifuged for 5 minutes at 13,000xg. Subsequently, 200 µL of supernatant was added in a 96-well plate and UV spectrum (Epoch2, Biotek) was scanned from 200 nm to 800nm. The control sample was prepared by replacing 350 µL of MMNs dispersion by distilled water.

2.2.7 Effect of surface modification on POD-like activity and ex vivo bioassay feasibility assessment

Surface modification with antibodies (Figure 7): Dispersions of selected ball-milled MMNs were prepared in PBS pH 7.4 with the addition of 0.005% polystyrene-graft-polyethylene glycol with carboxy end groups (PS-g-PEG-COOH; a surfactant used for antibody conjugation to the MMN surface). Subsequently, a solution of 5% polyethylene glycol (MW=400 Da) in water (40 µL) and 1 M 2-[4-(2-hydroxyethyl)piperazin-1-yl]ethane sulfonic acid (HEPES) buffer pH 7.4 (40 µL) was added to 1 mL MMN dispersion and mixed. A freshly prepared solution of 1% 1-ethyl-3-(3-dimethylaminopropyl)carbodiimide in water (EDC, 40 µL) and 1% 1-hydroxy-2,5-pyrrolidinedione in water (NHS, 10 µL) were then added and mixed for 5 min. Rabbit IgG (367 µL of 0.1 g/L in water) was added to the mixture and stirred for 2 h at room temperature followed by the addition of 10 µL 1% bovine serum albumin (BSA) in water. The mixture was then stirred for a further 30 min. The suspensions were washed three times by centrifugation at 15000 g for 5 min and resuspended in 2 mL PBS pH 7.4 containing 0.1% Tween 20. At the final washing step, the IgG-conjugated nanozyme dispersion was resuspended in 1 mL PBS pH 7.4 containing 0.1% Tween 20 and 0.1% BSA. The catalytic activity of IgG-conjugated dispersions was measured as described in section 2.2.4..

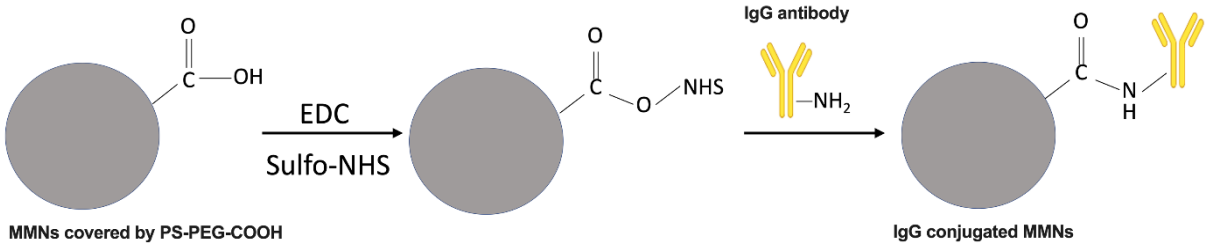

***Figure 7** . Illustration of IgG conjugation with MMNs via carbodiimide method.*

ELISA : Preparation of the ELISA plates was performed by adding 50 µL of goat anti-rabbit IgG in 0.1 M borate buffer pH 9 (20 µg/mL) to a 96-well plate and incubating at 4 °C overnight. The anti-rabbit IgG solution was aspirated and the wells were washed twice with 200 µL PBS containing 0.1% Tween 20, followed by a 2 h incubation (room temperature) with 150 µL blocking solution containing 1% BSA in PBS. Following blocking, the wells were washed twice with 200 µL PBS containing 0.1% Tween 20. To conduct the ELISA, 100 µL IgG-conjugated nanozyme samples (concentration of 500 µg/mL in PBS pH 7.4 containing 0.1% Tween 20 and 1 mg/mL BSA) were added to each well. The plate was covered, incubated at room temperature for 2 h, then washed three times with 200 µL PBS containing 0.1% Tween 20 and filled with 100 µL PBS containing 0.1% Tween 20. TMB/H_2O_2 solution (100 µL) was subsequently added to each well and the absorbance was measured at 650 nm every minute for 5 min. Controls comprised of wells containing nanozymes without addition of H_2O_2 (for background subtraction), as well as wells containing H_2O_2 but no nanozymes (for determination of baseline reaction rate). Controls without anti-rabbit IgG coating were also used as a control for non-specific binding**.** IRR (min^{-1}) values were calculated as described in the catalytic activity section.

2.2.8 Investigation the impact of inter-element interactions on POD-like activity of MMNs - a computational modelling (performed by collaborators at the University of Vienna)

Prior to modelling of the data, it was observed that the k_{cat} value (= IRR/ molar concentration of MMN) derived from the Michaelis Menten equation was a superior indicator of catalytic activity compared to the IRR itself. The reason for this resides in the method used for catalytic activity measurements which employed a nominal mass of 40 µg/mL material. Due to the different molecular weights of the respective elements in each material, 40 µg/mL equated to different molar concentrations, thus requiring the normalization of IRR with the molar concentration to remove this source of variability and improve the model performance.

The relationship between composition and normalized IRR values (i.e. k_{cat}) was explored via generalized linear models using Bambi (version 0.10.0) in Python 3. The model utilized five features including elemental concentration (E), oxidation state (O), coordination state (C), interaction term (I) and par-

tial inverse spinel indicator (PIS) as independent variables while normalized k_{cat} value collected from 41 single-phase MMNs as dependent one. The package arviz (version 0.15.1) was used to compute the estimated effective number of parameters, to compare models based on the widely applicable information criterion (WAIC) and for hypothesis testing. Model descriptors are presented as followed:

$$v_{max} = k_{cat} . [E_0]$$

$$k_{cat} \sim (\alpha, \alpha/\mu)$$

$$\log(\mu) = c_o + \sum_i c_i x_i$$

$$\alpha \sim HalfCauchy(1)$$

$$c \sim N(0,1)$$

The best model then was chosen to provide a deeper understanding about structure-activity relationship of MMNs. Based on my input as a user of the model, the research team focused on identifying a single parameter, which could be used to summarize the information from the best performing model and identify systems with high catalytic activity. The mean interaction effect (MIntE) satisfied these criteria. The MIntE was calculated using Equation 3. Since each material contains ten distinct possibilities for binary interactions and each interaction pair was characterized by multiplying its coefficient of interaction term with the individual molar concentrations of the corresponding cations with a defined oxidation and coordination state from that specific pair. The sum of these products was calculated and the exponent this value equated to the MIntE. An illustration and example calculation is provided as followed:

$$\textbf{\textit{Mean interaction effect}}\,(\textbf{\textit{MIntE}}) = e^{\sum c_{pair} \cdot [a] \cdot [b]} \quad \textbf{\textit{(Equation 3)}}$$

C_{pair}: coefficient of interaction terms

[a]: molar concentration of partner a in the interaction pair

[b]: molar concentration of partner b in the interaction pair

2.2.9. Investigation of peroxidase-like activity of MMNs in different substrate systems

Peroxidase assay was carried out with other substrates including 3,3'- diaminobenzidine (DAB) and indamine dye as described:

DAB procedure: Nanozymes were dispersed at 80 µg/mL in either distilled water, then centrifuged at 15000g. The supernatant removed and re-dispersed to same concentration. Washed nanozymes (100 µL) were added to a 96-well plate and then mixed with reaction solutions to get the final reaction condition (PBS buffer pH 7.4) in which concentrations of DAB and H_2O_2 were 800 µM and 500 mM, respectively. Dye absorption was measured every minute at 471 nm over 5 minutes via UV/Vis spec-

trophotometry (EPOCH2; Biotek). The absorbance values of control wells containing sample dispersions without H_2O_2 were subtracted from each time point to account for sample absorbance. Control wells containing H_2O_2 only (no nanozymes) were measured in parallel to determine baseline reaction rate without the catalyst. The reaction rate (min^{-1}) was calculated as the slope of the linear absorbance increase over 5 minutes. The increased reaction rate or IRR (min^{-1}) of the catalyst-mediated sample was calculated by subtracting the baseline reaction rate (H_2O_2 without catalyst) from the catalyst-mediated reaction rate. IRR (min^{-1}) values presented are the mean ± standard deviation of three independent experiments with n=4 replicates each from a single production batch.

Indamine procedure: Indamine solution was prepared by dissolving 2.6 mg of N,N diethyl-p-phenylenediamine sulfate (DEPDA) and 2.1 mg of 4-hydroxyl-1-naphthalenesulfonic acid sodium salt (NSA) in 5 mL of phosphate buffer pH 8. The peroxidase assay was carried out similarly as DAB procedure. Washed nanozymes (100 µL) were added to a 96-well plate and then mixed with reaction solutions to get the final reaction condition (phosphate buffer pH 8) in which concentrations of indamine and H_2O_2 were 800 µM and 50 mM, respectively. Dye absorption was measured every minute at 540 nm over 5 minutes via UV/Vis spectrophotometry (EPOCH2; Biotek). The absorbance values of control wells containing sample dispersions without H_2O_2 were subtracted from each time point to account for sample absorbance. Control wells containing H_2O_2 only (no nanozymes) were measured in parallel to determine baseline reaction rate without the catalyst. The reaction rate (min^{-1}) was calculated as the slope of the linear absorbance increase over 5 minutes. The increased reaction rate or IRR (min^{-1}) of the catalyst-mediated sample was calculated by subtracting the baseline reaction rate (H_2O_2 without catalyst) from the catalyst-mediated reaction rate. IRR (min^{-1}) values presented are the mean ± standard deviation of 4 replicates each from a single production batch.

2.2.10 Investigation of catalase-like activity of MMNs

Europium tetracyclin solution (EuTc) was prepared by mixing 5 mL of $EuCl_3$ solution (6.3mM) and 5 mL of tetracyclin solution (2.1mM), then the mixture was filled up to 50 mL with 10mM MOPS buffer pH 7.4. The assay was conducted as followed: 65 µL of EuTc solution, 20 µL of H_2O_2 (750mM) and 165 µL MOPS buffer were pipetted into a 96-well plate. After incubation for 15 minutes at room temperature, 50 µL of MMN dispersion (240 µg/mL) was added to obtain the final concentration of 40 µg/mL. The fluorescent intensity was recorded every 2 minute for 20 minutes (excitation and emission wavelength at 405 and 620 nm, respectively). Positive and negative control sample were prepared by replacing 50 µL of HEN dispersion by mQ water or native catalase solution (0.1mg/mL). The catalase activity was presented as mean value of decomposition rate with standard deviation obtained from 3 replicates.

2.2.11. Statistics

All the statistical analyses were performed using a one-way Analysis of Variance (ANOVA) with GraphPad Prism (10.2.3)

Chapter 3. Results and discussion

(Part of this chaper has been published by Phan-Xuan et al. in *ACS Nano*[267]*)*

3.1 MMN characterization

Precursor materials (pure metal oxides) were mixed in the desired stoichiometric ratios and ball-milled under an argon atmosphere to obtain cubic and trigonal materials with a $(AA')(BB'B'')_2O_4$ structure. Starting from magnetite $(Fe(II)Fe(III)_2O_4)$, Fe(II) in the AA' position was replaced with the divalent cations, Zn, Cu, Mg or Mn while the Fe(III) in the BB'B'' position was replaced with the trivalent ions, Mn and Cr. The stoichiometry of the elements is always equimolar; therefore, the composition of $(FeCu)Fe_2O_4$ can also be written as $Fe_{0.5}Cu_{0.5}Fe_2O_4$. In a subset of materials, such as $(FeCr)(FeCuCr)_2O_4$ we also attempted to incorporate partially trivalent ions into the A site and divalent ions into the B site, as this switch is also possible in inverse spinels (note: the oxygen content might vary accordingly). **Figure 8** shows a schematic of a magnetite inverse spinel and a high-entropy spinel (e.g. $(ZnCu)(FeCrMn)_2O_4$), whereby Zn(II) and Cu(II) replace Fe(II) and a mixture of Fe(III), Cr(III) and Mn(III) replace the Fe(III) in $(Fe)Fe_2O_4$.

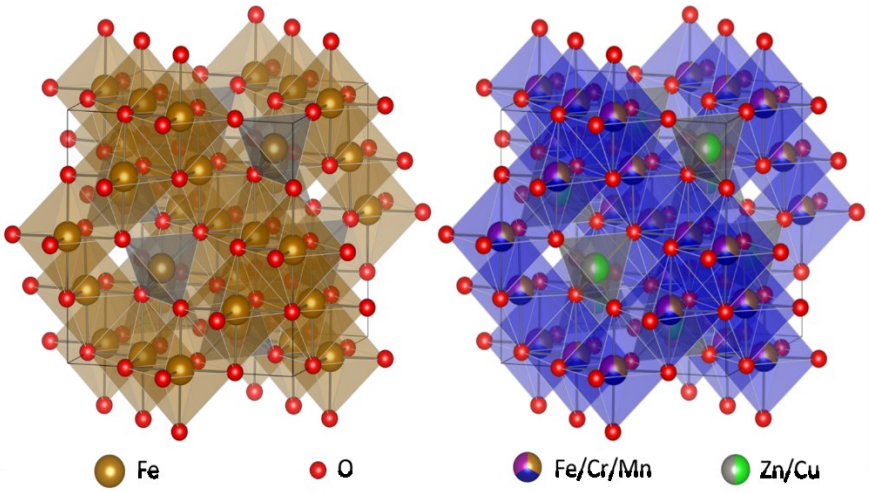

***Figure 8**. Illustration of magnetite Fe_3O_4 and selected MMN $(ZnCu)(FeCrMn)_2O_4$ structure. Adapted with permission from Phan-Xuan et al.,[267] Copyright (2024) American Chemical Society.*

Hydrodynamic diameters of ball-milled materials were measured using dynamic light scattering (DLS) and ranged from 250 to 400 nm (**Figure 9A)**. The non-processed $Fe(Fe)_2O_4$ was substantially larger (~1200 nm). The MMN crystal structure and phase purity were assessed using X-ray diffraction (XRD; **Figure 9B**) and Rietveld analysis (**Appendix**, **Figure 34**). Interestingly, the harsh ball-milling conditions changed the $(Fe)Fe_2O_4$ magnetite structure to a hematite structure after a short milling time. The same conversion was also observed with $(FeCu)Fe_2O_4$, while most of the other materials

show a spinel structure after the ball-milling procedure. Exceptions are materials $(CuMg)(FeMnCr)_2O_4$, $(CuFe)(FeMnCr)_2O_4$ and $(FeCr)(FeCuCr)_2O_4$, where a mixture of magnetite and hematite was observed. Comparing the XRD pattern of $(ZnCu)(FeMnCr)_2O_4$, with that of the non-processed magnetite reference material revealed that the reflections of the MMN are much broader compared to $(Fe)Fe_2O_4$, indicating smaller, defective crystallites resulting from the ball-milling process (**Appendix**, **Figure 34**). A slight shift of the reflections to smaller angles is observed, indicating an increase in lattice parameters and therefore a larger unit cell. This observation aligns with the larger ionic radii of the incorporated ions compared to $(Fe)Fe_2O_4$.[268]

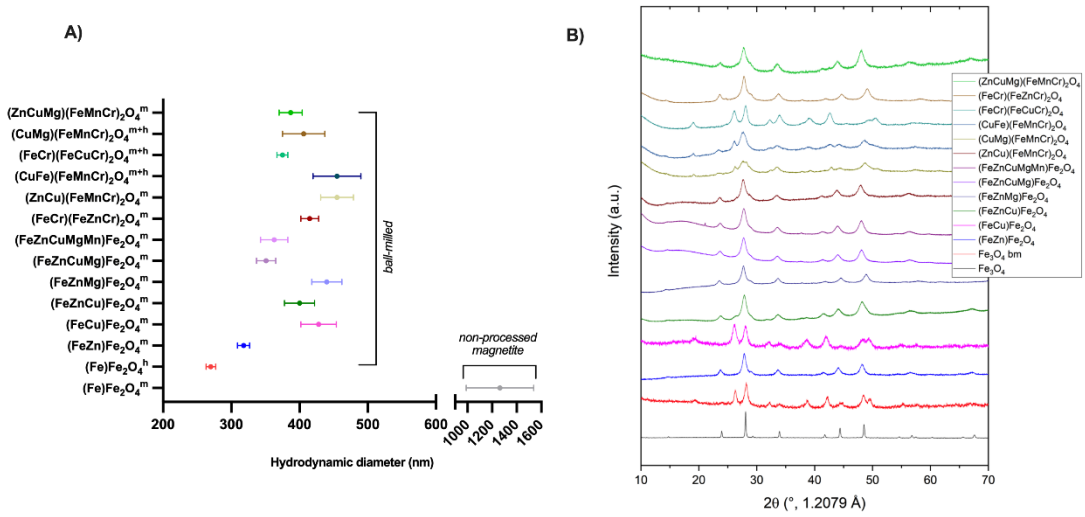

Figure 9. *(A) Hydrodynamic diameters of MMNs produced by ball-milling and measured by DLS (superscripts: m= magnetite, h=hematite, m+h= magnetite/hematite), (B) XRD patterns of non-processed $(Fe)Fe_2O_4$ and ball-milled materials (XRD data was kindly provided by collaborators at KIT). Adapted with permission from Phan-Xuan et al.,*[267] *Copyright (2024) American Chemical Society.*

High-resolution transmission electron microscopy (HR-TEM) investigations were conducted by collaborators at KIT for two materials, $(ZnCu)(FeMnCr)_2O_4$ (**Figure 10A**) and $(ZnCuMg)(FeMnCr)_2O_4$ (**Appendix, Figure 33**), revealing a high crystallinity as seen in the observable lattice planes. The observed crystallite size matches the calculated size from XRD Rietveld refinement (**Appendix, Figure 34**). The selected area diffraction (**SAED**, **Figure 10B**) confirms these findings and clearly indicates a single-phase spinel structure of high crystallinity for $(ZnCu)(FeMnCr)_2O_4$. **Figure 10C** also displays a fast Fourier transform (FFT) of the HR-TEM image in **Figure 10A**, where the d-values correspond to 2.97 and 2.53 Å for the lattice planes of a spinel structure (hkl indices: 2-20 and 1-13, respectively; in [110] zone axis orientation). Energy dispersive X-ray spectroscopy (EDX) measurements were performed in the TEM to acquire information about the spatial elemental distribution of the $(ZnCu)(FeMnCr)_2O_4$ sample. The high-angel annular dark-field (HAADF) micrograph in **Figure 10D** shows the scanned area of a single $(ZnCu)(FeMnCr)_2O_4$ particle. The subsequent colored figures de-

pict the individual elemental concentrations at a nanometer scale, whereby an increase in color intensity indicates a higher concentration of the respective element. It can be seen that Fe, Mn, Zn and O show a homogenous distribution over the entire area, while Cr distribution reveals some spatial heterogeneity with areas of higher Cr concentration. The spatial heterogeneity is even more pronounced for Cu.

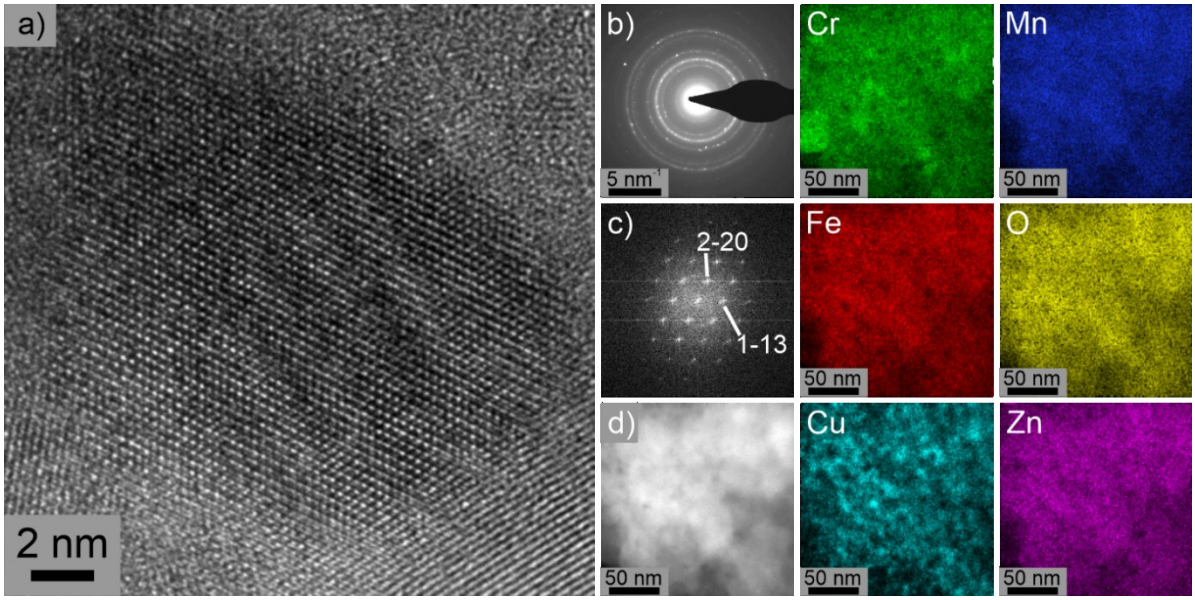

***Figure 10** . a) HR-TEM micrograph of $(ZnCu)(FeMnCr)_2O_4$. b) SAED of the $(ZnCu)(FeMnCr)_2O_4$ sample, indicating a single-phase spinel structure. c) FFT of the crystallite shown in 3a). d) HAADF micrograph and EDX images of $(ZnCu)(FeMnCr)_2O_4$ showing the elemental distribution in projection. Experiments performed by collaborators at KIT. Adapted with permission from Phan-Xuan et al.,[267] Copyright (2024) American Chemical Society.*

3.2 Optimization of catalytic activity

3.2.1 Effect of washing on catalytic activity

The activity of ball-milled samples showed a minor decrease after washing as can be seen in the drop of the TMB absorbance (red and orange lines) after washing compared to the unwashed sample (black line) (**Figure 11**). Correspondingly, the original supernatant of the nanozyme dispersion displayed a minor increase in absorbance, indicating catalytic activity in the dispersion medium (i.e. water). This was hypothesized to be due to unexpected dissolved species or contaminations resulting from synthesis method. The change in absorbance was relatively stable after one and two washing cycles and further washing did show evidence of increases in dissolved species although nanomaterial loss in the pellet was observed with increasing numbers of washing cycles. Therefore, one washing cycle was concluded to be sufficient.

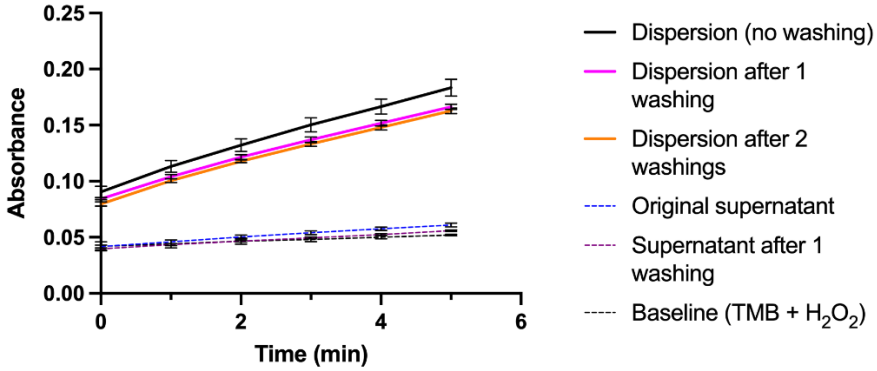

Figure 11. *Impact of preliminary washing on catalytic activity. Values present the mean ± standard deviation from n = 3 replicates.*

3.2.2 Optimization of nanozyme concentration

$(ZnCu)(FeMnCr)_2O_4$, non-processed Fe_3O_4 and ball-milled Fe_3O_4 dispersed at concentrations of 0.4, 4 and 40 µg/mL were used to measure the reaction rate in presence of 800 µM TMB and 50 mM H_2O_2. As can be seen in **Figure 12**, the concentration of 40 µg/mL of nanoparticles was sufficient to trigger a distinguishable increased reaction rate among the three materials, while lower concentrations of nanozymes were not distinguishable from the baseline. Therefore, a nanozyme concentration of 40 µg/mL was chosen for further experiments.

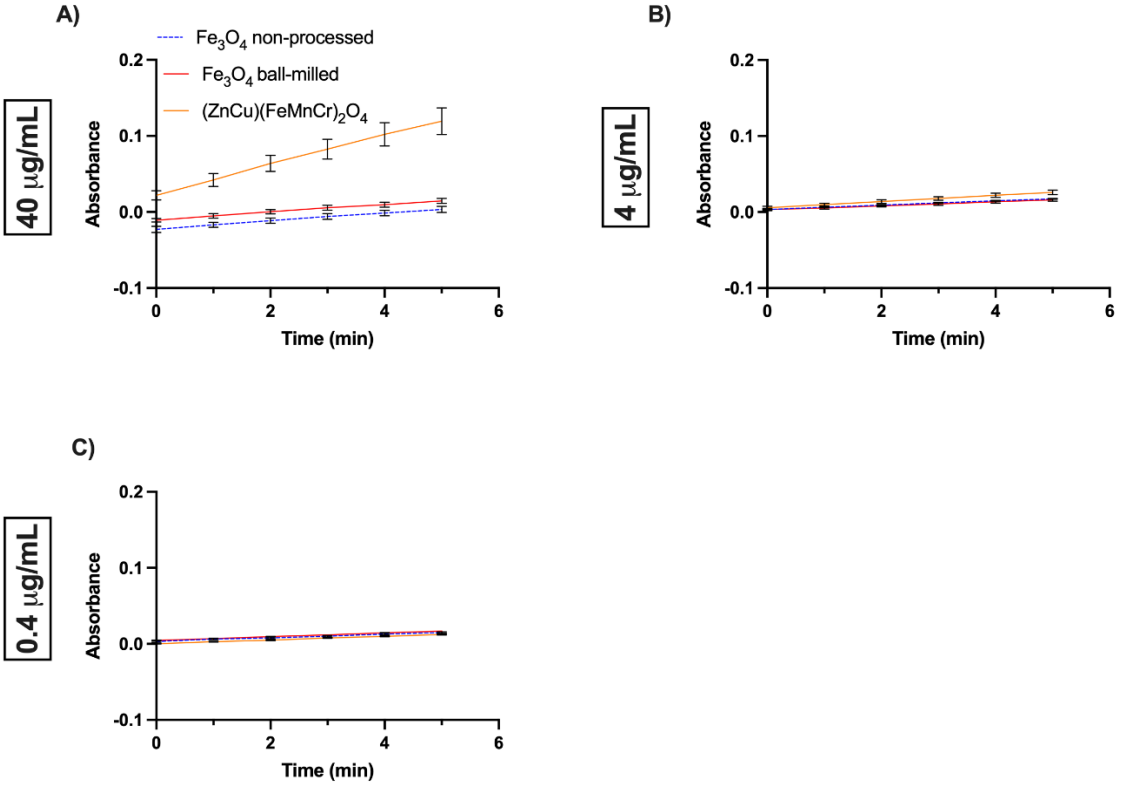

Figure 12. *Optimization of MMN concentration. Values present the mean ± standard deviation from n = 3 replicates.*

3.3 Peroxidase-like activity of MMNs

The ball-milled data set includes compositions with modification only in tetrahedral (AA') sites and compositions with modifications in both tetrahedral and octahedral (BB'B'') sites of Fe_3O_4 lattice structure. **Figure 13** showed that substitution in both AA' and BBB' sites offered a significant improvement in peroxidase-like activity compared to compared to reference $(Fe)Fe_2O_4$ nanozymes (magnetite and hematite) and MMNs with substitutions in the tetrahedral (AA') site only. The material, $(FeCr)(FeZnCr)_2O_4$, was a notable exception to this trend, showing a very low peroxidase activity. It is well-known that the incorporation of 3d transition metals into tetrahedral and octahedral sites of the spinel structure results in a significant effect on the catalytic activity towards H_2O_2.[199,258,269] Costa et al. found that the presence of Co or Mn produced a remarkable increase in reactivity in a concentration manner while Ni^{2+} ions inhibited the reaction. The authors suggested that the enhanced reactivity may result from thermodynamically favorable reduction of Co^{3+} and Mn^{3+} by Fe^{2+}. The substitution of iron cations by multivalent cations may vary the microstructure and physicochemical properties of magnetite and thus affect its surface reactivity in catalyzing advanced oxidation processes[199]. Due to the presence of multiple elements and the so-called cocktail effect in high entropy nanomaterials, the exact mechanisms of enhanced catalytic activity are still largely unknown.

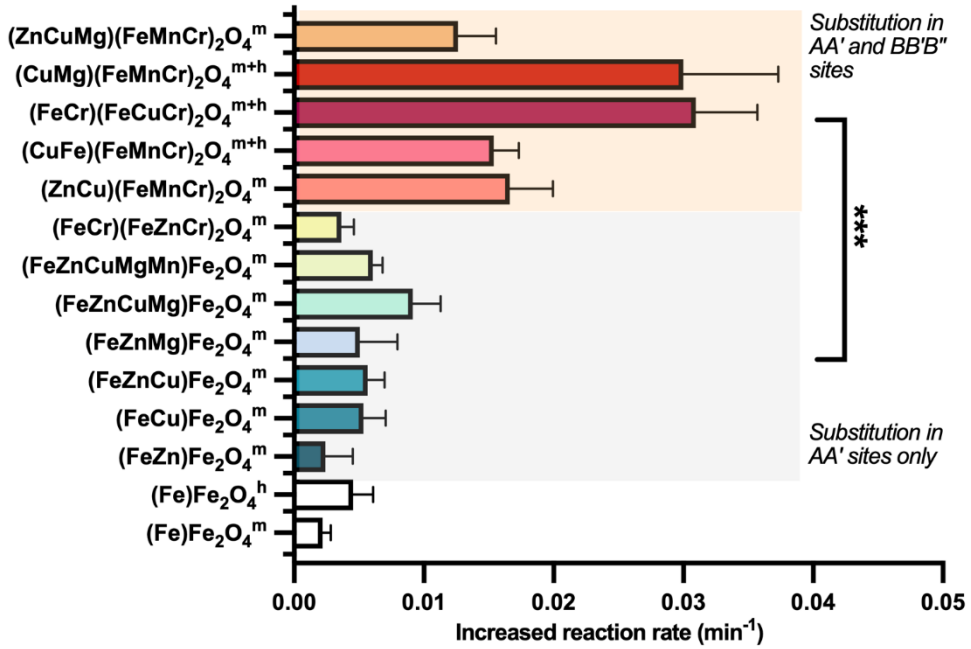

Figure 13. *IRR (min^{-1}) of non-processed $(Fe)Fe_2O_4$ and ball-milled nanozymes dispersed in water. All dispersions were prepared from a single production batch. ***p< 0.001. Superscripts: ^{m}magnetite, ^{h}hematite, $^{m+h}$magnetite+hematite. Values present the mean ± standard deviation from n = 12 replicates. Adapted with permission from Phan-Xuan et al.,[267] Copyright (2024) American Chemical Society.*

A further important observation was that copper ions were present in all materials with enhanced peroxidase-like activity. The catalytic activity of copper ions was expected since CuO NPs were shown to outperform other transitional metal oxide NPs in term of POD-like activity.[270] However, the concentration of copper ion in these compounds is not directly proportional to the catalytic activity. For example, $(ZnCu)(FeMnCr)_2O_4$ and $(CuMg)(FeMnCr)_2O_4$ have the same amount of copper ions but the latter possessed a higher catalytic activity. Another example is $(FeCu)Fe_2O_4$ and $(FeZnCu)Fe_2O_4$, which are similar in catalytic efficiency even though $(FeCu)Fe_2O_4$ contains a higher concentration of copper. This suggests that although copper may play an important role in POD-like activity of MMNs, the contribution of other ions cannot be underestimated.

Since CuO NPs also displayed peroxidase-mimicking activity,[270] it may be asked whether the high activity of multiple phase materials i.e $(FeCr)(FeCuMn)_2O_4$ might result from CuO enriched materials present as an impurity. Therefore, a control experiment was conducted with ball-milled CuO, $(FeCr)(FeCuMn)_2O_4{}^{m+h}$ and $(ZnCu)(FeMnCr)_2O_4{}^{m}$. **Figure 14A** shows that at equimolar copper concentrations, the peroxidase-like activity of CuO is significantly lower than MMNs with synergistic elemental compositions, confirming the undeniable role of other ions in the enhanced catalytic activity of MMNs.

It was further questioned whether the catalytic activity of copper-containing MMNs could result from the leaching of copper ions into the dispersion medium. To test this, $(FeCr)(FeCuMn)_2O_4{}^{m+h}$ particles were incubated in H_2O for 2h, then the MMNs were separated from the supernatant by centrifugation and the POD assay was carried out with supernatant. As depicted in **Figure 14B**, the $(FeCr)(FeCuMn)_2O_4{}^{m+h}$ supernatant (distilled water) showed no activity, confirming that the observed POD-like activity of MMNs was attributed to the intact particles, which is in agreement with previous studies.[6,150,253]

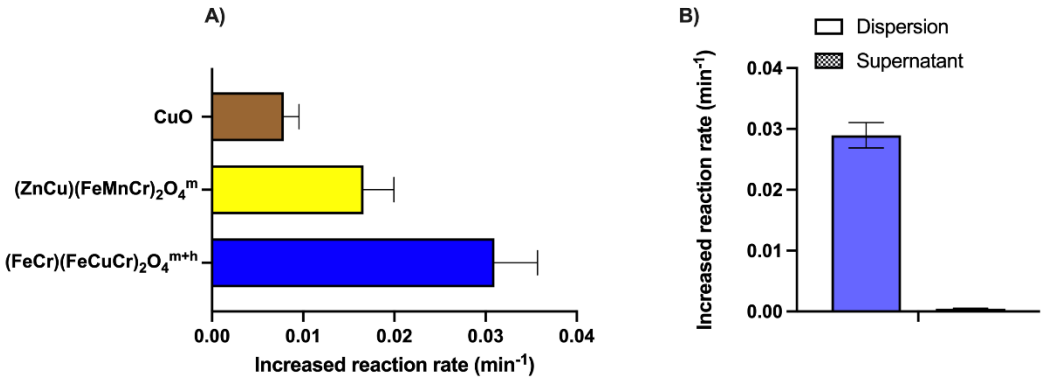

***Figure 14**. (A) Catalytic activity of $(FeCr)(FeCuMn)_2O_4{}^{m+h}$ and $(ZnCu)(FeMnCr)_2O_4{}^{m}$ in comparison with ball-milled CuO with the same Copper content. (B) Leaching experiment of $(FeCr)(FeCuMn)_2O_4{}^{m+h}$ in distilled water. Values represent the mean ± standard deviation from n = 3 replicates.*

3.4. Effect of buffers and temperature on catalytic activity

In many biomedical applications, nanozymes may be surface-modified via conjugation with biomolecules, e.g., antibodies, and stored in different buffer systems. Since some buffer components, such as phosphates, may react with different surface cations and modulate the catalytic activity, the POD activity of MMNs was also evaluated in TRIS pH 7.4 and PBS pH 7.4, and compared with activity in distilled water. As depicted in **Figure 15**, TRIS and PBS buffer showed a tendency to reduce the catalytic activity compared to water, which might be due to capping effect of these buffer to metallic ions in MMNs.[271–273] Indeed, it was observed that the peroxidase-like activity of Fe_3O_4 nanoparticles was decreased in PBS buffer.[274] This might be due to strong affinity of phosphates to iron ions on the nanoparticle surface, resulting in the formation of strong bidentate Fe-O-P bonds, thus decreasing the catalytic activity.[275] Similarly, TRIS buffer can interact with various transition metal ions to form a strong complexation,[276] leading to the reduced reactivity of MMNs. Distinct trends, however, were not observed and PBS was chosen for experiments, where surface modification with antibodies was performed.

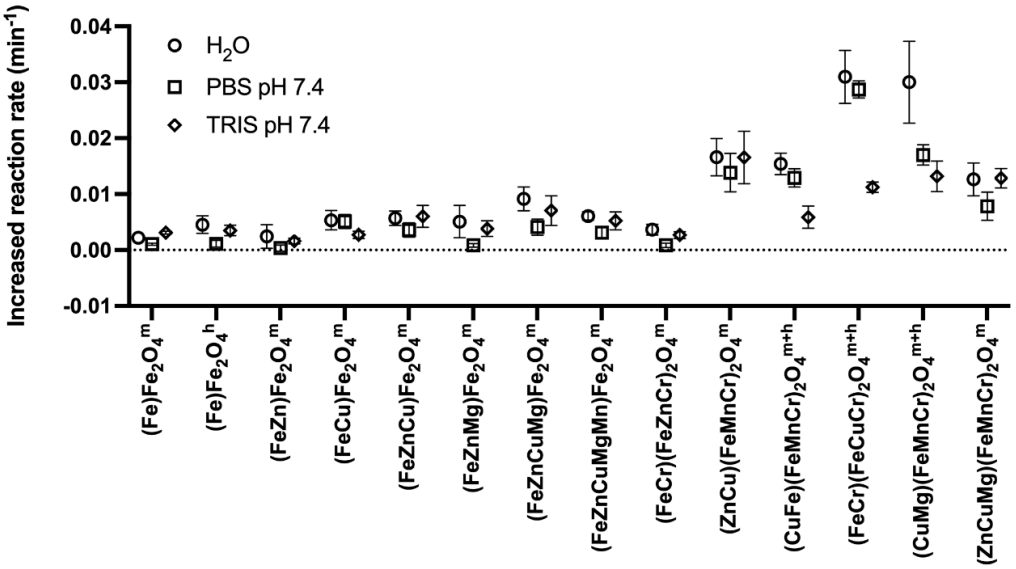

***Figure 15**. Effect of buffers on peroxidase-like activity of ball-milled MMNs. Values represent the mean ± standard deviation from n = 12 replicates.*

The effect of temperature on the catalytic activity was also determined with $(FeCr)(FeCuMn)_2O_4$ and the native HRP enzyme. As can be seen in **Figure 16**, the HRP activity decreased at elevated temperatures while $(FeCr)(FeCuMn)_2O_4$ exhibited a higher thermal stability, preserving over 90% of its catalytic performance over a wide range of temperatures.

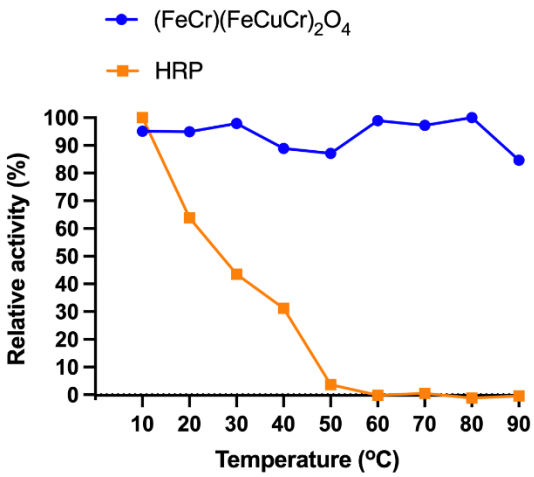

Figure 16. *Effect of temperature on catalytic activity of selected MMN and horseradish peroxidase (n=1).*

3.5. Batch-to-batch variability and storage stability

To evaluate batch consistency in catalytic performance which is also essential for clinical translation of MMNs, the second batch of selected MMNs $(ZnCu)(FeMnCr)_2O_4$ and $(ZnCuMg)(FeMnCr)_2O_4$ was produced by ball-milling and catalytic activity was compared to that of the first batch. **Figure 17A** showed there was about 20% variation in catalytic activity between two batches.

The storage stability of $(ZnCu)(FeMnCr)_2O_4$ and Fe_3O_4 was also investigated. Both MMNs and reference Fe_3O_4 showed no significant loss in catalytic activity over 16 months storage in the dry state at ambient room temperature (**Figure 17B**). The catalytic activity of Fe_3O_4 nanoparticles was reported to progessively decrease with time. However, this occcured after a prolonged catalysis due to the transformation of Fe_3O_4 into γ-Fe_2O_3 with lower peroxidase-like activity.[277] In addition, Fe_3O_4 can be gradually oxidized to Fe_2O_3 when exposed to atmosphere oxygen. The dry state and sealed storage conditions employed in our study may prevent this transformation, thus a stable reactivity of Fe_3O_4 was preserved. Furthermore, due to the high configuration entropy effect of MMNs, these materials may possess a high mechanical and thermal stability, in addition to oxidation and corrosion resistance,[278,279] therefore a high storage stability.

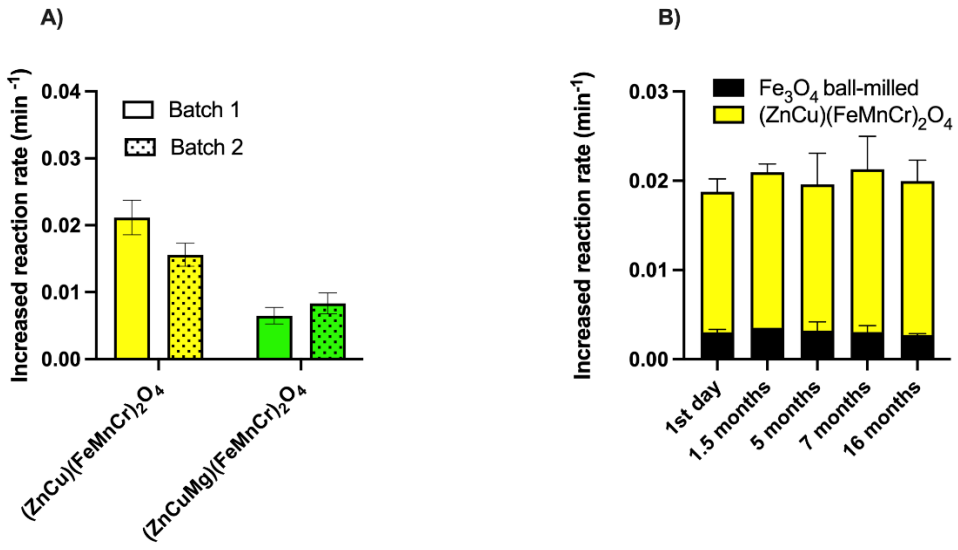

***Figure 17**. (A) Batch to batch activity variability of $(ZnCu)(FeMnCr)_2O_4$ and $(ZnCuMg)(FeMnCr)_2O_4$. (B) Storage stability of $(ZnCu)(FeMnCr)_2O_4$ and Fe_3O_4. Values represent the mean ± standard deviation from n = 3 replicates.*

3.6 Steady state kinetics and mechanism of POD-like activity of MMNs

3.6.1 Michaelis-Menten kinetics

Two ball-milled materials, $(Fe)(Fe)_2O_4^h$ and $(ZnCu)(FeMnCr)_2O_4^m$ and a co-precipitated material $(FeCu)(MgCrMn)_2O_4^a$ were chosen for in-depth analysis of Michaelis-Menten kinetics (**Figure 18**). The obtained values for the Michaelis-Menten constants (K_m) and maximum reaction velocity (V_{max}) are summarized in **Table 9**. As explained in the introduction, a small K_m indicates a higher affinity for the substrate, while a high V_{max} denotes a rapid reaction rate. As can be seen in **Figure 18A-C**, MMNs can accelerate the reaction at a faster pace than the reference iron-oxide nanoparticles and native HRP. Introducing different elements into the lattice sites resulted in varied K_m values, thus different levels of affinity to substrates. For example, while $(ZnCu)(FeMnCr)_2O_4^m$ and $(FeCu)(MgCrMn)_2O_4^a$ showed similar affinity toward TMB, the latter displayed a 7.5-fold higher affinity than the former toward H_2O_2 as a substrate (**Table 9**).

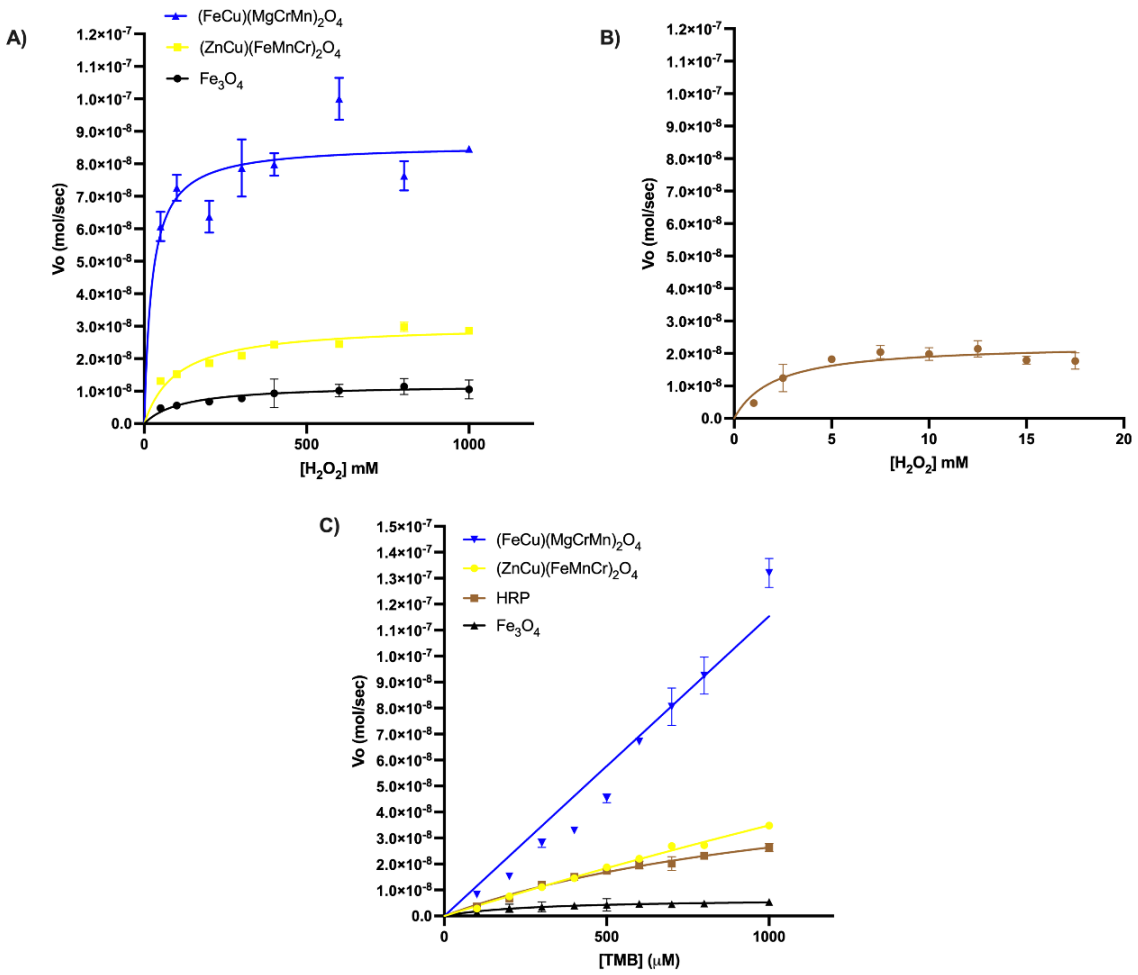

***Figure 18**. Steady-state kinetic assay. A) Assessment of nanozyme affinity to H_2O_2 as a substrate. The concentration of TMB was 800μM and the H_2O_2 concentration was varied (50-1000 mM). B) Assessment of HRP affinity to H_2O_2 as a substrate. The concentration of TMB was 800μM and the H_2O_2 concentration was varied (1-17.5 mM).C) Assessment of nanozyme and HRP affinity to TMB as a substrate. The concentration of H_2O_2 was 500 mM for all three nanozymes and 10 mM for HRP while the TMB concentration was varied (100-1000 μM). Values represent the mean ± standard deviation from n = 3 replicates.*

***Table 9.** Apparent Michaelis-Menten constant (K_m) and maximum reaction rate (V_{max}) of MMNs in comparison with $Fe(Fe)_2O_4$ and HRP towards TMB and H_2O_2 as substrates.*

	Substrate	K_m (mM)	V_{max} (10^{-8}M/sec)
$(ZnCu)(FeMnCr)_2O_4$	TMB	0.624	4.99×10^{-8}
	H_2O_2	290	4.07×10^{-8}
$(FeCu)(MgCrMn)_2O_4$	TMB	0.623	1.46×10^{-7}
	H_2O_2	38.57	9.03×10^{-8}
$Fe(Fe)_2O_4$	TMB	0.303	6.86×10^{-9}
	H_2O_2	322	1.6×10^{-8}

HRP	TMB	0.398	3.21×10^{-8}
	H_2O_2	2.07	2.29×10^{-8}

In order to enable comparisons of performance with other iron oxide-based nanozymes reported in the literature (**Figure 19**),[154,253,280,281] the Michaelis-Menten constant (K_m) and the maximum reaction velocity (V_{max}) were chosen as representative kinetic parameters for this comparison, since these are the most commonly reported values in POD-like nanozyme studies. The literature values reported were taken from a review by Zhang *et al*,[282]. The summary in **Figure 19** highlights that the reported K_m and V_{max} values (determined for both TMB and H_2O_2 as substrates) vary considerably in magnitude across the literature. This variation likely results from the wide range of reaction temperatures employed in different studies (e.g., ambient room temperature to 40°C)[6,191–193]. Since K_m and V_{max} can be dramatically affected by reaction temperature, the variation is not unexpected. The K_m and V_{max} calculated for the ball-milled $(Fe)(Fe)_2O_4{}^{h}$, $(ZnCu)(FeMnCr)_2O_4{}^{m}$ and co-precipitated $(FeCu)(MgCrMn)_2O_4{}^{a}$ in this study align with reported values in the literature, albeit in the lower affinity/velocity range. However, since all reactions performed in this study were conducted at ambient room temperature; 22-25°C), the results make sense within this context.

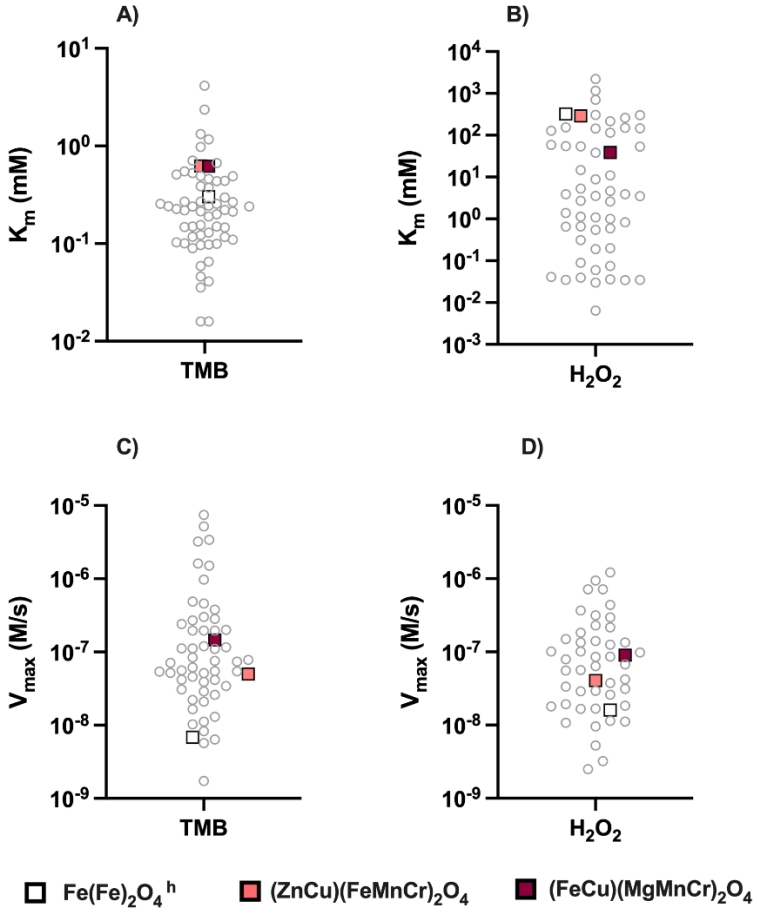

***Figure 19**. Comparison of the Michaelis-Menten parameters. A, B) K_m (mM) and C, D) V_{max} (M/s) with literature values summarized by Zhang et al [282] . It is important to note that the reaction temperature*

of the cited studies varied from ambient room temperature to ~40°C, which accounts for the high variation in the cited parameters.

3.6.2 Catalytic mechanism in POD-like activity of MMNs: the involvement of reactive oxygen species and electron transfer process

It has been reported that ROS, such as hydroxyl radicals (•OH) and superoxide radicals ($O_2^{\bullet-}$), are involved in the oxidation of TMB when catalyzed by nanozymes with peroxidase-like activity.[50,53,54] To identify the impact of generated active species on the reaction rate, terephthalic acid and p-benzoquinone were used as scavengers of •OH and $O_2^{\bullet-}$ radicals, respectively. Terephthalic acid reacts with •OH to produce a highly fluorescent derivative. As can be seen, nearly all MMNs with high catalytic activity also generated significant amounts of •OH (***Figure 20*A**), with the exception of $(FeCr)(FeCuCr)_2O_4$, which exhibited one of the highest IRR values, but had a 51-fold lower •OH generation (expressed as area under the fluorescence curve) than the most active MMN, $(CuMg)(FeMnCr)_2O_4$. Further experiments were conducted with and without the •OH scavenger, terephthalic acid. It was hypothesized that presence of the •OH scavenger would inhibit the catalysis and thereby reduce the reaction rate. The ratio of the IRR with scavenger:without scavenger can then be used to determine the impact of •OH on the catalysis process. A ratio of 1 means the IRR values are the same with and without scavenger, meaning that generation of •OH did not play a role in the POD-like activity. In contrast, a ratio > 1 indicated that •OH played a role in the catalysis. As can be seen in ***Figure 20*B (circles)**, •OH intermediates did not play a major role in the catalytic activity of nearly all materials tested. In contrast, the presence of the superoxide radical scavenger, p-benzoquinone, did show a remarkable decrease in IRR (min^{-1}) for many of the ball-milled materials, implying a significant role of $O_2^{\bullet-}$ radicals in TMB oxidation (***Figure 20*B; triangles)**

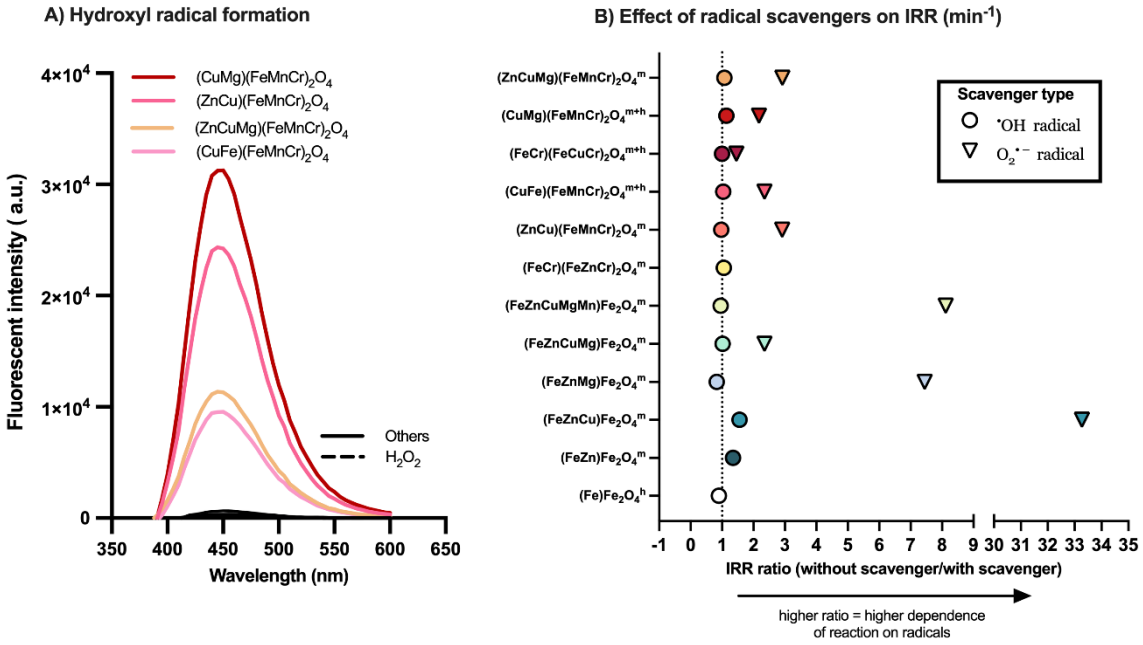

***Figure 20**. (A) Hydroxyl radical formation detected using terephthalic acid fluorescence emission as a quantitative measure of radical generation (n=3). (B) Influence of radical scavengers on the reaction rate expressed as the ratio of the mean IRR without scavenger : mean IRR with scavenger (n=3). Values > 1 indicate that the radical plays a mechanistic role in the reaction. Adapted with permission from Phan-Xuan et al.,[267] Copyright (2024) American Chemical Society.*

In the two most catalytically active materials, the POD-like activity may also be attributed to electron transfer processes. Electron transfer is typically determined using the reduced form of cytochrome C as a marker, since oxidation via electron transfer results in a dramatic shift in the absorbance spectrum (**Figure 21A**). Cytochrome C remained in the reduced form in the presence of four selected ball-milled MMNs (**Figure 21B**), indicating no electron transfer occurred. In the presence of $(FeCr)(FeCuMn)_2O_4$ and $(CuMg)(FeMnCr)_2O_4$, the oxidized form of cytochrome C was detected (**Figure 21C**), indicating that these materials likely act as an electron mediator between TMB and H_2O_2, a mechanism which has also been reported in other studies.[51,56] For example, Warkhade et al. postulated that the large potential band gap between TMB (1.12 V) and H_2O_2 (1.566 V) makes it difficult for electrons to be transferred directly between the two molecules. They observed that the reduction potential of $CoSe_2$ nanoflakes (1.2 V) was in between that of TMB and H_2O_2, thus facilitating electron transfer and TMB oxidation.[51] A similar observation was found in Ce-doped $ZnCo_2O_4$ and $MoSe_2$ nanoparticles, whereby the enhanced peroxidase-like activity was attributed to a co-contribution of superoxide radicals and electron transfer.[164,283]

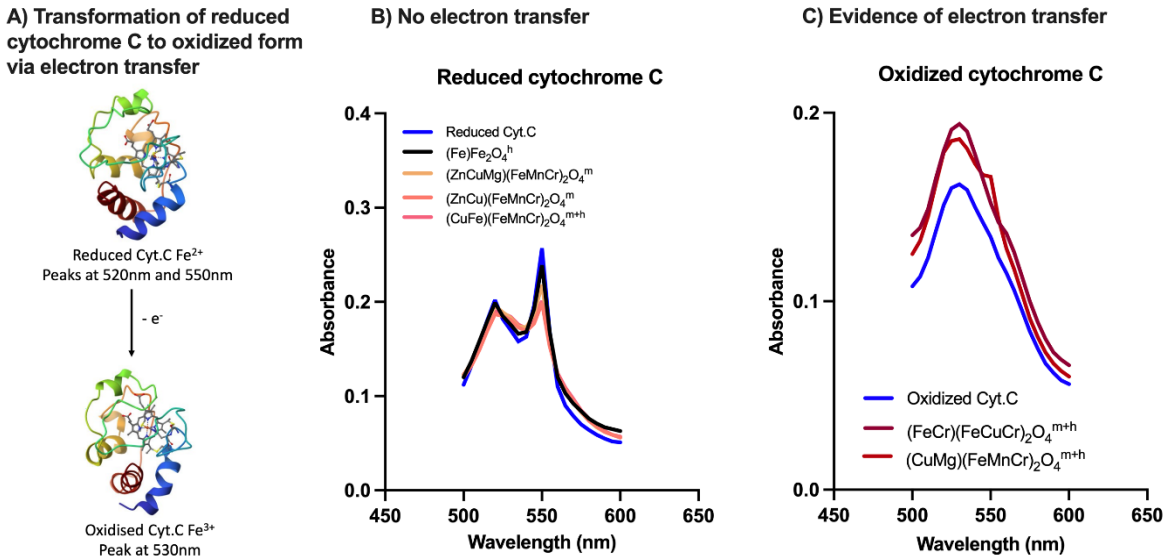

***Figure 21**. (A) Illustration of the transformation from reduced cytochrome C to oxidized cytochrome C via electron donation. (B) Absorbance spectra of reduced cytochrome C alone (blue line) and in the presence of ball-milled materials which do not exhibit electron transfer (others). (C) Absorbance spectra of oxidized cytochrome C alone (blue line) and in the presence of two materials exhibiting electron transfer properties (others).*

3.7 Effect of surface modification on POD-like activity and ex vivo bioassay feasibility assessment

The previous section confirmed the POD-like activity of high entropy-inspired MMNs. To evaluate the feasibility of these materials as an alternative to horseradish peroxidase for ex vivo biomedical applications, five selected ball-milled MMNs were conjugated with rabbit immunoglobin G (IgG) via conventional carbodiimide coupling method (**Figure 7**), then the activity of IgG conjugates were determined (**Figure 22**A). The surface of MMNs was covered by a polymeric surfactant, carboxylated poly(ethylene glycol-co-polystyrene) or PS-PEG-COOH via hydrophobic interactions between the particle surface and the polystyrene component of the surfactant. This attachment hypothetically allowed the terminal carboxyl moieties on the PEG groups to be free for conjugation with IgG. Following addition of the PS-PEG-COOH to the particle dispersion, the carboxyl groups were then activated by EDC/NHS to form a stable ester intermediate which allowed for efficient conjugation with primary amines of IgG molecules. As can be seen, surface modification of MMNs with IgG resulted in variation in catalytic activity, compared to the activity of non-modified materials, however, no distinctive trends were observed (**Figure 22C**).

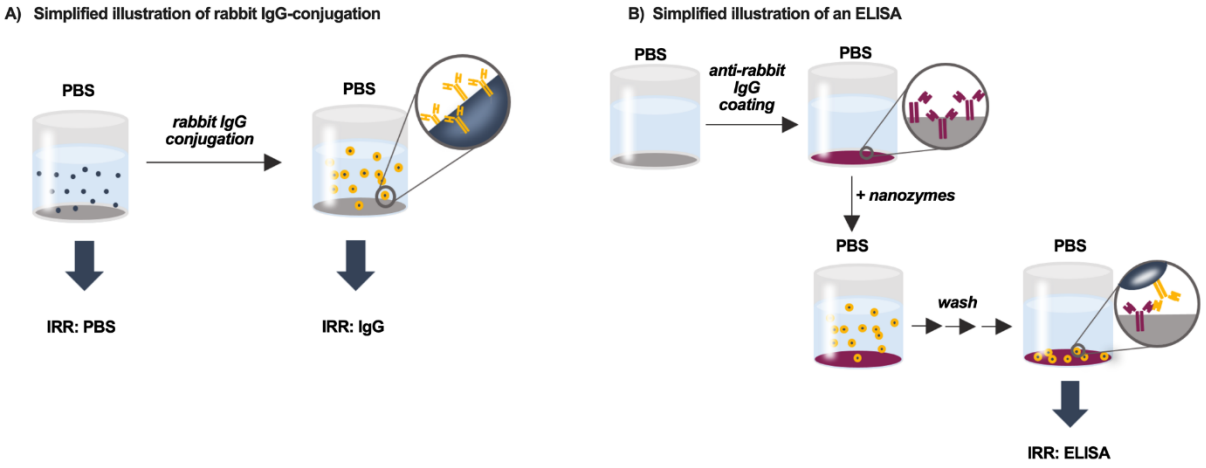

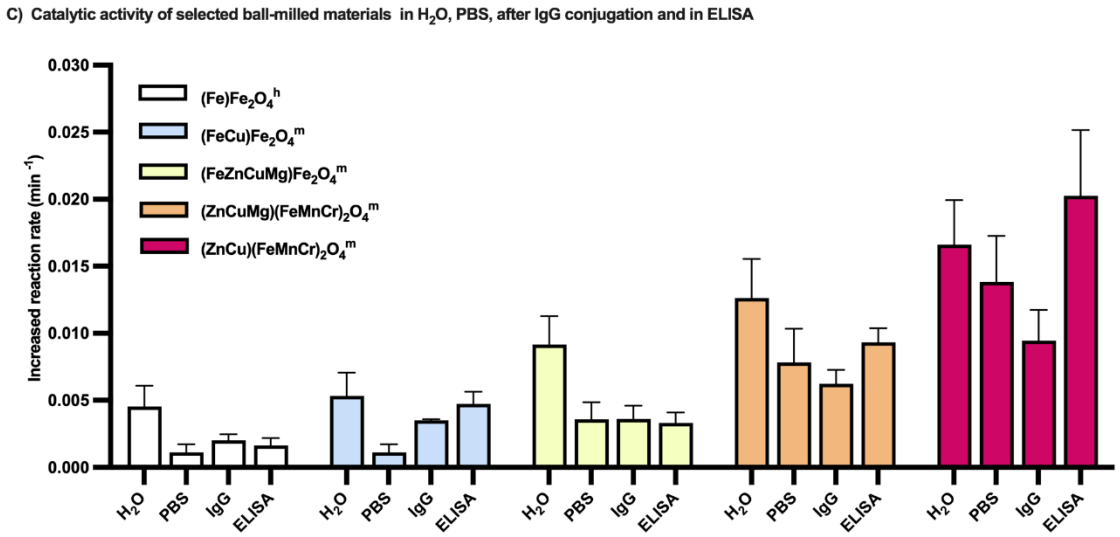

***Figure 22**. Feasibility studies demonstrating MMN performance in an ex vivo ELISA application. Simplified illustration of the IgG conjugation process (A) and ELISA (B). The catalytic activities of five selected ball-milled material in water (n=12), in PBS (n=12), after IgG conjugation (n=4) and in the ELISA (n=3). Results are portrayed as the mean ± standard deviation and all dispersions were prepared from a single ball-milled production batch. Adapted with permission from Phan-Xuan et al.,[267] Copyright (2024) American Chemical Society.*

When employed in a simplified ELISA assay (schematic in **Figure 22B**), the catalytic activity was either similar or higher than that of the dispersed IgG-conjugated materials (**Figure 22C**), indicating 1) that the IgG conjugation to the nanozyme surface was successful, 2) the conjugation process did not negatively impact rabbit IgG binding to its anti-rabbit IgG counterpart and 3) nanozyme activity was preserved in the ELISA.

3.8 Structural-activity relationship of co-precipitated MMNs – a computational approach

3.8.1. Phase property and catalytic activity of co-precipitated MMNs

To gain in-depth understanding the impact of elemental compositions on POD-like activity of MMNs, a larger subset of MMNs was required. Preparation via ball milling is time-consuming, thereby limiting the number of materials produced within a reasonable period. For this reason, different MMN variants were prepared using a co-precipitation approach (>100 samples in one batch). A subset of 70 distinct materials with elemental substitutions in both the AA' and BB'B'' sites was produced via co-precipitation by our collaborators at KIT (Table 10). This material library included three materials with structures corresponding to their ball-milled counterparts. The XRD investigation conducted by collaborators at KIT revealed that the phase property of the co-precipitated subset was more diverse than ball-milled sample set. Indeed, phase separation in some co-precipitated materials showed not only mixtures of magnetite and/or hematite structures but also amorphous and unidentified phases (Appendix, Figure 35).

***Table 10**: Structures of co-precipitated MMNs including their ranking according to catalytic activity. R = Rank order from highest (1) to lowest (70) peroxidase-like activity. Phase properties are also indicated via the superscript: a:amorphous, m:magnetite, m+h:magnetite+hematite. An asterisk indicates materials that were also included in the ball-milled subset. Please note that the composition presented here, as well as the distribution of elements within the A and B sites, is solely based on the amount of precursors employed during the synthesis process. The actual distribution of elements on the A and B sites has not been determined, and as a result, the true chemical formula may deviate. However, it is worth mentioning that the majority of the materials investigated exhibit structures resembling either hematite or magnetite, without the presence of additional phases.*

R	Material	IRR (min^{-1}) mean	SD	R	Material	IRR (min^{-1}) mean	SD
15	$(FeCr)(FeCuCr)_2O_4{}^{a*}$	0.0097	0.0038	41	$(FeMg)(CrMnZn)_2O_4{}^{m}$	0.0058	0.0022

28	$(ZnCu)(FeMnCr)_2O_4$ m+h*	0.0220	0.0060	69	$(FeMg)(CrMnFe)_2O_4$ m+h	0.0018	0.0009
19	$(CuMg)(FeMnCr)_2O_4$ m*	0.0238	0.0052	16	$(FeMg)(CrMnCu)_2O_4$ m	0.0227	0.0125
29	$(ZnMg)(FeMnCr)_2O_4$ m	0.0083	0.0037	38	$(FeMg)(CrMnMn)_2O_4$ m	0.0065	0.0062
39	$(ZnFe)(FeMnCr)_2O_4$ m	0.0062	0.0018	64	$(FeFe)(CrMnZn)_2O_4$ m+h	0.0023	0.0022
33	$(ZnMn)(FeMnCr)_2O_4$ a	0.0072	0.0020	57	$(FeFe)(CrMnMg)_2O_4$ a	0.0032	0.0018
55	$(MgFe)(FeMnCr)_2O_4$ m	0.0038	0.0012	27	$(FeFe)(CrMnCu)_2O_4$ m+h	0.0110	0.0038
26	$(MgMn)(FeMnCr)_2O_4$ m	0.0150	0.0033	58	$(FeFe)(CrMnMn)_2O_4$ a	0.0031	0.0014
31	$(FeMn)(FeMnCr)_2O_4$ m+h+x	0.0078	0.0019	50	$(FeMn)(CrMnZn)_2O_4$ m	0.0047	0.0022
2	$(CuMn)(FeMnCr)_2O_4$ a	0.0585	0.0093	66	$(FeMn)(CrMnMg)_2O_4$ m	0.0023	0.0025
35	$(CrZn)(FeMnMg)_2O_4$ m	0.0070	0.0022	67	$(FeMn)(CrMnFe)_2O_4$ m+h+x	0.0022	0.0015
53	$(CrZn)(FeMnFe)_2O_4$ m+h	0.0044	0.0021	20	$(FeMn)(CrMnCu)_2O_4$ m	0.0209	0.0099
7	$(CrZn)(FeMnCu)_2O_4$ m+x	0.0400	0.0172	47	$(MnZn)(CrFeMg)_2O_4$ m+x	0.0051	0.0014
34	$(CrZn)(FeMnMn)_2O_4$ m	0.0070	0.0051	51	$(MnZn)(CrFeFe)_2O_4$ m+h	0.0046	0.0017
17	$(CrCu)(FeMnZn)_2O_4$ m+x	0.0226	0.0075	4	$(MnZn)(CrFeCu)_2O_4$ m+x	0.0439	0.0063
8	$(CrCu)(FeMnMg)_2O_4$ m	0.0397	0.0104	30	$(MnZn)(CrFeMn)_2O_4$ m	0.0080	0.0035
21	$(CrCu)(FeMnFe)_2O_4$ m+h	0.0201	0.0052	6	$(MnCu)(CrFeZn)_2O_4$ m	0.0403	0.0077
12	$(CrCu)(FeMnMn)_2O_4$ m	0.0264	0.0064	9	$(MnCu)(CrFeMg)_2O_4$ m+h	0.0359	0.0107
44	$(CrMg)(FeMnZn)_2O_4$ m	0.0053	0.0025	14	$(MnCu)(CrFeFe)_2O_4$ m+h	0.0244	0.0046
61	$(CrMg)(FeMnFe)_2O_4$ a	0.0026	0.0013	10	$(MnCu)(CrFeMn)_2O_4$ m	0.0339	0.0053
22	$(CrMg)(FeMnCu)_2O_4$ a	0.0196	0.0036	63	$(MnMg)(CrFeZn)_2O_4$ m	0.0024	0.0013
37	$(CrMg)(FeMnMn)_2O_4$ a	0.0066	0.0028	65	$(MnMg)(CrFeFe)_2O_4$ m+h	0.0023	0.0008
68	$(CrFe)(FeMnZn)_2O_4$ m+h	0.0020	0.0011	25	$(MnMg)(CrFeCu)_2O_4$ m	0.0171	0.0054
59	$(CrFe)(FeMnMg)_2O_4$ m+h	0.0030	0.0019	43	$(MnMg)(CrFeMn)_2O_4$ m+h	0.0055	0.0022
48	$(CrFe)(FeMnCu)_2O_4$ m	0.0051	0.0039	70	$(MnFe)(CrFeZn)_2O_4$ m+h	0.0013	0.0006
52	$(CrFe)(FeMnMn)_2O_4$ m+h+x	0.0045	0.0017	45	$(MnFe)(CrFeMg)_2O_4$ m+h	0.0053	0.0019
56	$(CrMn)(FeMnZn)_2O_4$ m	0.0037	0.0035	24	$(MnFe)(CrFeCu)_2O_4$ m+h	0.0177	0.0047
42	$(CrMn)(FeMnMg)_2O_4$ m+h	0.0056	0.0019	54	$(MnFe)(CrFeMn)_2O_4$ m+h	0.0038	0.0011
60	$(CrMn)(FeMnFe)_2O_4$ m+h	0.0027	0.0012	49	$(MnMn)(CrFeZn)_2O_4$ m	0.0048	0.0024

23	$(CrMn)(FeMnCu)_2O_4$ [m]	0.0179	0.0091	46	$(MnMn)(CrFeMg)_2O_4$ [m]	0.0052	0.0030
32	$(FeZn)(CrMnMg)_2O_4$ [a]	0.0076	0.0035	40	$(MnMn)(CrFeFe)_2O_4$ [m+h]	0.0058	0.0025
62	$(FeZn)(CrMnFe)_2O_4$ [m+h]	0.0025	0.0010	18	$(MnMn)(CrFeCu)_2O_4$ [m]	0.0220	0.0082
5	$(FeZn)(CrMnCu)_2O_4$ [m]	0.0424	0.0050	R = Ranking			
36	$(FeZn)(CrMnMn)_2O_4$ [m]	0.0066	0.0014	[a]amorphous			
13	$(FeCu)(CrMnZn)_2O_4$ [m]	0.0250	0.0064	[m]magnetite			
1	$(FeCu)(CrMnMg)_2O_4$ [a]	0.0632	0.0120	[m+h]magnetite+hematite			
11	$(FeCu)(CrMnFe)_2O_4$ [a]	0.0298	0.0047	[x]unidentified phase			
3	$(FeCu)(CrMnMn)_2O_4$ [m+h]	0.0567	0.0087	*Match with ball-milled materials			

As expected, modification in the MMN composition resulted in different POD-mimicking activity. The IRR values of the top 15 performing materials were plotted demonstrating a broad compositional variety in addition to single and multi-phase properties (***Figure 23A***). By systematically varying the structural composition of the materials, MMNs could be prepared with three-fold higher IRR values compared to the first subset of randomly chosen ball-milled materials (e.g. $(FeCu)(CrMnMg)_2O_4$). This observation provides compelling evidence that the large chemical space offered by MMNs can enable a further optimization of nanozyme activity.

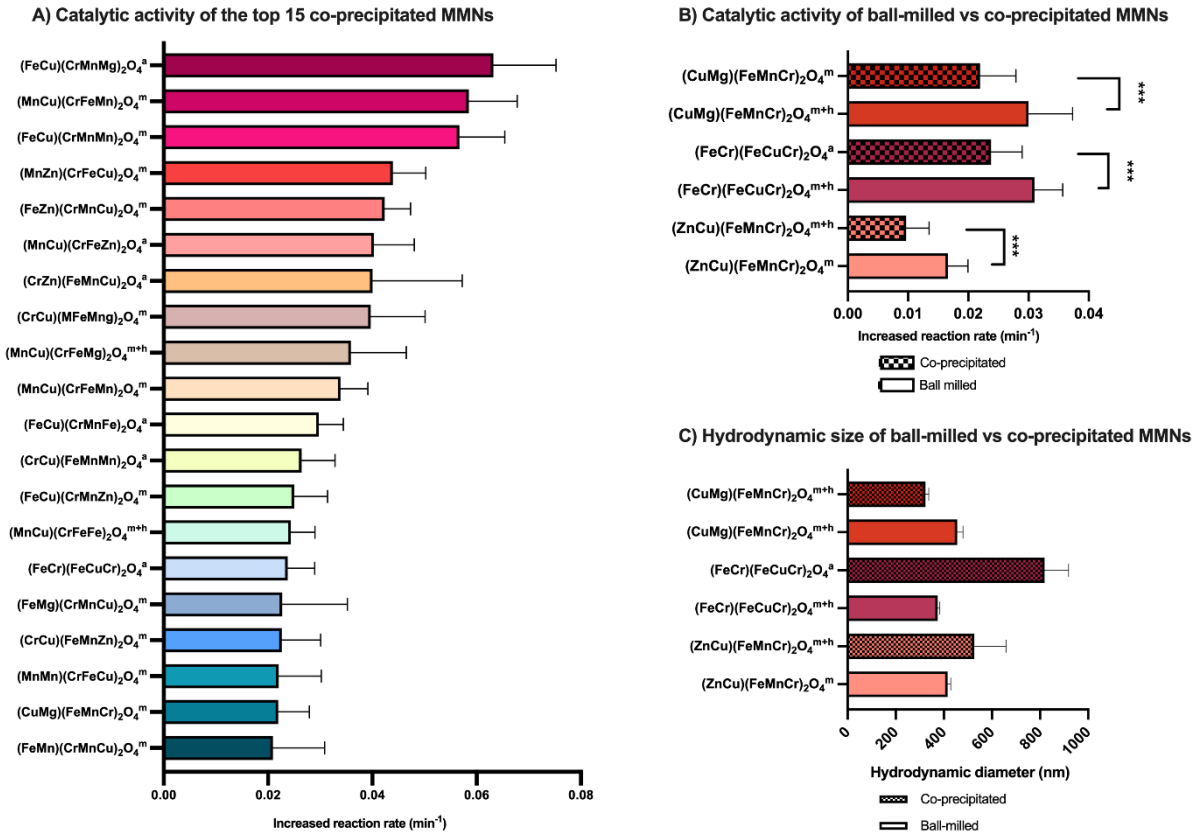

***Figure 23**. Peroxidase-like catalytic activity of co-precipitated MMNs. (A) IRR values of the 15 top performing materials from the co-precipitated MMN subset, in order of decreasing catalytic activity from top to bottom. (B) Comparison of the IRR values of three materials prepared both by ball milling and co-precipitation). Values represent the mean ± standard deviation from n = 12 replicates. Dispersions were prepared from a single nanozyme production batch. ns= non-significant; ***p< 0.001. (C) Comparison of hydrodynamic diameter of ball-milled materials and their co-precipitated counterparts, values represent the mean ± standard deviation from n = 3 replicates. Adapted with permission from Phan-Xuan et al.,[267] Copyright (2024) American Chemical Society.*

Since the method of production may influence the catalytic performance of MMNs, three materials were prepared by ball-milling and co-precipitation for comparison. It was interesting that samples obtained by ball-milling displayed a higher catalytic activity by 10-40%, compared to their co-precipitation counterparts (**Figure 23B**). Assessment of the hydrodynamic diameters using DLS was performed to ascertain whether significant differences in size and therefore surface area might explain this difference. While the mean hydrodynamic diameters of the dispersed materials in water differed between ball-milled and co-precipitated materials, no discernible trends were observed (**Figure 23C**). It is likely that the preparation technique itself makes a difference in terms of reactivity, although the reasons for this remain speculative at this point. Co-precipitation allows the particles to form during a wet chemistry approach and undergo a subsequent thermal annealing step to convert the salts into oxides. The particles form slowly and crystal growth occurs at a slower rate compared to the ball-milling process. During the calcination at several hundred degrees Celsius, the particles are given time to restructure, potentially resolving defects and gradually converting into oxides. In contrast, when using ball-milling, materials are synthesized mechanochemically over a very short time scale. It is documented in the literature that particles prepared by ball-milling exhibit high defect densities, lattice distortions, and a broader distribution of particle sizes, including very small broken particles and larger fractions. Therefore, we postulate that differences resulting from the distinct synthesis methods will strongly impact the catalytic properties. Particularly, defect density (which significantly influences material properties) and surface structure are key factors that could make a difference and will be studied in more detail.

3.8.2. Computational structure-activity relationship of co-precipitated MMNs

With the subset of co-precipitated materials, 41 samples exhibited either a single-phase magnetite structure or were amorphous. The remaining materials exhibited a mixed phase structure, which could have resulted in a mixture of metal oxides with unknown composition, rather than single phase high entropy materials. Therefore, only the 41 single-phase materials were used for computational structure-activity relationships. The computational models were developed by Steffen Hirte from the University of Vienna using the catalytic activity data generated in this work. The following paragraphs summarize the results of the structure-activity study, whereby a full description can be found in

Phan-Xuan et al.[267] Discussions between myself, representing the experimental researcher's point-of-view, and the computational analysis team, helped to inform the approach described in this section.

In total, 492 IRR measurements (41 single phase samples with n=12 replicates of IRR measurements) and different types of features including molar concentration of each element, oxidation state, coordination number, interaction term and partial inverse spinel (PIS) indicator were used for analysis. The model performance (i.e. best fit to the experimental data) then was evaluated using the widely applicable information criterion (WAIC)[284], where a less negative WAIC value indicates a better performance (**Appendix, Table 12**). Consequently, 16 out of 48 GLMs with varying degrees of information granularity were assessed. For easier visualisation, **Figure 24A** shows the dWAIC values of each scheme, which are obtained by results subtracting an individual WAIC value from the least negative WAIC value of the group (scheme #16). A low dWAIC value, therefore, also represents a better model performance. Schemes ranged from simple (using only molar concentration, scheme #1) to complex (including oxidation state, coordination state, binary interactions and PIS indicator). Please refer to the **Appendix, Figure 36** for a detailed illustration and explanation of the model schemes.

Key insights revealed that including the coordination state was crucial for improving model performance (all eight top performing schemes include the coordination state; #9-16). The best-performing models (#15-16) also incorporated interaction terms and oxidation state with the top models differing only by the inclusion of PIS indicator.

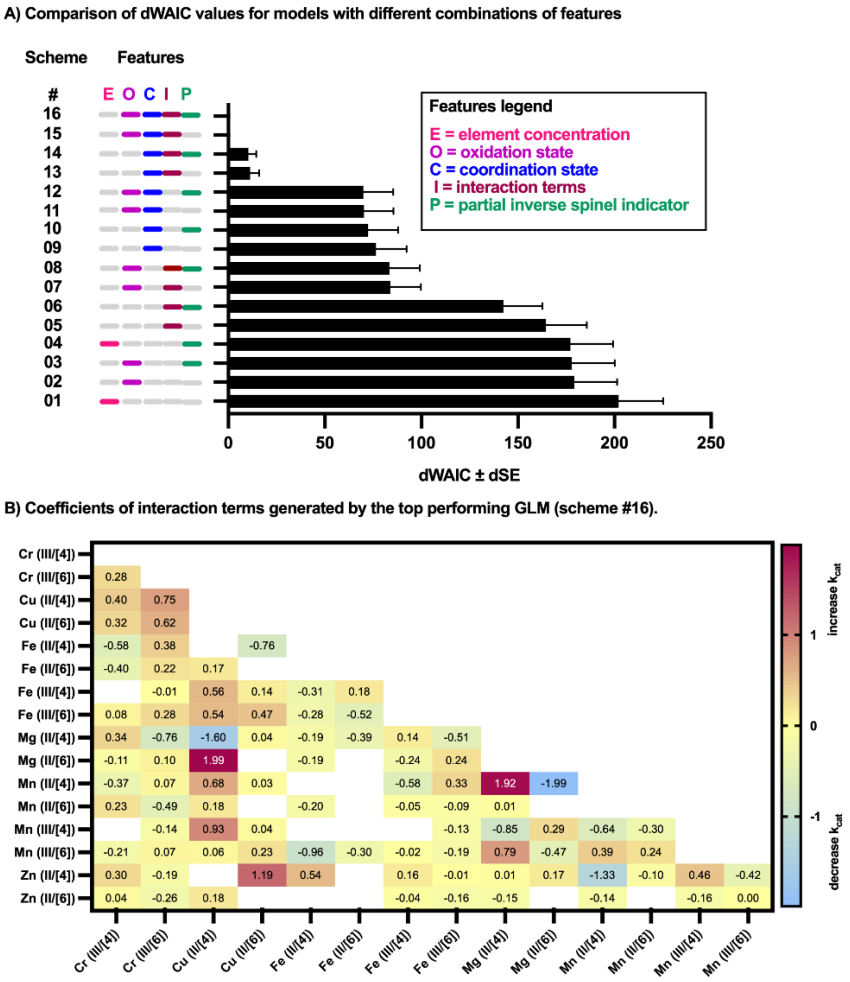

***Figure 24**. Structure-activity analysis of co-precipitated, single-phase MMNs. (A) Comparison of the dWAIC (± difference in standard error; dSE) values of 16 model schemes with differing information granularity. The colored dashes show the features included in each respective scheme. Lower dWAIC values indicate better model performance. (B) Coefficients of interaction terms calculated by scheme #16. Positive values (red boxes) indicate elemental combinations leading to increased k_{cat} values (synergistic interactions), while negative values (blue boxes) indicate interactions which decrease k_{cat} (antagonistic interactions). Blank white fields represent interactions that were not present in the subset of 41 materials used to train the models. Adapted with permission from Phan-Xuan et al.,[267] Copyright (2024) American Chemical Society.*

To design new MMN structures with enhanced catalytic activity, it is valuable to know which combination of elements increase k_{cat}. The heatmap in **Figure 24B** depicts the interaction term coefficients calculated using the top performing model (#16) and indicates which binary combinations increase or decrease k_{cat}. It is important to note that single elemental combinations are not representative of the overall catalytic activity, since each material contains ten interaction pairs. To this end, a mean interaction effect (MIntE) value was calculated for each material (example in **Figure 25A**) and plotted against its corresponding IRR or k_{cat} value (**Figure 25B**). Both Pearson correlation (IRR: r=0.8799; k_{cat}: r=0.9000) and coefficient of determination (IRR: R^2=0.7743; k_{cat}: R^2=0.8100) values indicate that the MIntE is a useful indicator of catalytic activity. As expected from the model, the correlation between MIntE and k_{cat} is slightly better due to the correction for molar concentration of

each element incorporated into the k_{cat} term. Importantly, it has been effectively demonstrated that GLMs can provide insight into the complex structure-activity relationship of MMNs. Furthermore, this complexity can also be elegantly summarized within a single parameter, the MIntE value, which can be employed in future work to design new MMNs with higher performance.

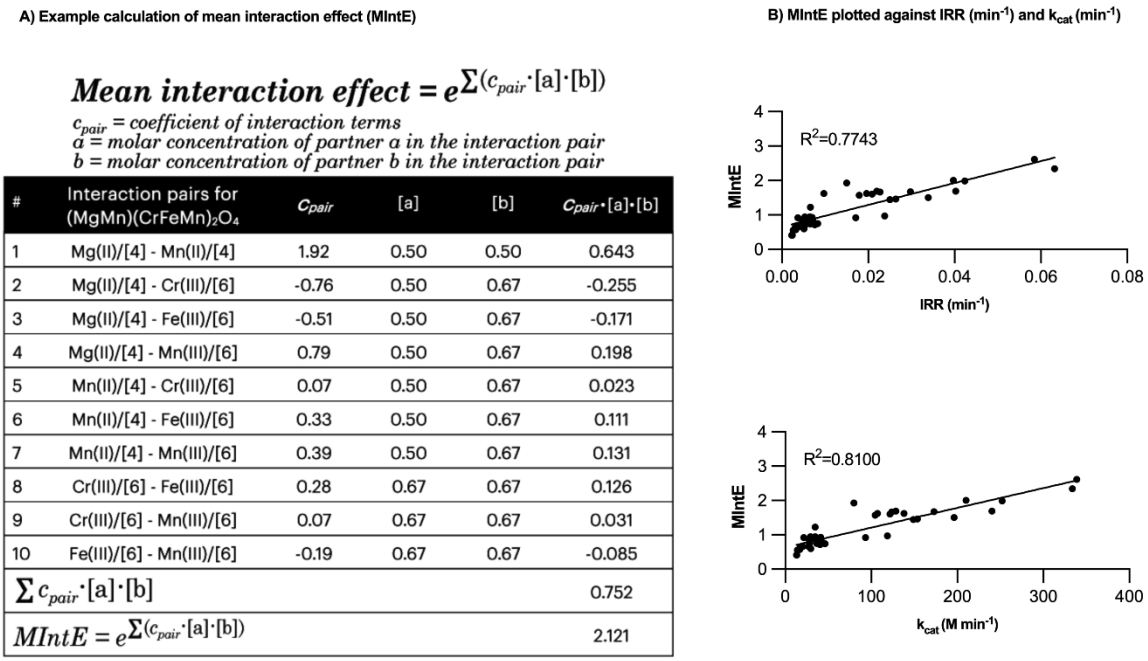

#	Interaction pairs for $(MgMn)(CrFeMn)_2O_4$	c_{pair}	[a]	[b]	c_{pair}·[a]·[b]
1	Mg(II)/[4] - Mn(II)/[4]	1.92	0.50	0.50	0.643
2	Mg(II)/[4] - Cr(III)/[6]	-0.76	0.50	0.67	-0.255
3	Mg(II)/[4] - Fe(III)/[6]	-0.51	0.50	0.67	-0.171
4	Mg(II)/[4] - Mn(III)/[6]	0.79	0.50	0.67	0.198
5	Mn(II)/[4] - Cr(III)/[6]	0.07	0.50	0.67	0.023
6	Mn(II)/[4] - Fe(III)/[6]	0.33	0.50	0.67	0.111
7	Mn(II)/[4] - Mn(III)/[6]	0.39	0.50	0.67	0.131
8	Cr(III)/[6] - Fe(III)/[6]	0.28	0.67	0.67	0.126
9	Cr(III)/[6] - Mn(III)/[6]	0.07	0.67	0.67	0.031
10	Fe(III)/[6] - Mn(III)/[6]	-0.19	0.67	0.67	-0.085
$\sum c_{pair}\cdot[a]\cdot[b]$					0.752
$MIntE = e^{\sum(c_{pair}\cdot[a]\cdot[b])}$					2.121

***Figure 25**. (A) Equation for calculation of the mean interaction effect (MintE) value (C_{pair} = coefficient of the interaction term for a pair of ions taken from the heatmap in C) and example calculation for the material $(MgMn)(CrFeMn)_2O_4$. (B) Correlation plots of MIntE vs IRR (min^{-1}) and MintE vs k_{cat} ($M\ min^{-1}$) for the 41 single phase materials. Adapted with permission from Phan-Xuan et al.,[267] Copyright (2024) American Chemical Society.*

3.9 Investigation of peroxidase-like activity of MMNs with different substrate systems

In the study of Gao et al, magnetite Fe_3O_4 NPs showed peroxidase-like activity toward typical substrates such as TMB, DAB and o-phenylenediamine (ODP). However, the study focused on determining steady-state kinetics of Fe_3O_4 NPs using TMB substrate. It is also of interest to evaluate peroxidase behavior towards different substrates to fully confirm the peroxidase-like property of nanozymes and evaluate the suitabilty of each substrate for further applications, such as for color developing agents in ELISA or lateral flow immuno assay. [568]

This section will describe the peroxidase-mimicking activity of MMNs with other two peroxidase substrate namely DAB and indamine. Due to the limited amount of materials, assays with DAB were carried out with both ball-milled and co-precipitated samples while only ball-milled materials were tested with indamine.

3.9.1. Peroxidase assay of MMNs with DAB substrate

Using DAB as a substrate, **Figure 26** revealed that different MMNs behaved differently in term of peroxidase-mimicking property. Similar to the TMB results, modifications in both AA' and BB'B" offered a higher catalytic performance, except for $(FeCr)(FeZnCr)_2O_4$ which showed very low reactivity, indicating that certain element compositions may be beneficial to the peroxidase-like activity of MMNs. In addition, copper-containing materials again displayed a better catalytic activity than materials without copper. It can also be seen that ball-milled MMNs generally presented a higher reactivity with TMB than DAB substrate. This difference might be attributed to their different oxidation pathways. DAB oxidized via an n-electron irreversible oxidation pathway while TMB oxidation reaction occurs through a reversible 2-electron mechanism.[285]

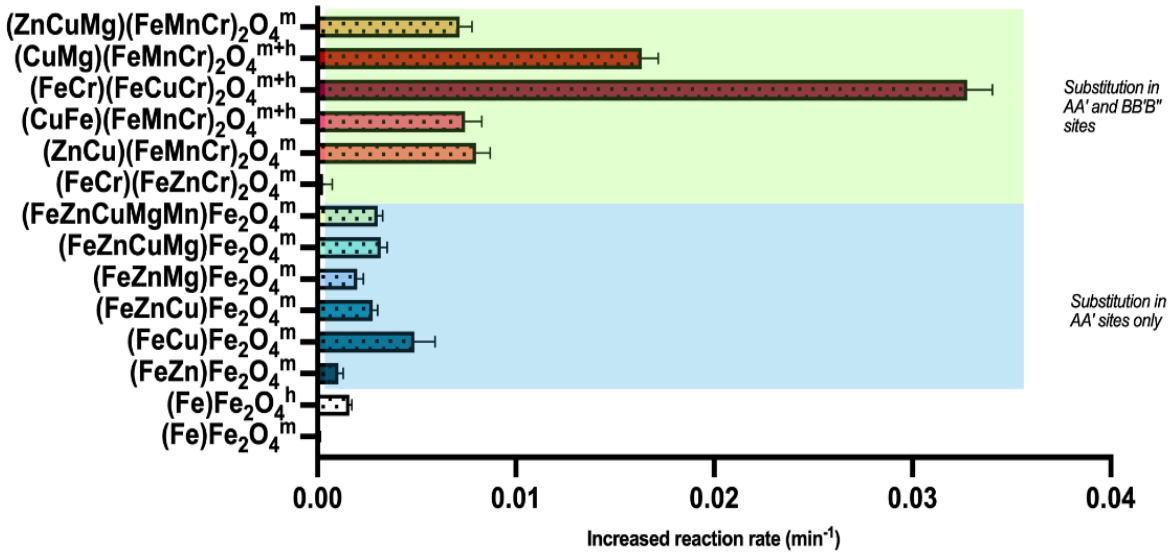

***Figure 26**. IRR (min^{-1}) of non-processed $(Fe)Fe_2O_4$ and ball-milled nanozymes dispersed in water with DAB substrate. Values represent the mean ± standard deviation from n = 12 replicates. All dispersions were prepared from a single production batch. Superscripts: ^{m}magnetite, ^{h}hematite, $^{m+h}$magnetite+hematite.*

The peroxidase assay with DAB was further investigated on a larger material library prepared by co-precipitation. Interestingly, most co-precipitated samples possessed a relatively low catalytic activity (**Table 11**). The highest reactivity was observed in $(CuMn)(CrFeMn)_2O_4$, which was three times lower than the top performer in ball-milled data set, indicating the impact of production method on the catalytic activity of MMNs.

***Table 11**. Mean IRR values ± standard deviation (n=12) of co-precipitated MMNs with DAB substrate*

Material	IRR (min^{-1}) mean	SD	Material	IRR (min^{-1}) mean	SD
$(FeCr)(FeCuCr)_2O_4{}^{a}$*	0.0009	0.0003	$(FeMg)(CrMnZn)_2O_4{}^{m}$	0.0025	0.0023
$(ZnCu)(FeMnCr)_2O_4{}^{m+h}$*	0.0006	0.0003	$(FeMg)(CrMnFe)_2O_4{}^{m+h}$	0.0007	0.0001
$(CuMg)(FeMnCr)_2O_4{}^{m}$*	0.0018	0.0005	$(FeMg)(CrMnCu)_2O_4{}^{m}$	0.0013	0.0007
$(ZnMg)(FeMnCr)_2O_4{}^{m}$	0.0052	0.0004	$(FeMg)(CrMnMn)_2O_4{}^{m}$	0.0026	0.0010
$(ZnFe)(FeMnCr)_2O_4{}^{m}$	0.0024	0.0006	$(FeFe)(CrMnZn)_2O_4{}^{m+h}$	0.0003	0.0002
$(ZnMn)(FeMnCr)_2O_4{}^{a}$	0.0037	0.0004	$(FeFe)(CrMnMg)_2O_4{}^{a}$	0.0015	0.0003
$(MgFe)(FeMnCr)_2O_4{}^{m}$	0.0015	0.0004	$(FeFe)(CrMnCu)_2O_4{}^{m+h}$	0.0009	0.0002
$(MgMn)(FeMnCr)_2O_4{}^{m}$	0.0083	0.003	$(FeFe)(CrMnMn)_2O_4{}^{a}$	0.0042	0.0073
$(FeMn)(FeMnCr)_2O_4{}^{m+h+x}$	0.0038	0.0004	$(FeMn)(CrMnZn)_2O_4{}^{m}$	0.0011	0.0002
$(CuMn)(FeMnCr)_2O_4{}^{a}$	0.0101	0.0006	$(FeMn)(CrMnMg)_2O_4{}^{m}$	0.0028	0.0003
$(CrZn)(FeMnMg)_2O_4{}^{m}$	0.0024	0.0004	$(FeMn)(CrMnFe)_2O_4{}^{m+h+x}$	0.0013	0.0020
$(CrZn)(FeMnFe)_2O_4{}^{m+h}$	0.0044	0.0003	$(FeMn)(CrMnCu)_2O_4{}^{m}$	0.0010	0.0002
$(CrZn)(FeMnCu)_2O_4{}^{m+x}$	0.0044	0.0004	$(MnZn)(CrFeMg)_2O_4{}^{m+x}$	0.0038	0.0006
$(CrZn)(FeMnMn)_2O_4{}^{m}$	0.0026	0.0005	$(MnZn)(CrFeFe)_2O_4{}^{m+h}$	0.0028	0.0004
$(CrCu)(FeMnZn)_2O_4{}^{m+x}$	0.0026	0.007	$(MnZn)(CrFeCu)_2O_4{}^{m+x}$	0.0053	0.0020
$(CrCu)(FeMnMg)_2O_4{}^{m}$	0.0069	0.0004	$(MnZn)(CrFeMn)_2O_4{}^{m}$	0.0039	0.0004
$(CrCu)(FeMnFe)_2O_4{}^{m+h}$	0.0023	0.0007	$(MnCu)(CrFeZn)_2O_4{}^{m}$	0.0061	0.0004
$(CrCu)(FeMnMn)_2O_4{}^{m}$	0.0035	0.0035	$(MnCu)(CrFeMg)_2O_4{}^{m+h}$	0.0069	0.0004
$(CrMg)(FeMnZn)_2O_4{}^{m}$	0.0012	0.0002	$(MnCu)(CrFeFe)_2O_4{}^{m+h}$	0.0031	0.0004
$(CrMg)(FeMnFe)_2O_4{}^{a}$	0.0009	0.0003	$(MnCu)(CrFeMn)_2O_4{}^{m}$	0.0064	0.0017
$(CrMg)(FeMnCu)_2O_4{}^{a}$	0.0018	0.0004	$(MnMg)(CrFeZn)_2O_4{}^{m}$	0.0007	0.0003
$(CrMg)(FeMnMn)_2O_4{}^{a}$	0.0032	0.0010	$(MnMg)(CrFeFe)_2O_4{}^{m+h}$	0.0009	0.0004
$(CrFe)(FeMnZn)_2O_4{}^{m+h}$	0.0006	0.0004	$(MnMg)(CrFeCu)_2O_4{}^{m}$	0.0012	0.0004
$(CrFe)(FeMnMg)_2O_4{}^{m+h}$	0.0013	0.0002	$(MnMg)(CrFeMn)_2O_4{}^{m+h}$	0.0060	0.0033

$(CrFe)(FeMnCu)_2O_4$ [m]	0.0004	0.0005	$(MnFe)(CrFeZn)_2O_4$ [m+h]	0.0007	0.0001
$(CrFe)(FeMnMn)_2O_4$ [m+h+x]	0.0031	0.0037	$(MnFe)(CrFeMg)_2O_4$ [m+h]	0.0009	0.0004
$(CrMn)(FeMnZn)_2O_4$ [m]	0.0011	0.0008	$(MnFe)(CrFeCu)_2O_4$ [m+h]	0.0017	0.0002
$(CrMn)(FeMnMg)_2O_4$ [m+h]	0.0041	0.001	$(MnFe)(CrFeMn)_2O_4$ [m+h]	0.0027	0.0037
$(CrMn)(FeMnFe)_2O_4$ [m+h]	0.0056	0.012	$(MnMn)(CrFeZn)_2O_4$ [m]	0.0009	0.0004
$(CrMn)(FeMnCu)_2O_4$ [m]	0.0022	0.0046	$(MnMn)(CrFeMg)_2O_4$ [m]	0.0021	0.0004
$(FeZn)(CrMnMg)_2O_4$ [a]	0.0049	0.0047	$(MnMn)(CrFeFe)_2O_4$ [m+h]	0.0015	0.0007
$(FeZn)(CrMnFe)_2O_4$ [m+h]	0.0019	0.0002	$(MnMn)(CrFeCu)_2O_4$ [m]	0.0013	0.0004
$(FeZn)(CrMnCu)_2O_4$ [m]	0.0040	0.0004			
$(FeZn)(CrMnMn)_2O_4$ [m]	0.0052	0.0003			
$(FeCu)(CrMnZn)_2O_4$ [m]	0.0026	0.0002			
$(FeCu)(CrMnMg)_2O_4$ [a]	0.0088	0.0005			
$(FeCu)(CrMnFe)_2O_4$ [a]	0.0043	0.0003			
$(FeCu)(CrMnMn)_2O_4$ [m+h]	0.0083	0.0008			

3.9.2 Peroxidase assay of MMNs with indamine as a substrate

The peroxidase-like activityof MMNs was also evaluated with indamine as a substrate. As can be seen in **Figure 27**, the reactivity of ball-milled MMNs with indamine was significantly higher, compared to that with TMB (**Figure 13C**). For example, oxidation of indamine showed a 4-fold higher IRR than TMB oxidation with the same material $(FeCr)(FeCuCr)_2O_4$. Again, materials with elemental substitution in both tetrahedral and octahedral sites displayed a better catalytic activity than the substitution in tetrahedral sites only, confirming this strategy could be a feasible approach to further improve peroxidase-like activity of Fe_3O_4-based MMNs in future studies.

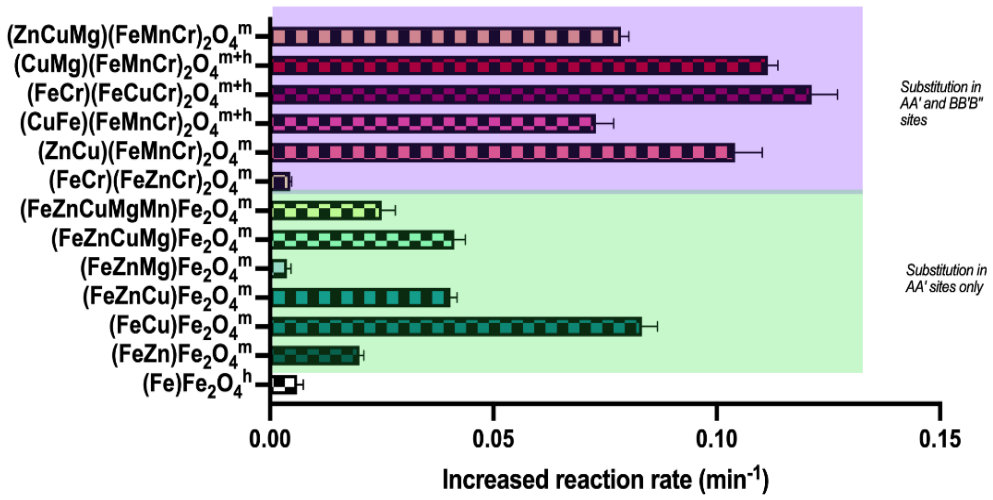

***Figure 27**. IRR (min^{-1}) of ball-milled (Fe)Fe_2O_4 and ball-milled nanozymes dispersed in water with Indamine substrate. Values represent the mean ± standard deviation from n = 4 replicates. All dispersions were prepared from a single production batch. Superscripts: ^{m}magnetite, ^{h}hematite, $^{m+h}$magnetite+hematite.*

3.10 Investigation of catalase-like activity of MMNs

The catalase-like activity of MMNs was investigated using a Europium tetracycline (EuTc)-based fluorescence assay. Basically, EuTc alone is a non-fluorescent complex. The binding of H_2O_2 to the metal center results in a strong fluorescent signal. In the presence of catalase activity-possessing materials, H_2O_2 are decomposed, therefore fluorescent intensity is decreased. As can be seen in **Figure 28**, most of the materials showed moderate catalase-like activity with $(FeCr)(FeCuCr)_2O_4$ achieving the highest catalase performance, which almost doubled that of Fe_3O_4. Unlike peroxidase-like activity, however, the benefit of substitutions in both AA' and BB'B'' was not clear.

The incorporation of multiple metal ions in a crystal structure is also a common strategy to achieve multienzyme-like activity of metal-based nanozymes. For example, several iron oxide-based nanoparticles such as $SnFe_2O_4$, $ZnFe_2O_4$, $MnFe_2O_4$, MFe_2O_4 (M= Ni, Mg, Cu) have been reported with catalase-like activity.[280,286–288] However, these materials are bimetallic platforms. Our study is the first report to reveal the catalase-like activity of Fe_3O_4-based multimetallic nanoparticles with high entropy.

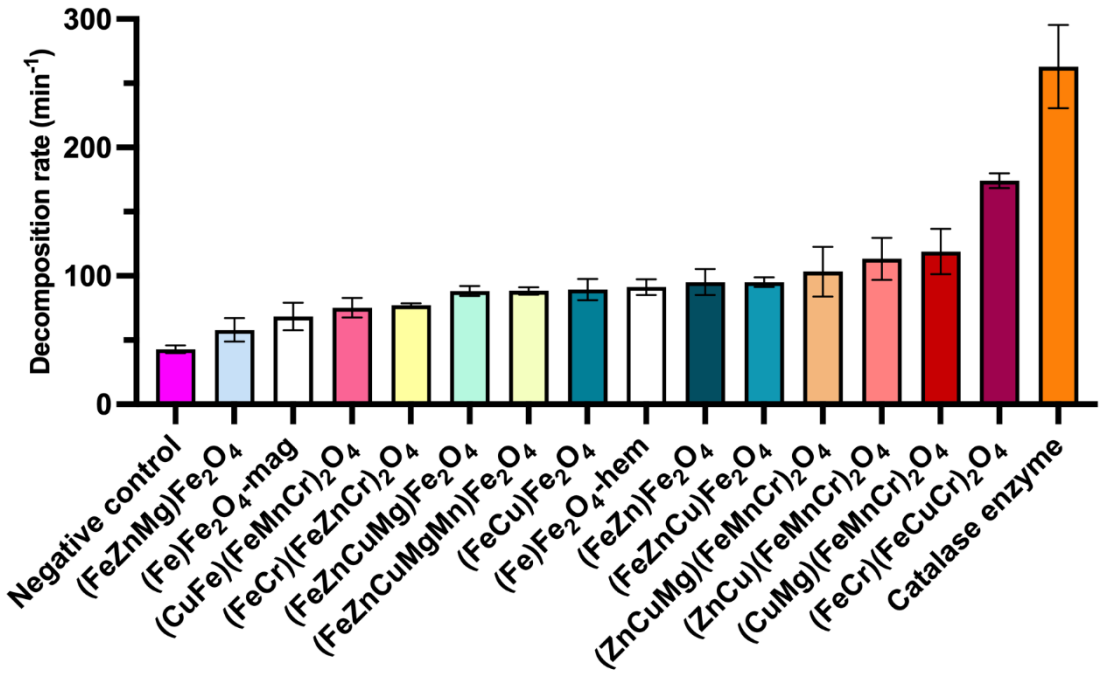

***Figure 28**. Catalase-like activity of ball-milled MMNs . Values represent the mean ± standard deviation from n = 3 replicates.*

The catalase assay was also carried out with co-precipitated MMNs. **Figure 29A** revealed that a majority of co-precipitated MMNs presented negligible activity, below the value of negative control which was reflects the rate of self-decomposition of H_2O_2. Interestingly, some materials even showed an increase in fluorescent intensity, indicating the in-situ generation of H_2O_2. This is possible since superoxide anions $O_2^{\bullet-}$ were generated during peroxidase-like activity of MMNs (section 3.6.2). These anions can be catalysed into H_2O_2 and O_2 in presence of superoxide dismutase – displaying agents. Therefore, the in-situ produced H_2O_2 may react with EuTc, resulting in stronger fluorescence. This observation suggests the superoxide dismutase-like property of MMNs, which will be a topic of interest in future studies.

Similar to peroxidase-like activity, ball-milled materials displayed a higher catalase activity than co-precipated counterparts with the same compositions (**Figure 29B**). This observation again indicates the impact of manufacturing method on the enzyme-like activity of MMNs. Different methods of production may result in nanoparticles with different morphology and surface facets which can affect the reactivity of nanozymes. For example, Fang et al. determined that {100}-facet Pd nanocubes showed a higher oxidase and peroxidase-like activity than {111}-facet Pd nanooctahedrons.[289] A similar observation was also seen when flower-like Mn_3O_4 NPs possessed a superior catalase-like activity than cube, polyhedron and hexagonal plate-shaped Mn_3O_4 NPs due to their higher surface area and larger pore size.[102] The morphology and facet characterisation of MMNs obtained by two production methods will be investigated in detail in future studies.

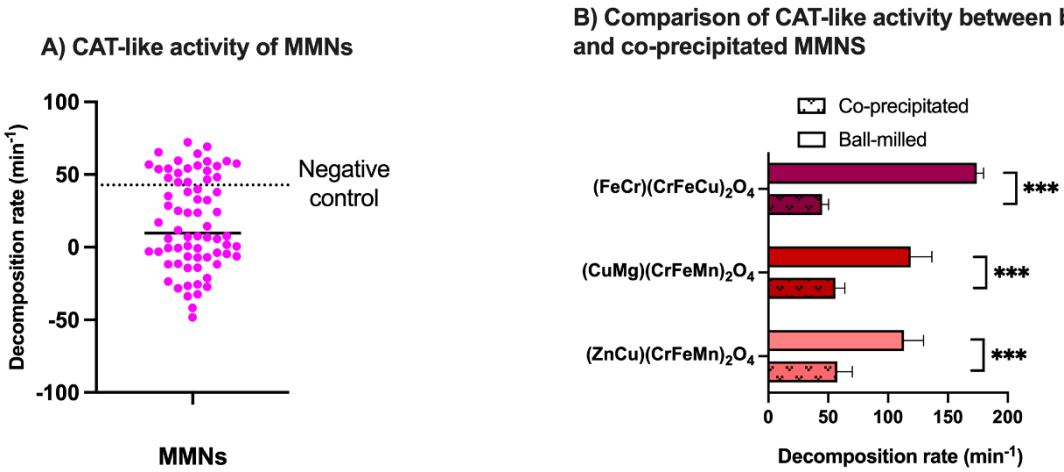

Figure 29. *A) Catalase-like activity of co-precipitated MMNs and B) Comparison between ball-milled and co-precipiatated MMNs in CAT performance. Values represent the mean ± standard deviation from n = 3 replicates.*

Chapter 4 Perspective and future studies

4.1 Contribution of this study to the current status of MMNs

4.1.1 Insights in structure-activity relationship as instructions for rational design of high entropy MMNs with enhanced peroxidase-like activity

Owing to the large compositional space, MMNs are emerging as an interesting materials within nanozymes research. The co-existence of multiple elements allows the tunability of electronic structures and structural characteristics, offering multiple active sites and exploiting the synergistic effect of elemental interactions, thus, resulting in an enhanced catalytic performance. The current state of MMN research has witnessed the blossoming development of bi-, tri- and tertiary metallic platforms while only a few reports of MMNs consisting of five or more elements have been published. Our study is among these early reports. Of note, our study pointed out that by incorporating multiple metal ions in a lattice structure of Fe_3O_4, the peroxidase-like activity of Fe_3O_4 could be significantly improved. In addition, we provided further supporting evidence that the location of elemental exchange in tetrahedral (A-sites) and octahedral (B-sites) of the magnetite structure, especially in both sites, was more beneficial in term of reactivity.

Through the systematic design of materials and the aid of high throughput manufacturing method, we were able to synthesis produce a large library of MMNs with different compositions, which has not been reported in literature. It should be mentioned that most current studies focus on designing MMNs through "trial-and-error", rather than providing instructive information for the rational design of MMNs. Our study, in contrast, generates meaningful outcomes a combinational of experimental and computational structure-activity analysis. Using generalized linear models, we were able to elucidate not only which binary elemental interactions enhanced or reduced catalytic activity, but also predict how the sum of these interactions in the material as a whole, would correlate with activity. This novel parameter, the MintE value, can be used in future to predict and design MMNs with enhanced catalytic activity.

4.1.2 Dual enzyme-property of high entropy MMNs

Our study is the first to reveal the catalase-like activity of high entropy Fe_3O_4-based MMNs. Incorporation of multiple elements can improve the catalase performance of the reference Fe_3O_4 NPs. The dual enzyme-like activity of ball-milled MMNs was visualized in **Figure 30** in which certain element compositions, e.g $(FeCr)(FeCuCr)_2O_4$ presented a high performance in both peroxidase and catalase-

like activity. This finding suggests the possibility of using these materials in other biomedical applications such as chemodynamic therapy through combined effect of peroxidase and catalase activity.

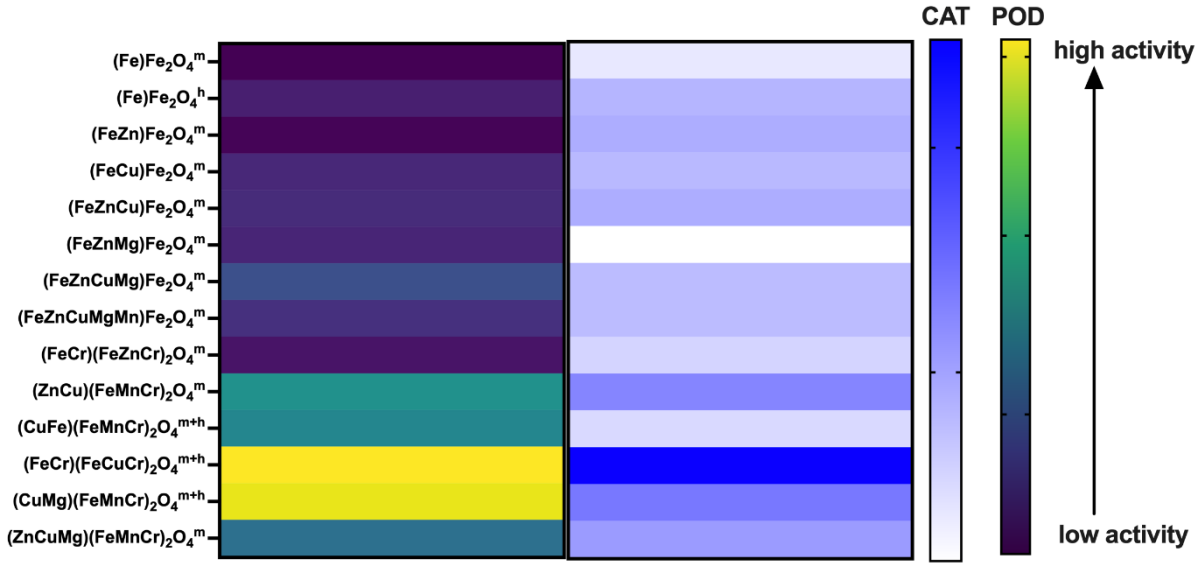

***Figure 30**. Heatmap illustration of dual enzyme-like activity of ball-milled MMNs. Values represent the mean ± standard deviation from n = 12 replicates (POD) and n = 3 replicates (CAT).*

4.2 Limitations

As discussed above, the computational model generated a MintE value as a useful indicator of catalytic activity. However, the coefficients used to calculate the MintE value reported here are only applicable to multi-metallic oxide nanoparticles with similar elemental compositions and spinel structure. For other types of MMNs, e.g. multi-metallic alloys, a new data set and model must be of course generated and validated.

4.3 Future studies

4.3.1 Investigating the structure-activity relationship at the atomic level and the inter-relationship between separate enzyme activities

The GLM in our study has pointed out which elemental combinations are beneficial or detrimental to the peroxidase-like activity of MMNs, when using the elements chosen for this study. However, further work could provide more insight in the relationship between the atomic structure and catalytic activity. Recently, density functional theory (DFT) calculations have been widely utilized to investigate the mechanisms and kinetics for nanozymes. The catalytic activities of nanozymes are the overall consequences of the microscopic reactions occurring at the surfaces of materials. DFT calculations compute the potential energy surfaces along the reaction coordinates for chemical reactions, thus providing in-depth understanding of mechanisms and kinetics at atomistic level for nanozymes.[290] For

example, Shen et al. applied DFT calculations to investigate the POD-mimicking activity of iron oxide nanosurfaces with different chemical compositions, exposed facets and structure effects.[291] The results revealed that the reaction followed a three-step mechanism involving the chemisorption of H_2O_2 on the surface to form two hydroxyl adsorbates and the removal of these hydroxyl groups via two subsequent reduction processes. In addition, the calculated $E_{ads,\ OH}$ value indicated the facet-dependent activity of iron-oxide in which $Fe_3O_4(110)$ facet exhibited POD-activity while $Fe_3O_4(111)_A$ showed no activity. This finding might explain the controversial results reported by Gao[6] and Gumpelmayer et al.[292] about the POD-like activity of iron oxide and maybe the reason for the different activity between ball-milled materials and their co-precipitated counterparts. The DFT calculations were also used in bimetallic Ni-Pt NPs, revealing the importance of surface structure in the high catalytic efficiency.[293] Therefore, applying DFT to discover the structure-activity relationship at atomic level of MMNs would be of interest.

The MMNs were shown to possess peroxidase and catalase-like properties. Multienzyme nanozymes may be advantegous over those with single enzymatic activity due to their synergistic effects and cascade reactions which offer diverse functions in a wide range of applications. Further studies can be done to investigate which elemental compositions might benefit both activities or how to modulate a certain type of activity without interfering with the other.

4.3.2 Combination of single-atom nanozyme and high entropy approach: the next horizon of multi-metallic nanozymes?

Recently, single atom nanozymes (SAzymes) have been the topic of interest due to their unique approach to mimic the highly evolved active centers of natural enzymes. Their atomically dispersed catalytic sites resulted in an optimal atom utilization efficiency, and thus, potentially an enhanced catalytic performance. In addition, the possibility of precise engineering these materials at atomic level can be achieved via modification of the active centers or the interactions between metal centers and supporting ligands.[294] Kim et al. prepared Fe-N_4 single atom nanozymes which mimics the active site of natural peroxidase enzyme. This material exhibited a 5 million times higher activity per iron ion than Fe_3O_4 nanoparticles and an exceptional specificity towards H_2O_2.[295] Moreover, the modification of single-atom iron active center through coordination with phosphorus and nitrogen resulted in FeN_3P SAzymes which outperformed FeN_4 SAzymes and HRP in catalytic efficiency.[296] Another study whereby the higher catalytic activity, compared to FeN_4 SAzymes, was achieved by the substitution of iron with other metals.[297] Furthermore, some natural enzymes such as cytochrome C oxidase, carbon monoxide dehydrogenase and nitrogenase even possess active centers with dual-metal atomic sites.[298–300] This has inspired the discovery of binary SAzymes. For example, dual isolated FeCo-DIA/NC SAzymes were reported with a higher peroxidase-like activity than single atom Fe-

DIA/NC and Co-DIA/NC SAzymes due to the synergistic effect of Fe and Co atoms.[301] Similarly, FeBi-NC SAzymes and Zn/Mo dual SAzymes exhibited enhanced enzyme-like activity, compared to mono-metallic SAzymes.[302,303] As mentioned, high entropy nanomaterials possess unique properties which render them as highly efficient catalysts. Therefore, it will be of great interest to determine whether the combination of these two concepts can lead to new generations of catalysts with superior catalytic efficiency (**Figure 31**). Indeed, only a few of high entropy single-atom catalysts has been reported with impressive catalytic activity due to the abundant active sites and the synergistic effects, demonstrating great potentials for practical energy applications.[304,305] There are plenty of room to investigate high entropy SAzymes in other types of application, particularly in the realm of biomedical sciences.

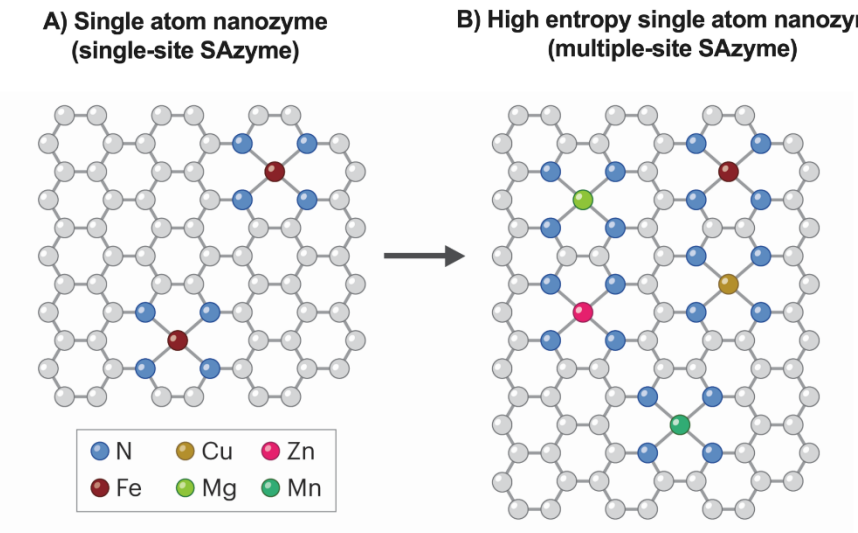

***Figure 31**. Illustration of a SAzyme with single element-active sites (A) and a SAzyme possessing multiple element-active sites with high entropy configuration (B).*

4.3.3 Feasibility study of using MMNs as signal transducers in lateral flow immuno assays (LFIA)

In the last decade, developing diagnostic tools for early detection of diseases has been emerging in the wordwide medical communication. Chapter 1 has provided overview about the potential of MMNs in a wide range of biomedical applications, especially as biosensors in point-of-care (POC) diagnostic test, e.g lateral flow immunoassays (LFIAs). Compared to traditional molecular detection techniques such as ELISA or polymerase chain reaction (PCR), the LFIAs test offers a more rapid detection with cost effectiveness, simplicity with less requirement of human and facility resources. A clear example about the benefit of POC test is the commercial SARS CoV-2 rapid test which helped to rapidly detect infected individuals at a large population scale, therefore controlling the transmission of the disease efffectively. However, one of the main hurdles of LFAs tests is their poor sensitivity which hampers their widespread use in the clinic.[306] To address this shortcoming, various efforts has

been invested, especially the extensive research in nanozymes as biosensors for LFIAs. For example, Wang et al. developed LFIA test based on CdSe@ZnS-COOH nanozymes which detected SARS-CoV-2 with a lower detection limit (12.5 fold) compared to an ELISA kit.[307] Therefore, it would be interesting to investigate the potential of high entropy MMNs with enhanced peroxidase-like activity as signal transducer for LFIA tests. Figure 32outlines a development route for the fabrication of an LFIA strip, starting from nanozyme discovery to evaluation of their performance in a full-component LFIA format with real clinical samples.

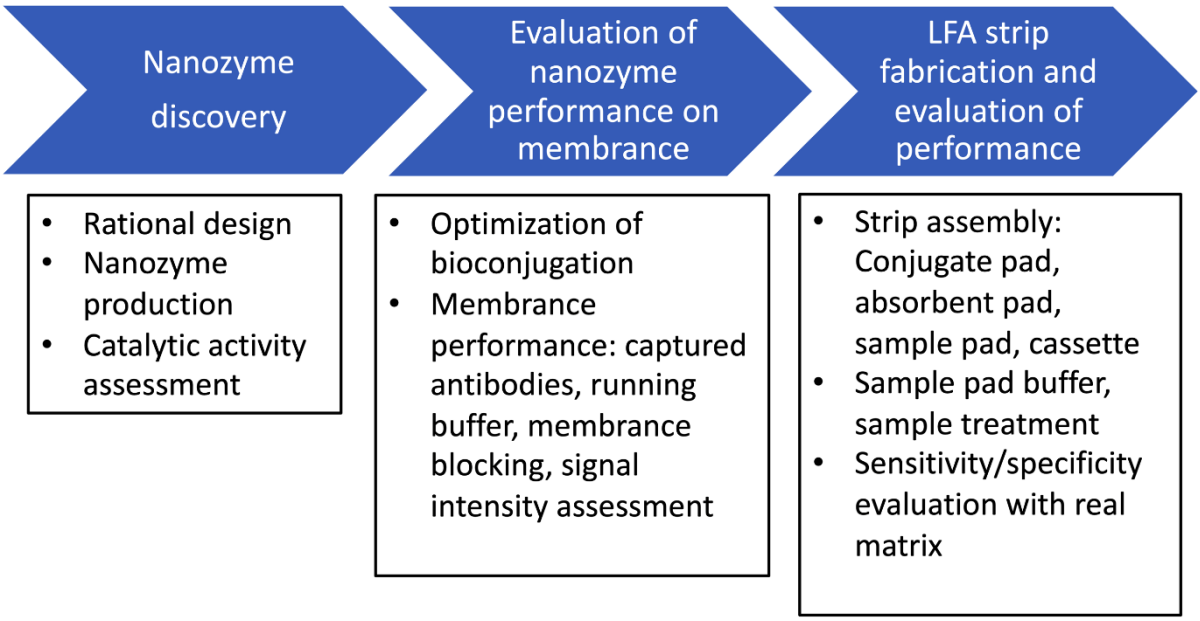

***Figure 32**. Illustration of step-by-step feasibility study of MMNs for lateral flow immunoassay*

In conclusion, our study highlights a promising strategy for enhancing the enzyme-like activity of multimetallic nanozymes through a high-entropy approach. The allocation of multiple metal ions in both the tetrahedral (A sites) and octahedral (B sites) positions within the magnetite structure significantly improved catalytic activity. By employing generalized linear models, we successfully elucidated the structure-activity relationship, which we quantified as the MintE value—a useful metric for the rational design of MMNs with enhanced catalytic properties. Additionally, our MMNs exhibited dual enzyme-like activity. Future research will focus on investigating the structure-activity relationship at the atomic level using DFT, developing and evaluating new nanozymes such as multi-site SAzymes, and assessing the potential of these materials in biomedical applications, such as signal transducers in LFIA.

Appendix

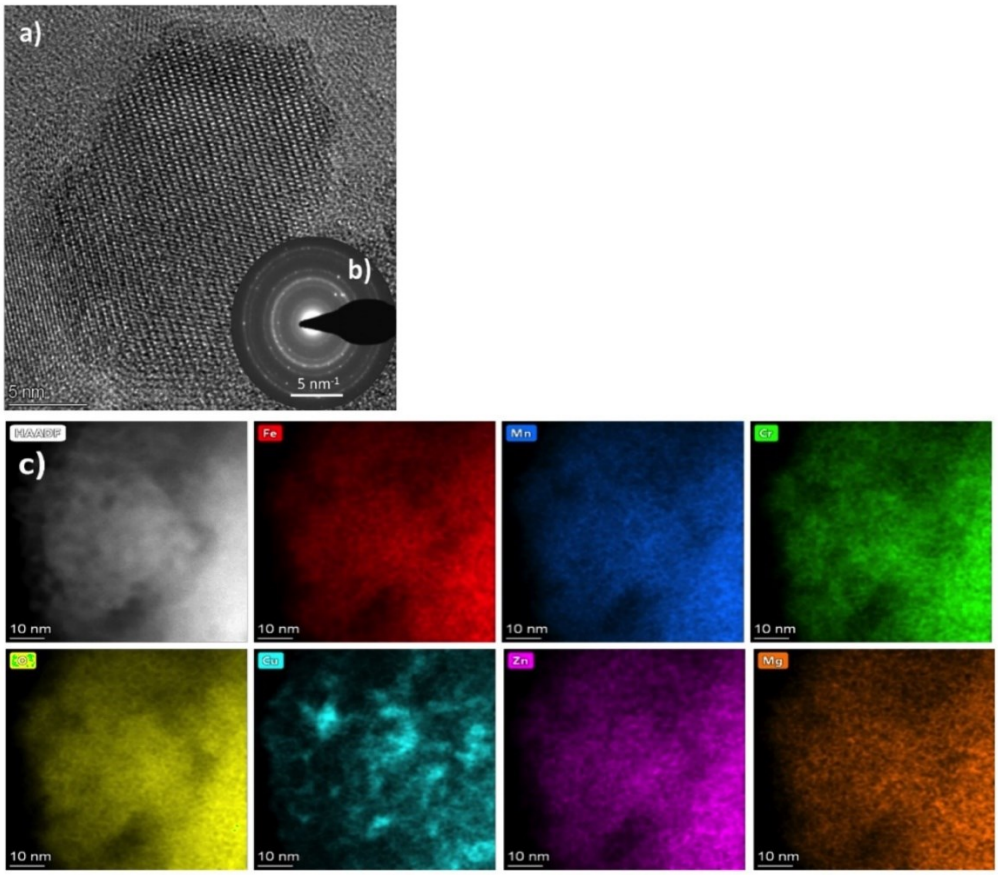

Figure 33. *Characterisation of $(ZnCuMg)(FeMnCr)_2O_4$. a) HR-TEM, b) SAED and c) EDX of $(ZnCuMg)(FeMnCr)_2O_4$*

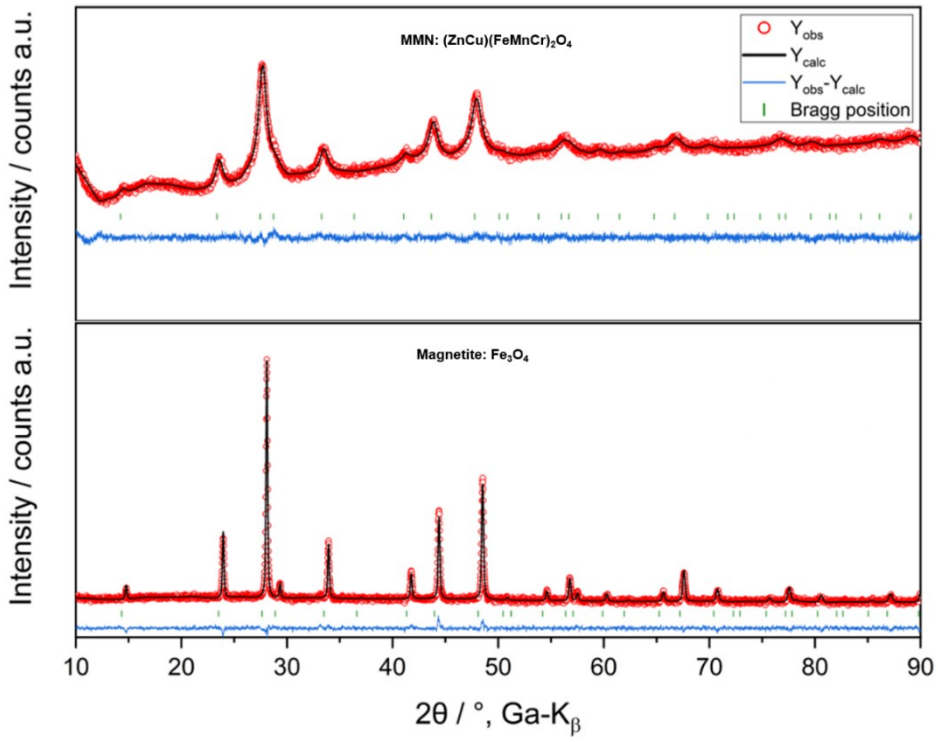

***Figure 34**. Rietveld analysis of XRD spectra is shown for both $(ZnCu)(FeMnCr)_2O_4$ and $(Fe)Fe_2O_4$.*

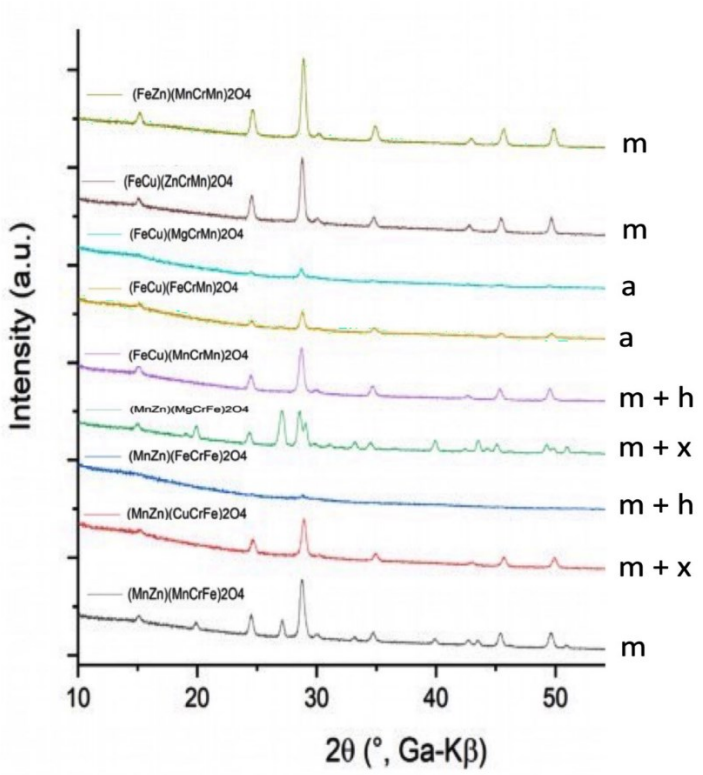
(FeZn)(MnCrMn)2O4
m
(FeCu)(ZnCrMn)2O4
m
(FeCu)(MgCrMn)2O4
a
(FeCu)(FeCrMn)2O4
a
(FeCu)(MnCrMn)2O4
m + h
(MnZn)(MgCrFe)2O4
m + x
(MnZn)(FeCrFe)2O4
m + h
(MnZn)(CuCrFe)2O4
m + x
(MnZn)(MnCrFe)2O4
m
Intensity (a.u.)
10
20
30
40
50
2θ (°, Ga-Kβ)

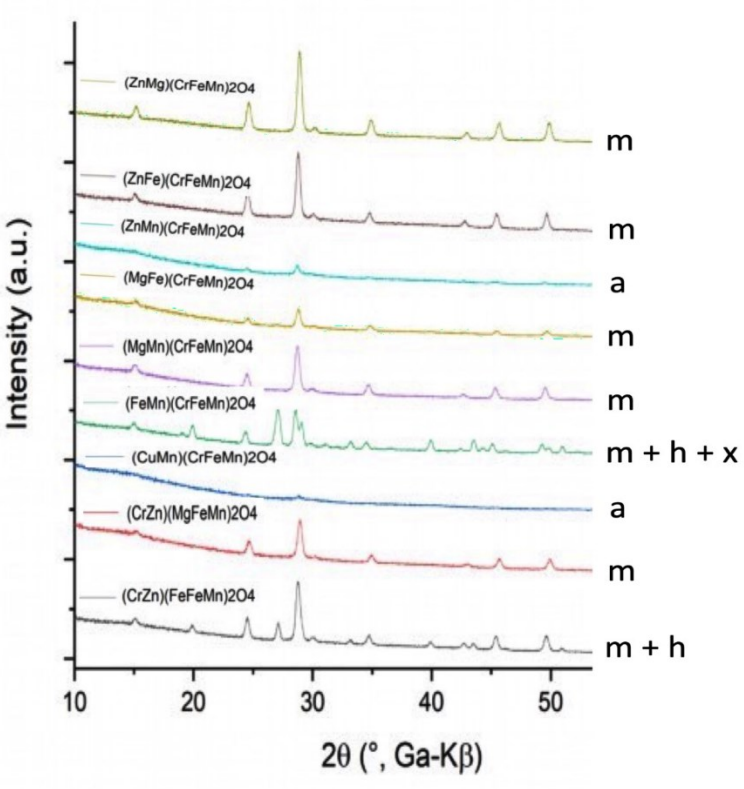
(ZnMg)(CrFeMn)2O4
m
(ZnFe)(CrFeMn)2O4
m
(ZnMn)(CrFeMn)2O4
a
(MgFe)(CrFeMn)2O4
m
(MgMn)(CrFeMn)2O4
m
(FeMn)(CrFeMn)2O4
m + h + x
(CuMn)(CrFeMn)2O4
a
(CrZn)(MgFeMn)2O4
m
(CrZn)(FeFeMn)2O4
m + h
Intensity (a.u.)
10
20
30
40
50
2θ (°, Ga-Kβ)

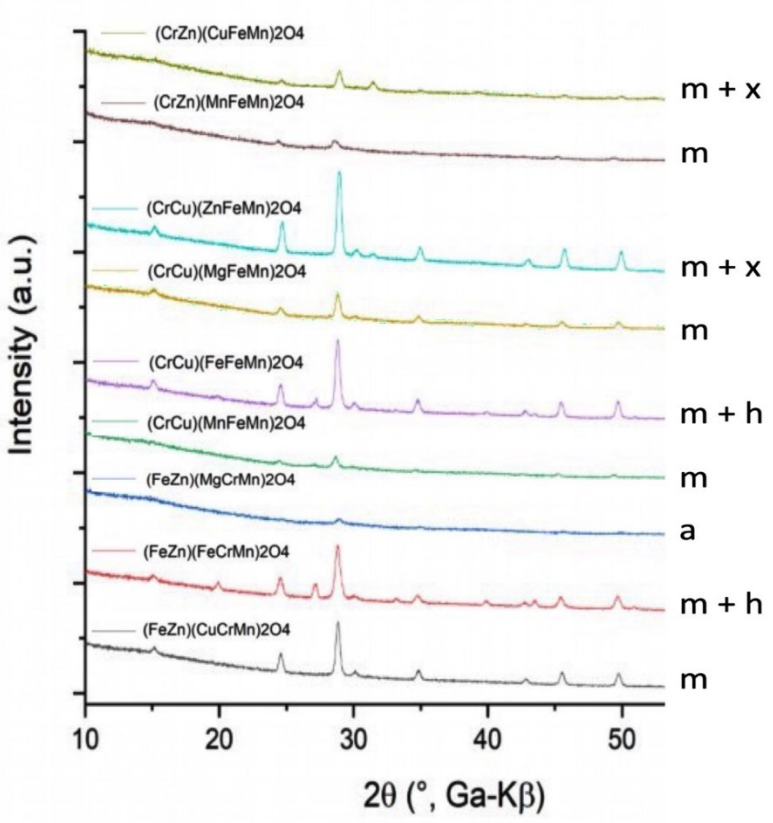
(CrZn)(CuFeMn)2O4
(CrZn)(MnFeMn)2O4
(CrCu)(ZnFeMn)2O4
(CrCu)(MgFeMn)2O4
(CrCu)(FeFeMn)2O4
(CrCu)(MnFeMn)2O4
(FeZn)(MgCrMn)2O4
(FeZn)(FeCrMn)2O4
(FeZn)(CuCrMn)2O4
m + x
m
m + x
m
m + h
m
a
m + h
m
Intensity (a.u.)
10
20
30
40
50
2θ (°, Ga-Kβ)

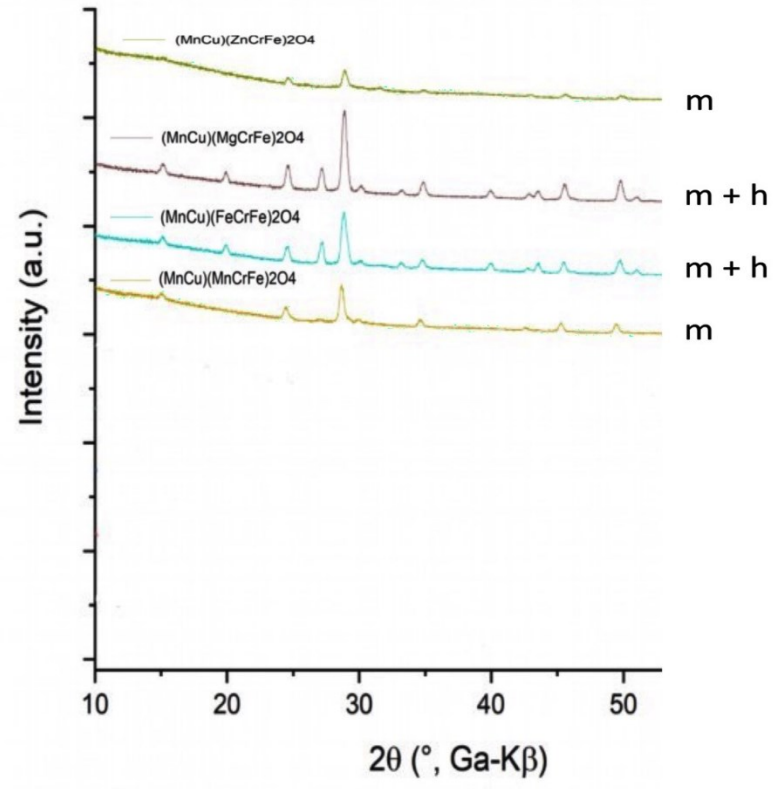
(MnCu)(ZnCrFe)2O4
(MnCu)(MgCrFe)2O4
(MnCu)(FeCrFe)2O4
(MnCu)(MnCrFe)2O4
m
m + h
m + h
m
Intensity (a.u.)
10
20
30
40
50
2θ (°, Ga-Kβ)

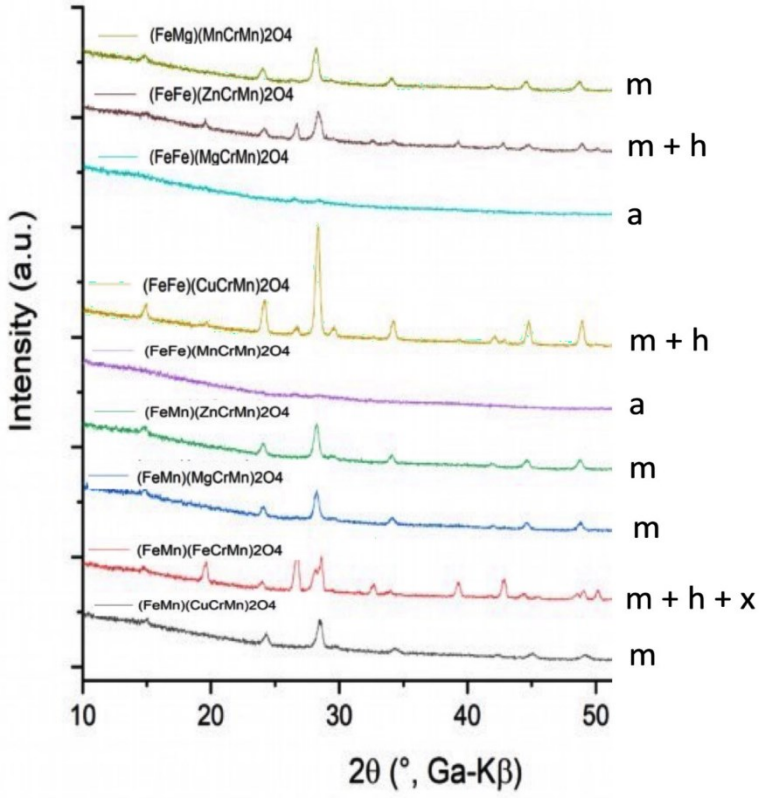
(FeMg)(MnCrMn)2O4
(FeFe)(ZnCrMn)2O4
(FeFe)(MgCrMn)2O4
(FeFe)(CuCrMn)2O4
(FeFe)(MnCrMn)2O4
(FeMn)(ZnCrMn)2O4
(FeMn)(MgCrMn)2O4
(FeMn)(FeCrMn)2O4
(FeMn)(CuCrMn)2O4
m
m + h
a
m + h
a
m
m
m + h + x
m
Intensity (a.u.)
10
20
30
40
50
2θ (°, Ga-Kβ)

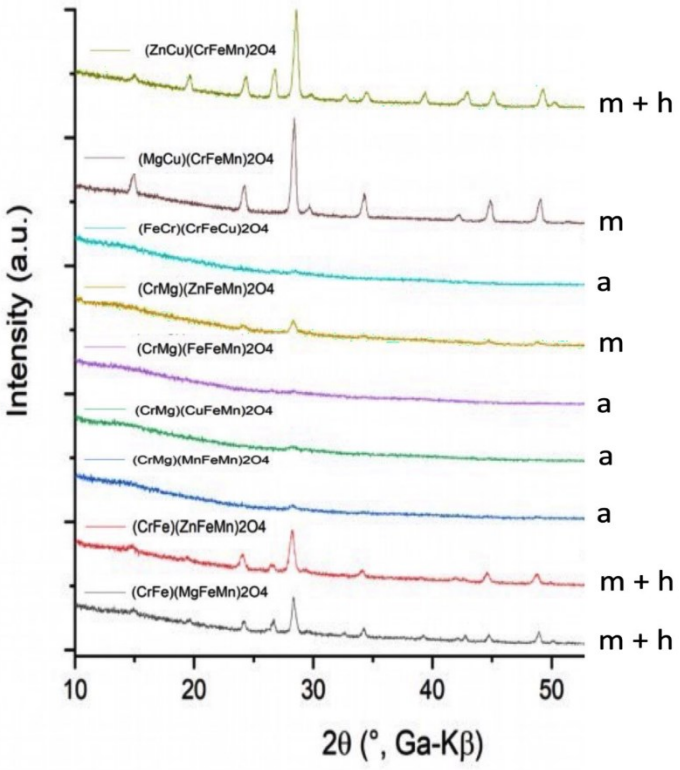
(ZnCu)(CrFeMn)2O4
(MgCu)(CrFeMn)2O4
(FeCr)(CrFeCu)2O4
(CrMg)(ZnFeMn)2O4
(CrMg)(FeFeMn)2O4
(CrMg)(CuFeMn)2O4
(CrMg)(MnFeMn)2O4
(CrFe)(ZnFeMn)2O4
(CrFe)(MgFeMn)2O4
m + h
m
a
m
a
a
a
m + h
m + h
Intensity (a.u.)
10
20
30
40
50
2θ (°, Ga-Kβ)

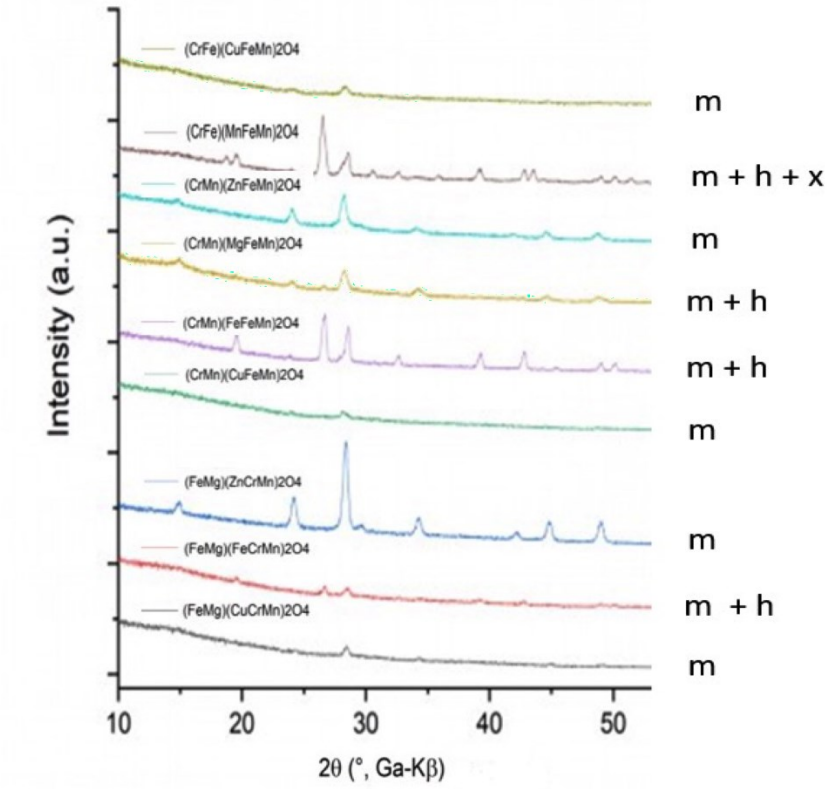
(CrFe)(CuFeMn)2O4
(CrFe)(MnFeMn)2O4
(CrMn)(ZnFeMn)2O4
(CrMn)(MgFeMn)2O4
(CrMn)(FeFeMn)2O4
(CrMn)(CuFeMn)2O4
(FeMg)(ZnCrMn)2O4
(FeMg)(FeCrMn)2O4
(FeMg)(CuCrMn)2O4
m
m + h + x
m
m + h
m + h
m
m
m + h
m
Intensity (a.u.)
10
20
30
40
50
2θ (°, Ga-Kβ)

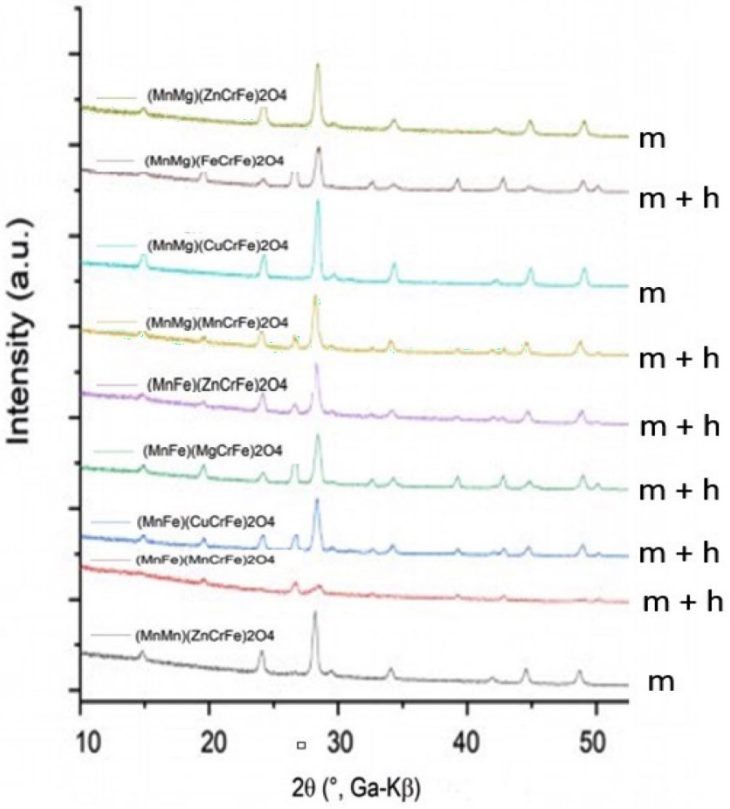
(MnMg)(ZnCrFe)2O4
(MnMg)(FeCrFe)2O4
(MnMg)(CuCrFe)2O4
(MnMg)(MnCrFe)2O4
(MnFe)(ZnCrFe)2O4
(MnFe)(MgCrFe)2O4
(MnFe)(CuCrFe)2O4
(MnFe)(MnCrFe)2O4
(MnMn)(ZnCrFe)2O4
m
m + h
m
m + h
m + h
m + h
m + h
m + h
m
Intensity (a.u.)
10
20
30
40
50
2θ (°, Ga-Kβ)

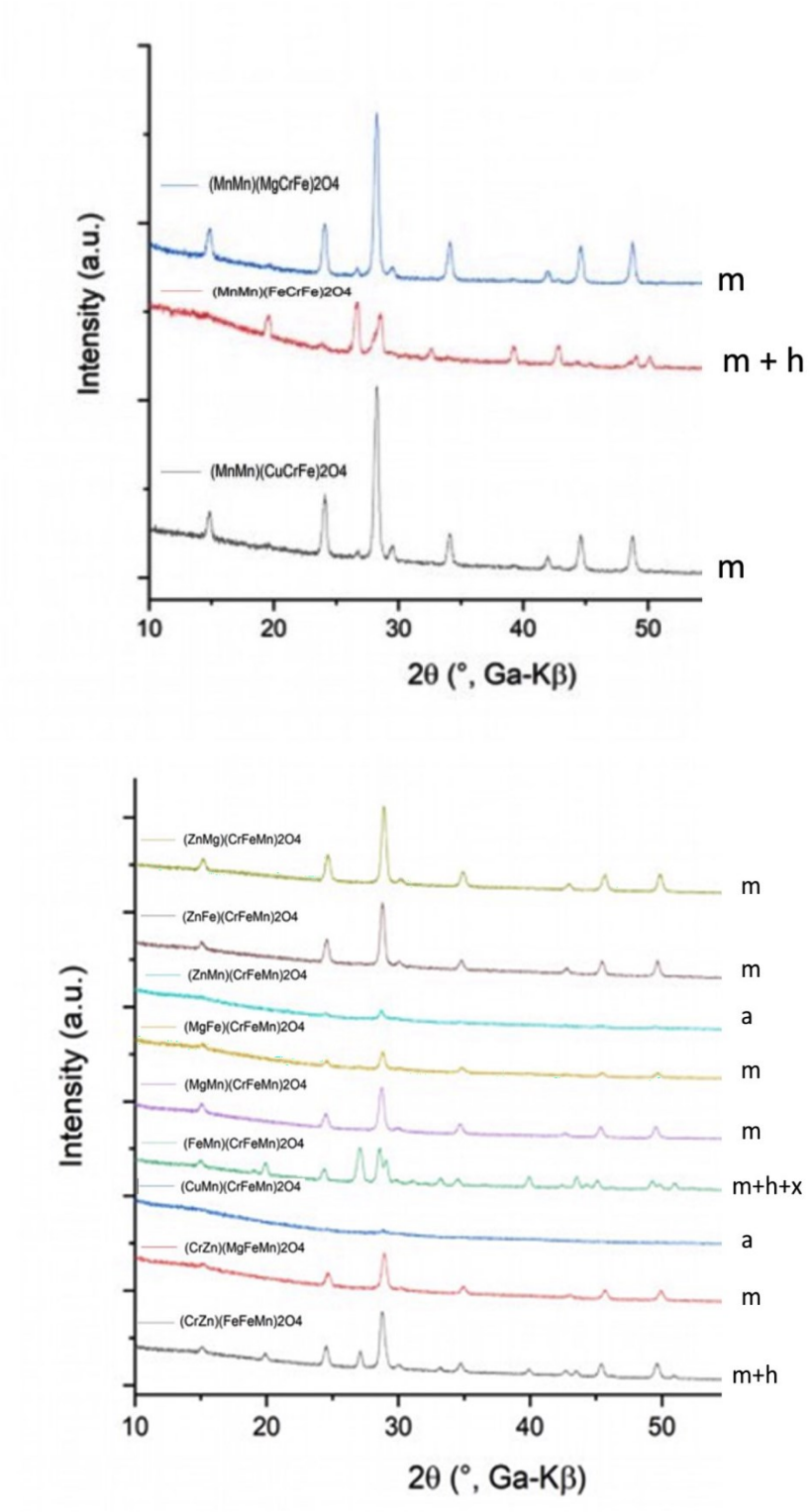

***Figure 35**. XRD spectra of co-precipitated MMNs*

Scheme 1 (E): $\log(\mu_i) = c_0 + (c_{Cu} \cdot [Cu]) + (c_{Fe} \cdot [Fe]) + (c_{Zn} \cdot [Zn]) + (c_{Mn} \cdot [Mn]) + (c_{Mg} \cdot [Mg]) + (c_{Cr} \cdot [Cr])$

Example of factorial matrix with input values (i.e. molar concentrations of elements) for scheme #1

	[Cu]	[Fe]	[Zn]	[Mn]	[Mg]	[Cr]	[Response]
$(FeZn)(FeCrMn)_2O_4$	0	1.17	0.50	0.67	0	0.67	$\log \mu_1$
$(CrZn)(CuFeMn)_2O_4$	0.67	0.67	0.50	0.67	0	0.50	$\log \mu_2$
$(MnZn)(CuCrFe)_2O_4$	0.67	0.67	0.50	0.50	0	0.67	$\log \mu_3$
$(MnMn)(MgCrFe)_2O_4$	0	0.67	0	1.00	0.67	0.67	$\log \mu_4$
$(ZnMg)(MnCrFe)_2O_4$	0	0.67	0.50	0.67	0.50	0.67	$\log \mu_5$
⋮	⋮	⋮	⋮	⋮	⋮	⋮	⋮

Response log (μ_i) = mean of k_{cat} from n=12 replicates of composition i following a Gamma distribution

Scheme 2 (O): $\log(\mu_i) = c_0 + (c_{Cu(II)} \cdot [Cu(II)]) + (c_{Fe(II)} \cdot [Fe(II)]) + (c_{Fe(III)} \cdot [Fe(III)]) + (c_{Mn(III)} \cdot [Mn(III)]) + (c_{Zn(II)} \cdot [Zn(II)])) + (c_{Cr(III)} \cdot [Cr(III)]) \ldots$

Example of factorial matrix with input values (i.e. molar concentrations of elements with different oxidation states) for scheme #2

	[Cu (II)]	[Zn (II)]	[Mg (II)]	[Fe (II)]	[Fe (III)]	[Mn (II)]	[Mn (III)]	[Cr (III)]	[Response]
$(FeZn)(FeCrMn)_2O_4$	0	0.50	0	0.67	0.50	0	0.67	0.67	$\log \mu_1$
$(CrZn)(CuFeMn)_2O_4$	0.67	0.50	0	0	0.67	0	0.67	0.50	$\log \mu_2$
$(MnZn)(CuCrFe)_2O_4$	0.67	0.50	0	0	0.67	0	0.50	0.67	$\log \mu_3$
$(MnMn)(MgCrFe)_2O_4$	0	0	0	0	0.67	0.50	0.50	0.67	$\log \mu_4$
$(ZnMg)(MnCrFe)_2O_4$	0	0.50	0.50	0	0.67	0	0.67	0.67	$\log \mu_5$
⋮	⋮	⋮	⋮	⋮	⋮	⋮	⋮	⋮	⋮

Scheme 3 (O, P): $\log(\mu_i) = c_0 + (c_{Cu(II)} \cdot [Cu(II)]) + (c_{Fe(II)} \cdot [Fe(II)]) + (c_{Fe(III)} \cdot [Fe(III)]) + (c_{Mn(III)} \cdot [Mn(III)]) + (c_{Zn(II)} \cdot [Zn(II)])) + (c_{Cr(III)} \cdot [Cr(III)]) \ldots + (c_{PISi} \cdot PISi)$

Example of factorial matrix with input values (i.e. molar concentrations of elements with different oxidation states + PIS indicator) for scheme #3

	[Cu (II)]	[Zn (II)]	[Mg (II)]	[Fe (II)]	[Fe (III)]	[Mn (II)]	[Mn (III)]	[Cr (III)]	PISi	[Response]
$(FeZn)(FeCrMn)_2O_4$	0	0.50	0	0.67	0.50	0	0.67	0.67	1	$\log \mu_1$
$(CrZn)(CuFeMn)_2O_4$	0.67	0.50	0	0	0.67	0	0.67	0.50	1	$\log \mu_2$
$(MnZn)(CuCrFe)_2O_4$	0.67	0.50	0	0	0.67	0	0.50	0.67	1	$\log \mu_3$
$(MnMn)(MgCrFe)_2O_4$	0	0	0	0	0.67	0.50	0.50	0.67	1	$\log \mu_4$
$(ZnMg)(MnCrFe)_2O_4$	0	0.50	0.50	0	0.67	0	0.67	0.67	0	$\log \mu_5$
⋮	⋮	⋮	⋮	⋮	⋮	⋮	⋮	⋮	⋮	⋮

Scheme 11 (O, C): $\log(\mu_i) = c_0 + (c_{Cu(II)/[4]} \cdot [Cu(II)/[4]]) + (c_{Cu(II)/[6]} \cdot [Cu(II)/[6]]) + (c_{Zn(II)/[4]} \cdot [Zn(II)/[4]]) + (c_{Zn(II)/[6]}) \cdot [Zn(II)/[6]]) \ldots$

Example of factorial matrix with input values (i.e. molar concentrations of elements with different oxidation and coordination states)

	[Cu(II)/[4]]	[Cu(II)/[6]]	[Zn(II)/[4]]	[Zn(II)/[6]]	[Mg(II)/[4]]	[Mg(II)/[6]]	...	[Cr(III)/[4]]	[Cr(III)/[6]]	[Response]
$(FeZn)(FeCrMn)_2O_4$	0	0	0.50	0	0	0	...	0	0.67	$\log \mu_1$
$(CrZn)(CuFeMn)_2O_4$	0	0.67	0.50	0	0	0	...	0.50	0	$\log \mu_2$
$(MnZn)(CuCrFe)_2O_4$	0	0.67	0.50	0	0	0	...	0	0.67	$\log \mu_3$
$(MnMn)(MgCrFe)_2O_4$	0	0	0	0	0	0	...	0	0.67	$\log \mu_4$
$(ZnMg)(MnCrFe)_2O_4$	0	0	0.50	0	0.50	0.50	...	0.50	0.67	$\log \mu_5$
⋮	⋮	⋮	⋮	⋮	⋮	⋮	⋮	⋮	⋮	⋮

Scheme 16 (O, C, I, P): $\log(\mu_i) = c_0 + (c_{Cu(II)/[4]:Zn(II)/[6]} \cdot [Cu(II)/[4]] \cdot [Zn(II)/[6]]) + (c_{Cu(II)/[6]:Zn(II)/[4]} \cdot [Cu(II)/[6]] \cdot [Zn(II)/[4]]) +) \ldots + (c_{PISi} \cdot PISi)$

Example of factorial matrix with input values (i.e. product of molar concentrations of two interacting elements with different oxidation and coordination states)

	[Cu(II)/[4]] · [Zn(II)/[6]]	[Cu(II)/[6]] · [Zn(II)/[4]]	[Zn(II)/[4]] · [Fe(II)/[6]]	[Zn(II)/[4]] · [Fe(III)/[6]]	...	PISi	[Response]
$(FeZn)(FeCrMn)_2O_4$	0 · 0 = 0	0.50 · 0 = 0	0.50 · 0.67 = 0.325	0.50 · 0 = 0	...	1	$\log \mu_1$
$(CrZn)(CuFeMn)_2O_4$	0 · 0 = 0	0.50 · 0 = 0	0.50 · 0 = 0	0.50 · 0.67 = 0.325	...	1	$\log \mu_2$
$(MnZn)(CuCrFe)_2O_4$	0 · 0 = 0	0.50 · 0.67 = 0.325	0.50 · 0 = 0	0.50 · 0.67 = 0.325	...	1	$\log \mu_3$
$(MnMn)(MgCrFe)_2O_4$	0 · 0 = 0	0 · 0 = 0	0 · 0 = 0	0 · 0.67 = 0	...	1	$\log \mu_4$
$(ZnMg)(MnCrFe)_2O_4$	0 · 0 = 0	0.50 · 0 = 0	0.50 · 0 = 0	0.50 · 0.67 = 0.325	...	0	$\log \mu_5$
⋮	⋮	⋮	⋮	⋮	⋮	⋮	⋮

Figure 36. *Model equations for schemes #1, 2, 3, 11 and 16 are listed. Beneath each equation, examples of the factorial matrix of independent variables used in each scheme are depicted. Five materials were selected from the 41 single-phase compositions to illustrate how the molar concentrations of the elements in each material were inputted into the model. Note: As the independent variables increased in information-richness (i.e. including more than one feature; schemes #10 and 16), the number of independent variables increased and could not be listed comprehensively in these examples.*

***Table 12**. Comparison of the performance of model schemes using different types of features (also featured in the main manuscript **Figure 24**). Schemes highlighted in blue (with a gamma distribution) were those chosen for the final analysis in the main study. [1]WAIC values with a lower negativity denote a better fit of the model to the data. SE = standard error; pWAIC = theoretical number of features effective in the model. Features: E= element concentration (molar); O=oxidation state; C= coordination state; I = Interaction terms; P = partially inverse spinel indicator*

Scheme #	Family	Link	E	O	C	I	P	# of features	WAIC +- SE	dWAIC	dSE	pWAIC
NA	gaussian	log	x					8	-2790.4 ± 27.1	512	34.8	10
NA	gaussian	log		x				10	-2769.6 ± 27.1	491.2	34.6	16
NA	gaussian	identity				x		23	-2768.7 ± 26.3	490.2	34.4	8
NA	gaussian	identity						8	-2768.6 ± 26.3	490.1	34.4	8
NA	gaussian	log		x			x	11	-2767.4 ± 27.9	489	35.1	16
NA	gaussian	log					x	9	-2765.8 ± 27.7	487.4	35	14
NA	gaussian	identity		x		x		38	-2756.3 ± 25.7	477.9	34	9
NA	gaussian	identity		x				10	-2756.2 ± 25.8	477.8	34	9
NA	gaussian	identity				x	x	24	-2755.8 ± 25.3	477.3	33.7	9
NA	gaussian	identity					x	9	-2755.4 ± 25.2	477	33.7	9
NA	gaussian	identity		x			x	11	-2754.8 ± 25.2	476.3	33.7	10
NA	gaussian	identity		x		x	x	39	-2754.7 ± 25.2	476.3	33.7	10
NA	gaussian	log				x		23	-2675.7 ± 26.9	397.2	34.5	19
NA	gaussian	log				x	x	24	-2652.2 ± 26.3	373.8	33.7	23
NA	gaussian	identity			x			14	-2632.4 ± 25.8	354	32.3	13
NA	gaussian	identity			x	x		73	-2632.1 ± 25.8	353.7	32.3	13
NA	gaussian	identity			x		x	15	-2630.7 ± 25.5	352.3	32.3	14

NA	gaussian	identity		x	x	x	74	-2630.4 ± 25.5	352	32.3	14
NA	gaussian	identity	x	x		x	19	-2627.9 ± 25.4	349.5	32.1	14
NA	gaussian	identity	x	x			18	-2627.9 ± 25.4	349.5	32.1	14
NA	gaussian	identity	x	x	x	x	111	-2627.5 ± 25.4	349.1	32.1	14
NA	gaussian	identity	x	x	x		110	-2627.5 ± 25.4	349	32.1	14
NA	gaussian	log	x		x		38	-2560.5 ± 28.4	282.1	33.9	27
NA	gaussian	log	x		x	x	39	-2559.4 ± 28.3	281	33.8	28
NA	gaussian	log		x			14	-2526.7 ± 28.7	248.2	32	19
NA	gaussian	log		x		x	15	-2509.1 ± 28.5	230.7	31.8	21
NA	gaussian	log	x	x			18	-2502.7 ± 28.8	224.3	31.8	22
NA	gaussian	log	x	x		x	19	-2502.7 ± 28.8	224.3	31.8	22
1	gamma	log	x				8	-2480.6 ± 25.8	202.1	23.2	7
NA	gaussian	log		x	x		73	-2473.7 ± 32.1	195.3	32.9	35
2	gamma	log	x				10	-2457.6 ± 26.5	179.2	22.2	8
3	gamma	log	x			x	11	-2456.4 ± 26.6	178	22.1	8
4	gamma	log				x	9	-2455.6 ± 26.6	177.2	22.1	8
5	gamma	log			x		23	-2443.0 ± 25.5	164.5	21.2	14
6	gamma	log			x	x	24	-2421.0 ± 26.1	142.6	20.1	16
NA	gaussian	log		x	x	x	74	-2418.8 ± 33.6	140.4	32.9	39
NA	gaussian	log	x	x	x		110	-2415.7 ± 34.2	137.3	33	41
NA	gaussian	log	x	x	x	x	111	-2415.4 ± 34.2	137	33	41
7	gamma	log	x		x		38	-2362.3 ± 27.2	83.9	15.8	20

8	gamma	log	x		x	x	39	-2361.8 ± 27.2	83.4	15.7	20
9	gamma	log		x			14	-2354.9 ± 26.9	76.5	15.9	12
10	gamma	log		x		x	15	-2350.8 ± 27.1	72.4	15.5	13
11	gamma	log	x	x			18	-2348.6 ± 26.9	70.2	15.3	14
12	gamma	log	x	x		x	19	-2348.4 ± 27.0	70	15.3	14
13	gamma	log		x	x		73	-2289.7 ± 30.1	11.3	4.7	39
14	gamma	log		x	x	x	74	-2288.8 ± 30.3	10.4	4.1	40
15	gamma	log	x	x	x		110	-2278.5 ± 31.7	0	0.2	43
16	**gamma**	**log**	**x**	**x**	**x**	**x**	**111**	**-2278.4 ± 31.7**	**0**	**0**	**43**

References

(1) Phan-Xuan, T.; Breitung, B.; Dailey, L. A. Nanozymes for Biomedical Applications: Multi-Metallic Systems May Improve Activity but at the Cost of Higher Toxicity? *Wiley Interdiscip Rev Nanomed Nanobiotechnol* **2024**, *16* (4). https://doi.org/10.1002/wnan.1981.

(2) Khatkhatay, M. I.; Desai, M. A Comparison of Performances of Four Enzymes Used in ELISA with Special Reference to β-Lactamase. *J Immunoassay* **1999**, *20* (3), 151–183. https://doi.org/10.1080/01971529909349349.

(3) Porstmann, B.; Porstmann, T.; Nugel, E.; Evers, U. *Which of the Commonly Used Marker Enzymes Gives the Best Results in Colorimetric and Fluorimetric Enzyme Immunoassays: Horseradish Peroxidase, Alkaline Phosphatase or Fl-Galactosidase?*; 1985; Vol. 79.

(4) Shivakumar, A.; BG, J.; MR, D. Role of Peroxidase in Clinical Assays: A Short Review. *Journal of Clinical Nutrition & Dietetics* **2017**, *03* (02). https://doi.org/10.4172/2472-1921.100048.

(5) Manea, F.; Houillon, F. B.; Pasquato, L.; Scrimin, P. Nanozymes: Gold-Nanoparticle-Based Transphosphorylation Catalysts. *Angewandte Chemie - International Edition* **2004**, *43* (45), 6165–6169. https://doi.org/10.1002/anie.200460649.

(6) Gao; Zhuang, J.; Nie, L.; Zhang, J.; Zhang, Y.; Gu, N.; Wang, T.; Feng, J.; Yang, D.; Perrett, S.; Yan, X. Intrinsic Peroxidase-like Activity of Ferromagnetic Nanoparticles. *Nat Nanotechnol* **2007**, *2* (9), 577–583. https://doi.org/10.1038/nnano.2007.260.

(7) Lou, D.; Tian, Y.; Zhang, Y.; Yin, J.; Yang, T.; He, C.; Ma, M.; Yu, W.; Gu, N. Peroxidase-Like Activity of Gold Nanoparticles and Their Gold Staining Enhanced ELISA Application. *J Nanosci Nanotechnol* **2017**, *18* (2), 951–958. https://doi.org/10.1166/jnn.2018.13977.

(8) Jin, L.; Meng, Z.; Zhang, Y.; Cai, S.; Zhang, Z.; Li, C.; Shang, L.; Shen, Y. Ultrasmall Pt Nanoclusters as Robust Peroxidase Mimics for Colorimetric Detection of Glucose in Human Serum. *ACS Appl Mater Interfaces* **2017**, *9* (11), 10027–10033. https://doi.org/10.1021/acsami.7b01616.

(9) Cao, G. J.; Jiang, X.; Zhang, H.; Croley, T. R.; Yin, J. J. Mimicking Horseradish Peroxidase and Oxidase Using Ruthenium Nanomaterials. *RSC Adv* **2017**, *7* (82), 52210–52217. https://doi.org/10.1039/c7ra10370k.

(10) Chen, W.; Chen, J.; Feng, Y. Bin; Hong, L.; Chen, Q. Y.; Wu, L. F.; Lin, X. H.; Xia, X. H. Peroxidase-like Activity of Water-Soluble Cupric Oxide Nanoparticles and Its Analytical Application for Detection of Hydrogen Peroxide and Glucose. *Analyst* **2012**, *137* (7), 1706–1712. https://doi.org/10.1039/c2an35072f.

(11) Tian, Z.; Li, J.; Zhang, Z.; Gao, W.; Zhou, X.; Qu, Y. Highly Sensitive and Robust Peroxidase-like Activity of Porous Nanorods of Ceria and Their Application for Breast Cancer Detection. *Biomaterials* **2015**, *59*, 116–124. https://doi.org/10.1016/j.biomaterials.2015.04.039.

(12) Dong, J.; Song, L.; Yin, J. J.; He, W.; Wu, Y.; Gu, N.; Zhang, Y. Co3O4 Nanoparticles with Multi-Enzyme Activities and Their Application in Immunohistochemical Assay. *ACS Appl Mater Interfaces* **2014**, *6* (3), 1959–1970. https://doi.org/10.1021/am405009f.

(13) Song, Y.; Wang, X.; Zhao, C.; Qu, K.; Ren, J.; Qu, X. Label-Free Colorimetric Detection of Single Nucleotide Polymorphism by Using Single-Walled Carbon Nanotube Intrinsic Peroxidase-like Activity. *Chemistry - A European Journal* **2010**, *16* (12), 3617–3621. https://doi.org/10.1002/chem.200902643.

(14) Song, Y.; Qu, K.; Zhao, C.; Ren, J.; Qu, X. Graphene Oxide: Intrinsic Peroxidase Catalytic Activity and Its Application to Glucose Detection. *Advanced Materials* **2010**, *22* (19), 2206–2210. https://doi.org/10.1002/adma.200903783.

(15) Garg, B.; Bisht, T. Carbon Nanodots as Peroxidase Nanozymes for Biosensing. *Molecules*. MDPI AG December 1, 2016. https://doi.org/10.3390/molecules21121653.

(16) Bagheri, N.; Dastborhan, M.; Khataee, A.; Hassanzadeh, J.; Kobya, M. Synthesis of G-C 3 N 4 @CuMOFs Nanocomposite with Superior Peroxidase Mimetic Activity for the Fluorometric Measurement of Glucose. *Spectrochim Acta A Mol Biomol Spectrosc* **2019**, *213*, 28–36. https://doi.org/10.1016/j.saa.2019.01.025.

(17) Ruan, X.; Liu, D.; Niu, X.; Wang, Y.; Simpson, C. D.; Cheng, N.; Du, D.; Lin, Y. 2D Graphene Oxide/Fe-MOF Nanozyme Nest with Superior Peroxidase-Like Activity and Its Application for Detection of Woodsmoke Exposure Biomarker. *Anal Chem* **2019**, *91* (21), 13847–13854. https://doi.org/10.1021/acs.analchem.9b03321.

(18) Liang, M.; Yan, X. Nanozymes: From New Concepts, Mechanisms, and Standards to Applications. *Acc Chem Res* **2019**, *52* (8), 2190–2200. https://doi.org/10.1021/acs.accounts.9b00140.

(19) He, S. Bin; Chen, F. Q.; Xiu, L. F.; Peng, H. P.; Deng, H. H.; Liu, A. L.; Chen, W.; Hong, G. L. Highly Sensitive Colorimetric Sensor for Detection of Iodine Ions Using Carboxylated Chitosan–Coated Palladium Nanozyme. *Anal Bioanal Chem* **2020**, *412* (2), 499–506. https://doi.org/10.1007/s00216-019-02270-7.

(20) Hu, L.; Yuan, Y.; Zhang, L.; Zhao, J.; Majeed, S.; Xu, G. Copper Nanoclusters as Peroxidase Mimetics and Their Applications to H2O2 and Glucose Detection. *Anal Chim Acta* **2013**, *762*, 83–86. https://doi.org/10.1016/j.aca.2012.11.056.

(21) Liu, X.; Yan, L.; Ren, H.; Cai, Y.; Liu, C.; Zeng, L.; Gao, J.; Liu, A. Facile Synthesis of Magnetic Hierarchical Flower-like Co3O4 Spheres: Mechanism, Excellent Tetra-Enzyme Mimics and Their Colorimetric Biosensing Applications. *Biosens Bioelectron* **2020**, *165*. https://doi.org/10.1016/j.bios.2020.112342.

(22) Yang, Z.; Wang, C.; Lu, X. Conducting Polymer-Based Peroxidase Mimics: Synthesis, Synergistic Enhanced Properties and Applications. *Science China Materials*. Science China Press May 1, 2018, pp 653–670. https://doi.org/10.1007/s40843-018-9235-3.

(23) Zheng, H. Q.; Liu, C. Y.; Zeng, X. Y.; Chen, J.; Lü, J.; Lin, R. G.; Cao, R.; Lin, Z. J.; Su, J. W. MOF-808: A Metal-Organic Framework with Intrinsic Peroxidase-Like Catalytic Activity at Neutral PH for Colorimetric Biosensing. *Inorg Chem* **2018**, *57* (15), 9096–9104. https://doi.org/10.1021/acs.inorgchem.8b01097.

(24) Goyal, M. M.; Basak, A. Human Catalase: Looking for Complete Identity. *Protein and Cell*. Higher Education Press 2010, pp 888–897. https://doi.org/10.1007/s13238-010-0113-z.

(25) Munjal, T.; Dutta, S. Biocompatible Nanoreactors of Catalase and Nanozymes for Anticancer Therapeutics. *Nano Select* **2021**, *2* (10), 1849–1873. https://doi.org/10.1002/nano.202100040.

(26) Chen, Z.; Yin, J. J.; Zhou, Y. T.; Zhang, Y.; Song, L.; Song, M.; Hu, S.; Gu, N. Dual Enzyme-like Activities of Iron Oxide Nanoparticles and Their Implication for Diminishing Cytotoxicity. *ACS Nano* **2012**, *6* (5), 4001–4012. https://doi.org/10.1021/nn300291r.

(27) Zhang, R.; Chen, L.; Liang, Q.; Xi, J.; Zhao, H.; Jin, Y.; Gao, X.; Yan, X.; Gao, L.; Fan, K. Unveiling the Active Sites on Ferrihydrite with Apparent Catalase-like Activity for Potentiating Radiotherapy. *Nano Today* **2021**, *41*. https://doi.org/10.1016/j.nantod.2021.101317.

(28) Li, J.; Liu, W.; Wu, X.; Gao, X. Mechanism of PH-Switchable Peroxidase and Catalase-like Activities of Gold, Silver, Platinum and Palladium. *Biomaterials* **2015**, *48*, 37–44. https://doi.org/10.1016/j.biomaterials.2015.01.012.

(29) Mu, J.; Wang, Y.; Zhao, M.; Zhang, L. Intrinsic Peroxidase-like Activity and Catalase-like Activity of Co3O4 Nanoparticles. *Chemical Communications* **2012**, *48* (19), 2540–2542. https://doi.org/10.1039/c2cc17013b.

(30) Pirmohamed, T.; Dowding, J. M.; Singh, S.; Wasserman, B.; Heckert, E.; Karakoti, A. S.; King, J. E. S.; Seal, S.; Self, W. T. Nanoceria Exhibit Redox State-Dependent Catalase Mimetic Activity. *Chemical Communications* **2010**, *46* (16), 2736–2738. https://doi.org/10.1039/b922024k.

(31) Dong, J.; Song, L.; Yin, J. J.; He, W.; Wu, Y.; Gu, N.; Zhang, Y. Co3O4 Nanoparticles with Multi-Enzyme Activities and Their Application in Immunohistochemical Assay. *ACS Appl Mater Interfaces* **2014**, *6* (3), 1959–1970. https://doi.org/10.1021/am405009f.

(32) Xu, B.; Cui, Y.; Wang, W.; Li, S.; Lyu, C.; Wang, S.; Bao, W.; Wang, H.; Qin, M.; Liu, Z.; Wei, W.; Liu, H. Immunomodulation-Enhanced Nanozyme-Based Tumor Catalytic Therapy. *Advanced Materials* **2020**, *32* (33). https://doi.org/10.1002/adma.202003563.

(33) Wang, M.; Chang, M.; Chen, Q.; Wang, D.; Li, C.; Hou, Z.; Lin, J.; Jin, D.; Xing, B. Au2Pt-PEG-Ce6 Nanoformulation with Dual Nanozyme Activities for Synergistic Chemodynamic Therapy / Phototherapy. *Biomaterials* **2020**, *252*. https://doi.org/10.1016/j.biomaterials.2020.120093.

(34) Wu, J.; Wang, X.; Wang, Q.; Lou, Z.; Li, S.; Zhu, Y.; Qin, L.; Wei, H. Nanomaterials with Enzyme-like Characteristics (Nanozymes): Next-Generation Artificial Enzymes (II). *Chemical Society Reviews*. Royal Society of Chemistry February 21, 2019, pp 1004–1076. https://doi.org/10.1039/c8cs00457a.

(35) Li, C.; Sun, Y.; Li, X.; Fan, S.; Liu, Y.; Jiang, X.; Boudreau, M. D.; Pan, Y.; Tian, X.; Yin, J. J. Bactericidal Effects and Accelerated Wound Healing Using Tb 4 O 7 Nanoparticles with Intrinsic Oxidase-like Activity. *J Nanobiotechnology* **2019**, *17* (1). https://doi.org/10.1186/s12951-019-0487-x.

(36) Li, D.; Liu, B.; Huang, P. J. J.; Zhang, Z.; Liu, J. Highly Active Fluorogenic Oxidase-Mimicking NiO Nanozymes. *Chemical Communications* **2018**, *54* (88), 12519–12522. https://doi.org/10.1039/c8cc07062h.

(37) Qin, W.; Su, L.; Yang, C.; Ma, Y.; Zhang, H.; Chen, X. Colorimetric Detection of Sulfite in Foods by a TMB-O2-Co 3O4 Nanoparticles Detection System. *J Agric Food Chem* **2014**, *62* (25), 5827–5834. https://doi.org/10.1021/jf500950p.

(38) You, J. G.; Liu, Y. W.; Lu, C. Y.; Tseng, W. L.; Yu, C. J. Colorimetric Assay of Heparin in Plasma Based on the Inhibition of Oxidase-like Activity of Citrate-Capped Platinum Nanoparticles. *Biosens Bioelectron* **2017**, *92*, 442–448. https://doi.org/10.1016/j.bios.2016.10.082.

(39) Zhang, P.; Sun, D.; Cho, A.; Weon, S.; Lee, S.; Lee, J.; Han, J. W.; Kim, D. P.; Choi, W. Modified Carbon Nitride Nanozyme as Bifunctional Glucose Oxidase-Peroxidase for Metal-Free Bioinspired Cascade Photocatalysis. *Nat Commun* **2019**, *10* (1). https://doi.org/10.1038/s41467-019-08731-y.

(40) Liu, L.; Du, J.; Liu, W. e.; Guo, Y.; Wu, G.; Qi, W.; Lu, X. Enhanced His@AuNCs Oxidase-like Activity by Reduced Graphene Oxide and Its Application for Colorimetric and Electrochemical Detection of Nitrite. *Anal Bioanal Chem* **2019**. https://doi.org/10.1007/s00216-019-01655-y.

(41) Han, Y.; Luo, L.; Zhang, L.; Kang, Y.; Sun, H.; Dan, J.; Sun, J.; Zhang, W.; Yue, T.; Wang, J. Oxidase-like Fe–Mn Bimetallic Nanozymes for Colorimetric Detection of Ascorbic Acid in Kiwi Fruit. *LWT* **2022**, *154*. https://doi.org/10.1016/j.lwt.2021.112821.

(42) Vernekar, A. A.; Das, T.; Ghosh, S.; Mugesh, G. A Remarkably Efficient MnFe2O4-Based Oxidase Nanozyme. *Chem Asian J* **2016**, *11* (1), 72–76. https://doi.org/10.1002/asia.201500942.

(43) Zhang, L.; Zhang, L.; Deng, H.; Li, H.; Tang, W.; Guan, L.; Qiu, Y.; Donovan, M. J.; Chen, Z.; Tan, W. In Vivo Activation of PH-Responsive Oxidase-like Graphitic Nanozymes for Selective Killing of Helicobacter Pylori. *Nat Commun* **2021**, *12* (1). https://doi.org/10.1038/s41467-021-22286-x.

(44) Zhu, M.; Wen, Y.; Song, S.; Zheng, A.; Li, J.; Sun, W.; Dai, Y.; Yin, K.; Sun, L. Synergistic Effects between Polyvinylpyrrolidone and Oxygen Vacancies on Improving the Oxidase-Mimetic Activity of Flower-like CeO2nanozymes. *Nanoscale* **2020**, *12* (37), 19104–19111. https://doi.org/10.1039/d0nr04177g.

(45) Yasui, K.; Baba, A. Therapeutic Potential of Superoxide Dismutase (SOD) for Resolution of Inflammation. *Inflammation Research*. September 2006, pp 359–363. https://doi.org/10.1007/s00011-006-5195-y.

(46) Qiu, H.; Gong, H.; Bao, Y.; Jiang, H.; Tong, W. Reactive Oxygen Species-Scavenging Hollow MnO2nanozymes as Carriers to Deliver Budesonide for Synergistic Inflammatory Bowel Disease Therapy. *Biomater Sci* **2022**, *10* (2), 457–466. https://doi.org/10.1039/d1bm01525g.

(47) Korsvik, C.; Patil, S.; Seal, S.; Self, W. T. Superoxide Dismutase Mimetic Properties Exhibited by Vacancy Engineered Ceria Nanoparticles. *Chemical Communications* **2007**, No. 10, 1056–1058. https://doi.org/10.1039/b615134e.

(48) He, W.; Zhou, Y. T.; Wamer, W. G.; Hu, X.; Wu, X.; Zheng, Z.; Boudreau, M. D.; Yin, J. J. Intrinsic Catalytic Activity of Au Nanoparticles with Respect to Hydrogen Peroxide Decomposition and Superoxide Scavenging. *Biomaterials* **2013**, *34* (3), 765–773. https://doi.org/10.1016/j.biomaterials.2012.10.010.

(49) Huang, Z.; He, K.; Song, Z.; Zeng, G.; Chen, A.; Yuan, L.; Li, H.; Hu, L.; Guo, Z.; Chen, G. Antioxidative Response of Phanerochaete Chrysosporium against Silver Nanoparticle-Induced Toxicity and Its Potential Mechanism. *Chemosphere* **2018**, *211*, 573–583. https://doi.org/10.1016/j.chemosphere.2018.07.192.

(50) Song, C.; Ding, W.; Zhao, W.; Liu, H.; Wang, J.; Yao, Y.; Yao, C. High Peroxidase-like Activity Realized by Facile Synthesis of FeS2 Nanoparticles for Sensitive Colorimetric Detection of H2O2 and Glutathione. *Biosens Bioelectron* **2020**, *151*, 111983. https://doi.org/10.1016/j.bios.2019.111983.

(51) Warkhade, S. K.; Singh, R. P.; Das, R. S.; Gaikwad, G. S.; Zodape, S. P.; Pratap, U. R.; Maldhure, A.; Wankhade, A. V. CoSe2 Nanoflakes: An Artificial Nanoenzyme with Excellent Peroxidase like Activity. *Inorg Chem Commun* **2021**, *126*, 108461. https://doi.org/10.1016/j.inoche.2021.108461.

(52) Yang, H.; Yang, R.; Zhang, P.; Qin, Y.; Chen, T.; Ye, F. A Bimetallic (Co/2Fe) Metal-Organic Framework with Oxidase and Peroxidase Mimicking Activity for Colorimetric Detection of Hydrogen Peroxide. *Microchimica Acta* **2017**, *184* (12), 4629–4635. https://doi.org/10.1007/s00604-017-2509-4.

(53) Wang, C.; Gao, J.; Cao, Y.; Tan, H. Colorimetric Logic Gate for Alkaline Phosphatase Based on Copper (II)-Based Metal-Organic Frameworks with Peroxidase-like Activity. *Anal Chim Acta* **2018**, *1004*, 74–81. https://doi.org/10.1016/j.aca.2017.11.078.

(54) Liang, L.; Zhao, Z.; Ye, F.; Zhao, S. Rapid and Sensitive Colorimetric Detection of Dopamine Based on the Enhanced-Oxidase Mimicking Activity of Cerium(Iv). *New Journal of Chemistry* **2021**, *45* (15), 6780–6786. https://doi.org/10.1039/d1nj00162k.

(55) Zhang, W.; Hu, S.; Yin, J. J.; He, W.; Lu, W.; Ma, M.; Gu, N.; Zhang, Y. Prussian Blue Nanoparticles as Multienzyme Mimetics and Reactive Oxygen Species Scavengers. *J Am Chem Soc* **2016**, *138* (18), 5860–5865. https://doi.org/10.1021/jacs.5b12070.

(56) Chen, T. M.; Wu, X. J.; Wang, J. X.; Yang, G. W. WSe2 Few Layers with Enzyme Mimic Activity for High-Sensitive and High-Selective Visual Detection of Glucose. *Nanoscale* **2017**, *9* (32), 11806–11813. https://doi.org/10.1039/c7nr03179c.

(57) Li, J.; Liu, W.; Wu, X.; Gao, X. Mechanism of PH-Switchable Peroxidase and Catalase-like Activities of Gold, Silver, Platinum and Palladium. *Biomaterials* **2015**, *48*, 37–44. https://doi.org/10.1016/j.biomaterials.2015.01.012.

(58) Mu, J.; Zhang, L.; Zhao, M.; Wang, Y. Co3O4 Nanoparticles as an Efficient Catalase Mimic: Properties, Mechanism and Its Electrocatalytic Sensing Application for Hydrogen Peroxide. *J Mol Catal A Chem* **2013**, *378*, 30–37. https://doi.org/10.1016/j.molcata.2013.05.016.

(59) Wang, C.; Li, Y.; Yang, W.; Zhou, L.; Wei, S. Nanozyme with Robust Catalase Activity by Multiple Mechanisms and Its Application for Hypoxic Tumor Treatment. *Adv Healthc Mater* **2021**, *10* (19). https://doi.org/10.1002/adhm.202100601.

(60) Zhang, X.; Huang, Y. Evaluation of the Antioxidant Activity of Phenols and Tannic Acid Determination with Mn3O4 Nano-Octahedrons as an Oxidase Mimic. *Analytical Methods* **2015**, *7* (20), 8640–8646. https://doi.org/10.1039/c5ay01732g.

(61) Zhang, X.; Yuan, A.; Mao, X.; Chen, Q.; Huang, Y. Engineered Mn/Co Oxides Nanocomposites by Cobalt Doping of Mn-BTC - New Oxidase Mimetic for Colorimetric Sensing of Acid Phosphatase. *Sens Actuators B Chem* **2019**, *299*. https://doi.org/10.1016/j.snb.2019.126928.

(62) Cui, M.; Zhao, Y.; Wang, C.; Song, Q. The Oxidase-like Activity of Iridium Nanoparticles, and Their Application to Colorimetric Determination of Dissolved Oxygen. *Microchimica Acta* **2017**, *184* (9), 3113–3119. https://doi.org/10.1007/s00604-017-2326-9.

(63) Comotti, M.; Della Pina, C.; Falletta, E.; Rossi, M. Aerobic Oxidation of Glucose with Gold Catalyst: Hydrogen Peroxide as Intermediate and Reagent. *Adv Synth Catal* **2006**, *348* (3), 313–316. https://doi.org/10.1002/adsc.200505389.

(64) Chen, J.; Ma, Q.; Li, M.; Chao, D.; Huang, L.; Wu, W.; Fang, Y.; Dong, S. Glucose-Oxidase like Catalytic Mechanism of Noble Metal Nanozymes. *Nat Commun* **2021**, *12* (1). https://doi.org/10.1038/s41467-021-23737-1.

(65) Ragg, R.; Natalio, F.; Tahir, M. N.; Janssen, H.; Kashyap, A.; Strand, D.; Strand, S.; Tremel, W. Molybdenum Trioxide Nanoparticles with Intrinsic Sulfite Oxidase Activity. *ACS Nano* **2014**, *8* (5), 5182–5189. https://doi.org/10.1021/nn501235j.

(66) Shen, X.; Liu, W.; Gao, X.; Lu, Z.; Wu, X.; Gao, X. Mechanisms of Oxidase and Superoxide Dismutation-like Activities of Gold, Silver, Platinum, and Palladium, and Their Alloys: A General Way to the Activation of Molecular Oxygen. *J Am Chem Soc* **2015**, *137* (50), 15882–15891. https://doi.org/10.1021/jacs.5b10346.

(67) Samuel, E. L. G.; Marcano, D. C.; Berka, V.; Bitner, B. R.; Wu, G.; Potter, A.; Fabian, R. H.; Pautler, R. G.; Kent, T. A.; Tsai, A. L.; Tour, J. M. Highly Efficient Conversion of Superoxide to Oxygen Using Hydrophilic Carbon Clusters. *Proc Natl Acad Sci U S A* **2015**, *112* (8), 2343–2348. https://doi.org/10.1073/pnas.1417047112.

(68) Guo, S.; Han, Y.; Guo, L. Mechanistic Study of Catalase- and Superoxide Dismutation-Mimic Activities of Cobalt Oxide Nanozyme from First-Principles Microkinetic Modeling. *Catalysis Surveys from Asia* **2020**, *24* (1), 70–85. https://doi.org/10.1007/s10563-019-09290-4.

(69) Duan, D.; Fan, K.; Zhang, D.; Tan, S.; Liang, M.; Liu, Y.; Zhang, J.; Zhang, P.; Liu, W.; Qiu, X.; Kobinger, G. P.; Fu Gao, G.; Yan, X. Nanozyme-Strip for Rapid Local Diagnosis of Ebola. *Biosens Bioelectron* **2015**, *74*, 134–141. https://doi.org/10.1016/j.bios.2015.05.025.

(70) Wang, L.; Hou, J.; Liu, S.; Carrier, A. J.; Guo, T.; Liang, Q.; Oakley, D.; Zhang, X. CuO Nanoparticles as Haloperoxidase-Mimics: Chloride-Accelerated Heterogeneous Cu-Fenton Chemistry for H2O2 and Glucose Sensing. *Sens Actuators B Chem* **2019**, *287*, 180–184. https://doi.org/10.1016/j.snb.2019.02.030.

(71) Sun, M.; He, M.; Jiang, S.; Wang, Y.; Wang, X.; Liu, T.; Song, C.; Wang, S.; Rao, H.; Lu, Z. Multi-Enzyme Activity of Three Layers FeOx@ZnMnFeOy@Fe-Mn Organogel for Colorimetric Detection of Antioxidants and Norfloxacin with Smartphone. *Chemical Engineering Journal* **2021**, *425*. https://doi.org/10.1016/j.cej.2021.131823.

(72) Boruah, P. K.; Darabdhara, G.; Das, M. R. Polydopamine Functionalized Graphene Sheets Decorated with Magnetic Metal Oxide Nanoparticles as Efficient Nanozyme for the Detection and Degradation of Harmful Triazine Pesticides. *Chemosphere* **2021**, *268*. https://doi.org/10.1016/j.chemosphere.2020.129328.

(73) Lyu, Z.; Ding, S.; Wang, M.; Pan, X.; Feng, Z.; Tian, H.; Zhu, C.; Du, D.; Lin, Y. Iron-Imprinted Single-Atomic Site Catalyst-Based Nanoprobe for Detection of Hydrogen Peroxide in Living Cells. *Nanomicro Lett* **2021**, *13* (1). https://doi.org/10.1007/s40820-021-00661-z.

(74) Zou, W.; Tang, Y.; Zeng, H.; Wang, C.; Wu, Y. Porous Co3O4 Nanodisks as Robust Peroxidase Mimetics in an Ultrasensitive Colorimetric Sensor for the Rapid Detection of Multiple Heavy Metal Residues in Environmental Water Samples. *J Hazard Mater* **2021**, *417*. https://doi.org/10.1016/j.jhazmat.2021.125994.

(75) Lu, Z.; Dang, Y.; Dai, C.; Zhang, Y.; Zou, P.; Du, H.; Zhang, Y.; Sun, M.; Rao, H.; Wang, Y. Hollow MnFeO Oxide Derived from MOF@MOF with Multiple Enzyme-like Activities for Multifunction Colorimetric Assay of Biomolecules and Hg2+. *J Hazard Mater* **2021**, *403*, 123979. https://doi.org/10.1016/j.jhazmat.2020.123979.

(76) Ahmed, S. R.; Corredor, J. C.; Nagy, É.; Neethirajan, S. Amplified Visual Immunosensor Integrated with Nanozyme for Ultrasensitive Detection of Avian Influenza Virus. *Nanotheranostics* **2017**, *1* (3), 338–345. https://doi.org/10.7150/ntno.20758.

(77) Mumtaz, S.; Wang, L. S.; Hussain, S. Z.; Abdullah, M.; Huma, Z.; Iqbal, Z.; Creran, B.; Rotello, V. M.; Hussain, I. Dopamine Coated Fe3O4 Nanoparticles as Enzyme Mimics for the Sensitive Detection of Bacteria. *Chemical Communications* **2017**, *53* (91), 12306–12308. https://doi.org/10.1039/c7cc07149c.

(78) Liu, D.; Ju, C.; Han, C.; Shi, R.; Chen, X.; Duan, D.; Yan, J.; Yan, X. Nanozyme Chemiluminescence Paper Test for Rapid and Sensitive Detection of SARS-CoV-2 Antigen. *Biosens Bioelectron* **2021**, *173*. https://doi.org/10.1016/j.bios.2020.112817.

(79) Liu, L.; Jiang, H.; Wang, X. Alkaline Phosphatase-Responsive Zn2+ Double-Triggered Nucleotide Capped Gold Nanoclusters/ Alginate Hydrogel with Recyclable Nanozyme Capability. *Biosens Bioelectron* **2021**, *173*. https://doi.org/10.1016/j.bios.2020.112786.

(80) Zhao, J.; Fu, C.; Huang, C.; Zhang, S.; Wang, F.; Zhang, Y.; Zhang, L.; Ge, S.; Yu, J. Co3O4-Au Polyhedron Mimic Peroxidase- and Cascade Enzyme-Assisted Cycling Process-Based Photoelectrochemical Biosensor for Monitoring of MiRNA-141. *Chemical Engineering Journal* **2021**, *406*. https://doi.org/10.1016/j.cej.2020.126892.

(81) Zhang, J.; Zhang, X.; Gao, Y.; Yan, J.; Song, W. Integrating CuO/g-C3N4 p-n Heterojunctioned Photocathode with MoS2 QDs@Cu NWs Multifunctional Signal Amplifier for Ultrasensitive Detection of AβO. *Biosens Bioelectron* **2021**, *176*. https://doi.org/10.1016/j.bios.2020.112945.

(82) Gu, Y.; Cao, Z.; Zhao, M.; Xu, Y.; Lu, N. Single-Atom Fe Nanozyme with Enhanced Oxidase-like Activity for the Colorimetric Detection of Ascorbic Acid and Glutathione. *Biosensors (Basel)* **2023**, *13* (4). https://doi.org/10.3390/bios13040487.

(83) Guo, A.; Sun, J.; Yan, M.; Wang, G. L. Sensitive Colorimetric Assay of T4 DNA Ligase by the Oxidase Nanozyme of LaMnO3.26 Coupled with a Hyperbranched Amplification Reaction. *Analyst* **2023**. https://doi.org/10.1039/d3an00195d.

(84) Wang, L.; Sun, Y.; Zhang, H.; Shi, W.; Huang, H.; Li, Y. Selective Sensing of Catechol Based on a Fluorescent Nanozyme with Catechol Oxidase Activity. *Spectrochim Acta A Mol Biomol Spectrosc* **2023**, *302*. https://doi.org/10.1016/j.saa.2023.123003.

(85) Li, H.; Wang, Z.; Zhao, J.; Guan, Y.; Liu, Y. Dual Colorimetric and Ratiometric Fluorescent Responses for the Determination of Glutathione Based on Fluorescence Quenching and Oxidase-like Activity of MnO2nanosheets. *ACS Sustain Chem Eng* **2020**, *8* (43), 16136–16142. https://doi.org/10.1021/acssuschemeng.0c04345.

(86) Zhang, L.; Qiao, C.; Cai, X.; Xia, Z.; Han, J.; Yang, Q.; Zhou, C.; Chen, S.; Gao, S. Microcalorimetry-Guided Pore-Microenvironment Optimization to Improve Sensitivity of Ni-MOF Electrochemical Bio-

sensor for Chiral Galantamine. *Chemical Engineering Journal* **2021**, *426*. https://doi.org/10.1016/j.cej.2021.130730.

(87) Liu, T.; Li, Z.; Chen, M.; Zhao, H.; Zheng, Z.; Cui, L.; Zhang, X. Sensitive Electrochemical Biosensor for Uracil-DNA Glycosylase Detection Based on Self-Linkable Hollow Mn/Ni Layered Doubled Hydroxides as Oxidase-like Nanozyme for Cascade Signal Amplification. *Biosens Bioelectron* **2021**, *194*. https://doi.org/10.1016/j.bios.2021.113607.

(88) Puiu, M.; Istrate, O. M.; Mirceski, V.; Bala, C. Ultrasensitive Detection of Hydrogen Peroxide Using Methylene Blue Grafted on Molecular Wires as Nanozyme with Catalase-like Activity. *Anal Chem* **2023**, *95* (44), 16185–16193. https://doi.org/10.1021/acs.analchem.3c02919.

(89) Ma, X.; Wang, Z.; Hu, X.; Chen, J.; Zhang, H.; Li, X.; Xie, F.; Xu, J. Nanozyme Catalysis-Powered Portable Mini-Drainage Device Enables Real-Time and Universal Weighing Analysis of Silver Ions and Silver Nanoparticles. *J Hazard Mater* **2021**, *415*. https://doi.org/10.1016/j.jhazmat.2021.125689.

(90) Fang, X.; Zhang, X.; Zhang, Z.; Hu, S.; Ye, F.; Zhao, S. Complementary Atomic Flame/Molecular Colorimetry Dual-Mode Assay for Sensitive and Wide-Range Detection of Cancer Cells. *Chemical Communications* **2021**, *57* (27), 3327–3330. https://doi.org/10.1039/d1cc00192b.

(91) Cai, X.; Shi, L.; Sun, W.; Zhao, H.; Li, H.; He, H.; Lan, M. A Facile Way to Fabricate Manganese Phosphate Self-Assembled Carbon Networks as Efficient Electrochemical Catalysts for Real-Time Monitoring of Superoxide Anions Released from HepG2 Cells. *Biosens Bioelectron* **2018**, *102*, 171–178. https://doi.org/10.1016/j.bios.2017.11.020.

(92) Ji, H.; Dong, K.; Yan, Z.; Ding, C.; Chen, Z.; Ren, J.; Qu, X. Bacterial Hyaluronidase Self-Triggered Prodrug Release for Chemo-Photothermal Synergistic Treatment of Bacterial Infection. *Small* **2016**, *12* (45), 6200–6206. https://doi.org/10.1002/smll.201601729.

(93) Xi, J.; Wei, G.; An, L.; Xu, Z.; Xu, Z.; Fan, L.; Gao, L. Copper/Carbon Hybrid Nanozyme: Tuning Catalytic Activity by the Copper State for Antibacterial Therapy. *Nano Lett* **2019**, *19* (11), 7645–7654. https://doi.org/10.1021/acs.nanolett.9b02242.

(94) Zheng, Y.; Liu, W.; Qin, Z.; Chen, Y.; Jiang, H.; Wang, X. Mercaptopyrimidine-Conjugated Gold Nanoclusters as Nanoantibiotics for Combating Multidrug-Resistant Superbugs. *Bioconjug Chem* **2018**, *29* (9), 3094–3103. https://doi.org/10.1021/acs.bioconjchem.8b00452.

(95) Khoshgozaran Roudbaneh, S. Z.; Kahbasi, S.; Sohrabi, M. J.; Hasan, A.; Salihi, A.; Mirzaie, A.; Niyazmand, A.; Qadir Nanakali, N. M.; Shekha, M. S.; Aziz, F. M.; Vaghar-Lahijani, G.; Keshtali, A. B.; Ehsani, E.; Rasti, B.; Falahati, M. Albumin Binding, Antioxidant and Antibacterial Effects of Cerium Oxide Nanoparticles. *J Mol Liq* **2019**, *296*. https://doi.org/10.1016/j.molliq.2019.111839.

(96) Karim, M. N.; Singh, M.; Weerathunge, P.; Bian, P.; Zheng, R.; Dekiwadia, C.; Ahmed, T.; Walia, S.; Della Gaspera, E.; Singh, S.; Ramanathan, R.; Bansal, V. Visible-Light-Triggered Reactive-Oxygen-Species-Mediated Antibacterial Activity of Peroxidase-Mimic CuO Nanorods. *ACS Appl Nano Mater* **2018**, *1* (4), 1694–1704. https://doi.org/10.1021/acsanm.8b00153.

(97) Huang, X. W.; Wei, J. J.; Liu, T.; Zhang, X. L.; Bai, S. M.; Yang, H. H. Silk Fibroin-Assisted Exfoliation and Functionalization of Transition Metal Dichalcogenide Nanosheets for Antibacterial Wound Dressings. *Nanoscale* **2017**, *9* (44), 17193–17198. https://doi.org/10.1039/c7nr06807g.

(98) Li, C.; Sun, Y.; Li, X.; Fan, S.; Liu, Y.; Jiang, X.; Boudreau, M. D.; Pan, Y.; Tian, X.; Yin, J. J. Bactericidal Effects and Accelerated Wound Healing Using Tb 4 O 7 Nanoparticles with Intrinsic Oxidase-like Activity. *J Nanobiotechnology* **2019**, *17* (1). https://doi.org/10.1186/s12951-019-0487-x.

(99) Kumar, V.; Abbas, Abul. K.; Aster, Jon. C. *Robbins Basic Patholoy*, 11th ed.; Elsevier: Philadelphia, 2018.

(100) Kwon, H. J.; Kim, D.; Seo, K.; Kim, Y. G.; Han, S. I.; Kang, T.; Soh, M.; Hyeon, T. Ceria Nanoparticle Systems for Selective Scavenging of Mitochondrial, Intracellular, and Extracellular Reactive Oxygen

Species in Parkinson's Disease. *Angewandte Chemie* **2018**, *130* (30), 9552–9556. https://doi.org/10.1002/ange.201805052.

(101) Singh, N.; Savanur, M. A.; Srivastava, S.; D'Silva, P.; Mugesh, G. A Manganese Oxide Nanozyme Prevents the Oxidative Damage of Biomolecules without Affecting the Endogenous Antioxidant System. *Nanoscale* **2019**, *11* (9), 3958–3967. https://doi.org/10.1039/c8nr09397k.

(102) Singh; Savanur, M. A.; Srivastava, S.; D'Silva, P.; Mugesh, G. A Redox Modulatory Mn 3 O 4 Nanozyme with Multi-Enzyme Activity Provides Efficient Cytoprotection to Human Cells in a Parkinson's Disease Model . *Angewandte Chemie* **2017**, *129* (45), 14455–14459. https://doi.org/10.1002/ange.201708573.

(103) Xiong, B.; Xu, R.; Zhou, R.; He, Y.; Yeung, E. S. Preventing UV Induced Cell Damage by Scavenging Reactive Oxygen Species with Enzyme-Mimic Au-Pt Nanocomposites. *Talanta* **2014**, *120*, 262–267. https://doi.org/10.1016/j.talanta.2013.12.020.

(104) Dugan, L. L.; Tian, L. L.; Quick, K. L.; Hardt, J. I.; Karimi, M.; Brown, C.; Loftin, S.; Flores, H.; Moerlein, S. M.; Polich, J.; Tabbal, S. D.; Mink, J. W.; Perlmutter, J. S. Carboxyfullerene Neuroprotection Postinjury in Parkinsonian Nonhuman Primates. *Ann Neurol* **2014**, *76* (3), 393–402. https://doi.org/10.1002/ana.24220.

(105) Wu, C.; Han, X.; Feng, W.; Liu, Z.; Chen, L.; Zhou, B.; Chen, Y.; Shi, J. Multi-Enzymatic Activities of Ultrasmall Ruthenium Oxide for Anti-Inflammation and Neuroprotection. *Chemical Engineering Journal* **2021**, *411*. https://doi.org/10.1016/j.cej.2021.128543.

(106) Fan, K.; Cao, C.; Pan, Y.; Lu, D.; Yang, D.; Feng, J.; Song, L.; Liang, M.; Yan, X. Magnetoferritin Nanoparticles for Targeting and Visualizing Tumour Tissues. *Nat Nanotechnol* **2012**, *7* (7), 459–464. https://doi.org/10.1038/nnano.2012.90.

(107) Qin, R.; Feng, Y.; Ding, D.; Chen, L.; Li, S.; Deng, H.; Chen, S.; Han, Z.; Sun, W.; Chen, H. Fe-Coordinated Carbon Nanozyme Dots as Peroxidase-Like Nanozymes and Magnetic Resonance Imaging Contrast Agents. *ACS Appl Bio Mater* **2021**, *4* (7), 5520–5528. https://doi.org/10.1021/acsabm.1c00336.

(108) Zhen, W.; Liu, Y.; Lin, L.; Bai, J.; Jia, X.; Tian, H.; Jiang, X. BSA-IrO 2 : Catalase-like Nanoparticles with High Photothermal Conversion Efficiency and a High X-ray Absorption Coefficient for Anti-inflammation and Antitumor Theranostics . *Angewandte Chemie* **2018**, *130* (32), 10466–10470. https://doi.org/10.1002/ange.201804466.

(109) Zeng, L.; Han, Y.; Chen, Z.; Jiang, K.; Golberg, D.; Weng, Q. Biodegradable and Peroxidase-Mimetic Boron Oxynitride Nanozyme for Breast Cancer Therapy. *Advanced Science* **2021**, *8* (16). https://doi.org/10.1002/advs.202101184.

(110) Wang, C.; Li, Y.; Yang, W.; Zhou, L.; Wei, S. Nanozyme with Robust Catalase Activity by Multiple Mechanisms and Its Application for Hypoxic Tumor Treatment. *Adv Healthc Mater* **2021**, *10* (19). https://doi.org/10.1002/adhm.202100601.

(111) Xu, Z.; Chen, J.; Li, Y.; Hu, T.; Fan, L.; Xi, J.; Han, J.; Guo, R. Yolk-Shell Fe3O4@Carbon@Platinum-Chlorin E6 Nanozyme for MRI-Assisted Synergistic Catalytic-Photodynamic-Photothermal Tumor Therapy. *J Colloid Interface Sci* **2022**, *628*, 1033–1043. https://doi.org/10.1016/j.jcis.2022.08.006.

(112) Huang, Y.; Ren, J.; Qu, X. Nanozymes: Classification, Catalytic Mechanisms, Activity Regulation, and Applications. *Chem Rev* **2019**, *119* (6), 4357–4412. https://doi.org/10.1021/acs.chemrev.8b00672.

(113) Li, Y.; Liu, J. Nanozyme's Catching up: Activity, Specificity, Reaction Conditions and Reaction Types. *Materials Horizons*. Royal Society of Chemistry February 1, 2021, pp 336–350. https://doi.org/10.1039/d0mh01393e.

(114) Somerville, S. V.; Li, Q.; Wordsworth, J.; Jamali, S.; Eskandarian, M. R.; Tilley, R. D.; Gooding, J. J. Approaches to Improving the Selectivity of Nanozymes. *Advanced Materials* **2024**, *36* (10). https://doi.org/10.1002/adma.202211288.

(115) Fan, H.; Zhang, R.; Fan, K.; Gao, L.; Yan, X. Exploring the Specificity of Nanozymes. *ACS Nano*. American Chemical Society January 30, 2024, pp 2533–2540. https://doi.org/10.1021/acsnano.3c07680.

(116) Goya, G. F.; Mayoral, A.; Winkler, E.; Zysler, R. D.; Bagnato, C.; Raineri, M.; Fuentes-García, J. A.; Lima, E. Next Generation of Nanozymes: A Perspective of the Challenges to Match Biological Performance. *J Appl Phys* **2021**, *130* (19). https://doi.org/10.1063/5.0061499.

(117) Chen, M.; Zhou, X.; Xiong, C.; Yuan, T.; Wang, W.; Zhao, Y.; Xue, Z.; Guo, W.; Wang, Q.; Wang, H.; Li, Y.; Zhou, H.; Wu, Y. Facet Engineering of Nanoceria for Enzyme-Mimetic Catalysis. *ACS Appl Mater Interfaces* **2022**, *14* (19), 21989–21995. https://doi.org/10.1021/acsami.2c04320.

(118) Wang, Z.; Zhang, R.; Yan, X.; Fan, K. Structure and Activity of Nanozymes: Inspirations for de Novo Design of Nanozymes. *Materials Today*. Elsevier B.V. December 1, 2020, pp 81–119. https://doi.org/10.1016/j.mattod.2020.08.020.

(119) Zhang, W.; Dong, J.; Wu, Y.; Cao, P.; Song, L.; Ma, M.; Gu, N.; Zhang, Y. Shape-Dependent Enzyme-like Activity of Co3O4 Nanoparticles and Their Conjugation with His-Tagged EGFR Single-Domain Antibody. *Colloids Surf B Biointerfaces* **2017**, *154*, 55–62. https://doi.org/10.1016/j.colsurfb.2017.02.034.

(120) Luo, W.; Zhu, C.; Su, S.; Li, D.; He, Y.; Huang, Q.; Fan, C. Self-Catalyzed, Self-Limiting Growth of Glucose Oxidase-Mimicking Gold Nanoparticles. *ACS Nano* **2010**, *4* (12), 7451–7458. https://doi.org/10.1021/nn102592h.

(121) Zhao, J.; Zhang, S.; Wang, D.; Jia, C.; Yang, P. Synthesis of Rhombic Dodecahedral Fe3O4 Single Crystals towards Their High Peroxidase-like Activity. *J Nanosci Nanotechnol* **2016**, *16* (8), 8846–8853. https://doi.org/10.1166/jnn.2016.11904.

(122) Wordsworth, J.; Benedetti, T. M.; Alinezhad, A.; Tilley, R. D.; Edwards, M. A.; Schuhmann, W.; Gooding, J. J. The Importance of Nanoscale Confinement to Electrocatalytic Performance. *Chem Sci* **2020**, *11* (5), 1233–1240. https://doi.org/10.1039/c9sc05611d.

(123) Benedetti, T. M.; Andronescu, C.; Cheong, S.; Wilde, P.; Wordsworth, J.; Kientz, M.; Tilley, R. D.; Schuhmann, W.; Gooding, J. J. Electrocatalytic Nanoparticles That Mimic the Three-Dimensional Geometric Architecture of Enzymes: Nanozymes. *J Am Chem Soc* **2018**, *140* (41), 13449–13455. https://doi.org/10.1021/jacs.8b08664.

(124) Qileng, A.; Chen, S.; Liang, H.; Shen, H.; Chen, M.; Liu, W.; Liu, Y. Bionic Structural Design of Pt Nanozymes with the Nano-Confined Effect for the Precise Recognition of Copper Ion. *Chemical Engineering Journal* **2023**, *455*. https://doi.org/10.1016/j.cej.2022.140769.

(125) Li, Z.; Liu, F.; Jiang, Y.; Ni, P.; Zhang, C.; Wang, B.; Chen, C.; Lu, Y. Single-Atom Pd Catalysts as Oxidase Mimics with Maximum Atom Utilization for Colorimetric Analysis. *Nano Res* **2022**, *15* (5), 4411–4420. https://doi.org/10.1007/s12274-021-4029-0.

(126) Ji, S.; Jiang, B.; Hao, H.; Chen, Y.; Dong, J.; Mao, Y.; Zhang, Z.; Gao, R.; Chen, W.; Zhang, R.; Liang, Q.; Li, H.; Liu, S.; Wang, Y.; Zhang, Q.; Gu, L.; Duan, D.; Liang, M.; Wang, D.; Yan, X.; Li, Y. Matching the Kinetics of Natural Enzymes with a Single-Atom Iron Nanozyme. *Nat Catal* **2021**, *4* (5), 407–417. https://doi.org/10.1038/s41929-021-00609-x.

(127) Chen, F.; Wu, X. L.; Shi, C.; Lin, H.; Chen, J.; Shi, Y.; Wang, S.; Duan, X. Molecular Engineering toward Pyrrolic N-Rich M-N4 (M = Cr, Mn, Fe, Co, Cu) Single-Atom Sites for Enhanced Heterogeneous Fenton-Like Reaction. *Adv Funct Mater* **2021**, *31* (13). https://doi.org/10.1002/adfm.202007877.

(128) Liu, C. P.; Chen, K. C.; Su, C. F.; Yu, P. Y.; Lee, P. W. Revealing the Active Site of Gold Nanoparticles for the Peroxidase-like Activity: The Determination of Surface Accessibility. *Catalysts* **2019**, *9* (6). https://doi.org/10.3390/catal9060517.

(129) Long, Y. J.; Li, Y. F.; Liu, Y.; Zheng, J. J.; Tang, J.; Huang, C. Z. Visual Observation of the Mercury-Stimulated Peroxidase Mimetic Activity of Gold Nanoparticles. *Chemical Communications* **2011**, *47* (43), 11939–11941. https://doi.org/10.1039/c1cc14294a.

(130) Fan, K.; Wang, H.; Xi, J.; Liu, Q.; Meng, X.; Duan, D.; Gao, L.; Yan, X. Optimization of Fe3O4 Nanozyme Activity via Single Amino Acid Modification Mimicking an Enzyme Active Site. *Chemical Communications* **2017**, *53* (2), 424–427. https://doi.org/10.1039/c6cc08542c.

(131) Sun, Y.; Xie, Z.; Pei, F.; Hu, W.; Feng, S.; Hao, Q.; Liu, B.; Mu, X.; Lei, W.; Tong, Z. Trimetallic Au@Pd@Pt Nanozyme-Enhanced Lateral Flow Immunoassay for the Detection of SARS-CoV-2 Nucleocapsid Protein. *Analytical Methods* **2022**, *14*, 5091–5099. https://doi.org/10.1039/d2ay01530g.

(132) Wu, K.; Zhu, D.; Dai, X.; Wang, W.; Zhong, X.; Fang, Z.; Peng, C.; Wei, X.; Qian, H.; Chen, X.; Wang, X.; Zha, Z.; Cheng, L. Bimetallic Oxide Cu1.5Mn1.5O4 Cage-like Frame Nanospheres with Triple Enzyme-like Activities for Bacterial-Infected Wound Therapy. *Nano Today* **2022**, *43*, 101380. https://doi.org/10.1016/j.nantod.2022.101380.

(133) Shang, C.; Wang, Q.; Tan, H.; Lu, S.; Wang, S.; Zhang, Q.; Gu, L.; Li, J.; Wang, E.; Guo, S. Defective PtRuTe As Nanozyme with Selectively Enhanced Peroxidase-like Activity. *JACS Au* **2022**, *2* (11), 2453–2459. https://doi.org/10.1021/jacsau.2c00495.

(134) Tao, H.; Chen, X.; Li, R.; Wang, Z.; Zhao, X.; Liu, C.; Duan, S.; Wang, X. A Flexible Visual Detection of Calcium Peroxide in Flour Employing Enhanced Catalytic Activity of Heterogeneous Catalysts Binary Copper Trapped Silica-Layered Magnetite Nanozyme. *Colloids Surf B Biointerfaces* **2022**, *219*. https://doi.org/10.1016/j.colsurfb.2022.112823.

(135) Shah, J.; Singh, S. Unveiling the Role of ATP in Amplification of Intrinsic Peroxidase-like Activity of Gold Nanoparticles. *3 Biotech* **2018**, *8* (1). https://doi.org/10.1007/s13205-017-1082-1.

(136) Wu, Y.; Zhong, H.; Xu, W.; Su, R.; Qin, Y.; Qiu, Y.; Zheng, L.; Gu, W.; Hu, L.; Lv, F.; Zhang, S.; Beckman, S. P.; Lin, Y.; Zhu, C.; Guo, S. Harmonizing Enzyme-like Cofactors to Boost Nanozyme Catalysis. *Angewandte Chemie - International Edition* **2024**, *63* (11). https://doi.org/10.1002/anie.202319108.

(137) Huang, Y. Q.; Fu, S.; Wang, Y. S.; Xue, J. H.; Xiao, X. L.; Chen, S. H.; Zhou, B. Protamine-Gold Nanoclusters as Peroxidase Mimics and the Selective Enhancement of Their Activity by Mercury Ions for Highly Sensitive Colorimetric Assay of Hg(II). *Anal Bioanal Chem* **2018**, *410* (28), 7385–7394. https://doi.org/10.1007/s00216-018-1344-8.

(138) Zhu, M.; Wang, M.; Qi, W.; Su, R.; He, Z. Constructing Peptide-Based Artificial Hydrolases with Customized Selectivity. *J Mater Chem B* **2019**, *7* (24), 3804–3810. https://doi.org/10.1039/c9tb00408d.

(139) Zhang, Z.; Zhang, X.; Liu, B.; Liu, J. Molecular Imprinting on Inorganic Nanozymes for Hundred-Fold Enzyme Specificity. *J Am Chem Soc* **2017**, *139* (15), 5412–5419. https://doi.org/10.1021/jacs.7b00601.

(140) He, X.; Luo, Q.; Guo, Z.; Li, Y.; Liu, Z. Construction of DNA Ligase-Mimicking Nanozymes via Molecular Imprinting. *J Mater Chem B* **2022**, *10* (35), 6716–6723. https://doi.org/10.1039/d1tb02325j.

(141) Sun, Y.; Zhao, C.; Gao, N.; Ren, J.; Qu, X. Stereoselective Nanozyme Based on Ceria Nanoparticles Engineered with Amino Acids. *Chemistry - A European Journal* **2017**, *23* (72), 18146–18150. https://doi.org/10.1002/chem.201704579.

(142) Jiang, W.; Li, Q.; Zhang, R.; Li, J.; Lin, Q.; Li, J.; Zhou, X.; Yan, X.; Fan, K. Chiral Metal-Organic Frameworks Incorporating Nanozymes as Neuroinflammation Inhibitors for Managing Parkinson's Disease. *Nat Commun* **2023**, *14* (1). https://doi.org/10.1038/s41467-023-43870-3.

(143) Ma, Q.; Cheng, C.; Luo, D.; Qiao, J.; Qi, L. Dipeptide-Capped Copper Nanoparticles as Chiral Nanozymes for Colorimetric Enantioselective Recognition of 3,4-Dihydroxy-d,l-Phenylalanine. *ACS Appl Bio Mater* **2023**, *6* (4), 1676–1682. https://doi.org/10.1021/acsabm.3c00118.

(144) Li, S.; Zhao, X.; Yu, X.; Wan, Y.; Yin, M.; Zhang, W.; Cao, B.; Wang, H. Fe3O4 Nanozymes with Aptamer-Tuned Catalysis for Selective Colorimetric Analysis of ATP in Blood. *Anal Chem* **2019**. https://doi.org/10.1021/acs.analchem.9b04116.

(145) Ouyang, Y.; Biniuri, Y.; Fadeev, M.; Zhang, P.; Carmieli, R.; Vázquez-González, M.; Willner, I. Aptamer-Modified Cu2+-Functionalized C-Dots: Versatile Means to Improve Nanozyme Activities-"Aptananozymes". *J Am Chem Soc* **2021**, *143* (30), 11510–11519. https://doi.org/10.1021/jacs.1c03939.

(146) Ouyang, Y.; Fadeev, M.; Zhang, P.; Carmieli, R.; Li, J.; Sohn, Y. S.; Karmi, O.; Nechushtai, R.; Pikarsky, E.; Fan, C.; Willner, I. Aptamer-Modified Au Nanoparticles: Functional Nanozyme Bioreactors for Cascaded Catalysis and Catalysts for Chemodynamic Treatment of Cancer Cells. *ACS Nano* **2022**, *16* (11), 18232–18243. https://doi.org/10.1021/acsnano.2c05710.

(147) Alrozi, R.; Zubir, A.; Khairul, M.; Selamat, A.; Zakarya, N.; Paisan, S. *Effect of Cobalt Substitution on Catalytic Activity of Fe 3-X Co x O 4 Catalyst*; 2018; Vol. 5.

(148) Liang, X.; He, Z.; Zhong, Y.; Tan, W.; He, H.; Yuan, P.; Zhu, J.; Zhang, J. The Effect of Transition Metal Substitution on the Catalytic Activity of Magnetite in Heterogeneous Fenton Reaction: In Interfacial View. *Colloids Surf A Physicochem Eng Asp* **2013**, *435*, 28–35. https://doi.org/10.1016/j.colsurfa.2012.12.038.

(149) Vetr, F.; Moradi-Shoeili, Z.; Özkar, S. Oxidation of O-Phenylenediamine to 2,3-Diaminophenazine in the Presence of Cubic Ferrites MFe2O4 (M = Mn, Co, Ni, Zn) and the Application in Colorimetric Detection of H2O2. *Appl Organomet Chem* **2018**, *32*, e4465. https://doi.org/10.1002/aoc.4465.

(150) Zhang, K.; Zuo, W.; Wang, Z.; Liu, J.; Li, T.; Wang, B.; Yang, Z. A Simple Route to CoFe2O4 Nanoparticles with Shape and Size Control and Their Tunable Peroxidase-like Activity. *RSC Adv* **2015**, *5* (14), 10632–10640. https://doi.org/10.1039/c4ra15675g.

(151) Shi, W.; Zhang, X.; He, S.; Huang, Y. CoFe2O4 Magnetic Nanoparticles as a Peroxidase Mimic Mediated Chemiluminescence for Hydrogen Peroxide and Glucose. *Chemical Communications* **2011**, *47* (38), 10785–10787. https://doi.org/10.1039/c1cc14300j.

(152) Sahoo, R.; Santra, S.; Ray, C.; Pal, A.; Negishi, Y.; Ray, S. K.; Pal, T. Hierarchical Growth of ZnFe2O4 for Sensing Applications. *New Journal of Chemistry* **2016**, *40* (2), 1861–1871. https://doi.org/10.1039/c5nj02547h.

(153) Chen, D.; Jiang, L.; Lei, T.; Xiao, G.; Wang, Y.; Zuo, X.; Li, B.; Li, L.; Wang, J. Magnetic CuFe2O4 with Intrinsic Protease-like Activity Inhibited Cancer Cell Proliferation and Migration through Mediating Intracellular Proteins. *Biomaterials and Biosystems* **2022**, *5*, 100038. https://doi.org/10.1016/j.bbiosy.2021.100038.

(154) Xia, F.; Shi, Q.; Nan, Z. Facile Synthesis of Cu-CuFe2O4nanozymes for Sensitive Assay of H2O2and GSH. *Dalton Transactions* **2020**, *49* (36), 12780–12792. https://doi.org/10.1039/d0dt02395g.

(155) Su, L.; Qin, W.; Zhang, H.; Rahman, Z. U.; Ren, C.; Ma, S.; Chen, X. The Peroxidase/Catalase-like Activities of MFe2O4 (M=Mg, Ni, Cu) MNPs and Their Application in Colorimetric Biosensing of Glucose. *Biosens Bioelectron* **2015**, *63*, 384–391. https://doi.org/10.1016/J.BIOS.2014.07.048.

(156) Wang, Y.; Li, H.; Guo, L.; Jiang, Q.; Liu, F. A Cobalt-Doped Iron Oxide Nanozyme as a Highly Active Peroxidase for Renal Tumor Catalytic Therapy. *RSC Adv* **2019**, *9* (33), 18815–18822. https://doi.org/10.1039/c8ra05487h.

(157) Wang, J.; Huang, F.; Wang, X.; Wan, Y.; Xue, Y.; Cai, N.; Chen, W.; Yu, F. Hierarchically Structured Fe3O4-Doped MnO2 Microspheres as an Enhanced Peroxidase-like Catalyst for Low Limit of Detection. *Process Biochemistry* **2019**, *83*, 35–43. https://doi.org/10.1016/j.procbio.2019.05.014.

(158) Li, S.; Shang, L.; Xu, B.; Wang, S.; Gu, K.; Wu, Q.; Sun, Y.; Zhang, Q.; Yang, H.; Zhang, F.; Gu, L.; Zhang, T.; Liu, H. A Nanozyme with Photo-Enhanced Dual Enzyme-Like Activities for Deep Pancreatic Cancer

Therapy. *Angewandte Chemie* **2019**, *131* (36), 12754–12761. https://doi.org/10.1002/ange.201904751.

(159) Gao, M.; Lu, X.; Chen, S.; Tian, D.; Zhu, Y.; Wang, C. Enhanced Peroxidase-like Activity of Mo6+-Doped Co3O4 Nanotubes for Ultrasensitive and Colorimetric l -Cysteine Detection. *ACS Appl Nano Mater* **2018**, *1* (9), 4703–4715. https://doi.org/10.1021/acsanm.8b00945.

(160) Zhang, X.; Lu, Y.; Chen, Q.; Huang, Y. A Tunable Bifunctional Hollow Co3O4/MO3(M = Mo, W) Mixed-Metal Oxide Nanozyme for Sensing H2O2and Screening Acetylcholinesterase Activity and Its Inhibitor. *J Mater Chem B* **2020**, *8* (30), 6459–6468. https://doi.org/10.1039/d0tb01337d.

(161) Isho, R. D.; Sher Mohammad, N. M.; Omer, K. M. Enhancing Enzymatic Activity of Mn@Co3O4 Nanosheets as Mimetic Nanozyme for Colorimetric Assay of Ascorbic Acid. *Anal Biochem* **2022**, *654*, 114818. https://doi.org/10.1016/j.ab.2022.114818.

(162) Cao, X.; Liu, M.; Zhao, M.; Li, J.; Xia, J.; Zou, T.; Wang, Z. Synergetic PtNP@Co3O4 Hollow Nanopolyhedrals as Peroxidase-like Nanozymes for the Dual-Channel Homogeneous Biosensing of Prostate-Specific Antigen. *Anal Bioanal Chem* **2022**, *414* (5), 1921–1932. https://doi.org/10.1007/s00216-021-03827-1.

(163) Chen, J.; Wei, X.; Tang, H.; Munyemana, J. C.; Guan, M.; Zhang, S.; Qiu, H. Deep Eutectic Solvents-Assisted Synthesis of ZnCo2O4 Nanosheets as Peroxidase-like Nanozyme and Its Application in Colorimetric Logic Gate. *Talanta* **2021**, *222*, 12168. https://doi.org/10.1016/j.talanta.2020.121680.

(164) Yin, D.; Yang, H.; Wang, S.; Yang, Z.; Liu, Q.; Zhang, X.; Zhang, X. Ce-Doped ZnCo2O4 Nanospheres: Synthesis, Double Enzyme-like Performances, Catalytic Mechanism and Fast Colorimetric Determination for Glutathione. *Colloids Surf A Physicochem Eng Asp* **2020**, *607*, 125466. https://doi.org/10.1016/j.colsurfa.2020.125466.

(165) Wei, X.; Chen, J.; Ali, M. C.; Munyemana, J. C.; Qiu, H. Cadmium Cobaltite Nanosheets Synthesized in Basic Deep Eutectic Solvents with Oxidase-like, Peroxidase-like, and Catalase-like Activities and Application in the Colorimetric Assay of Glucose. *Microchimica Acta* **2020**, *187*, 314. https://doi.org/10.1007/s00604-020-04298-4.

(166) Mu, Q.; Sun, Y.; Guo, A.; Xu, X.; Qin, B.; Cai, A. A Bifunctionalized NiCo2O4-Au Composite: Intrinsic Peroxidase and Oxidase Catalytic Activities for Killing Bacteria and Disinfecting Wound. *J Hazard Mater* **2021**, *402*. https://doi.org/10.1016/j.jhazmat.2020.123939.

(167) Bhagat, S.; Srikanth Vallabani, N. V.; Shutthanandan, V.; Bowden, M.; Karakoti, A. S.; Singh, S. Gold Core/Ceria Shell-Based Redox Active Nanozyme Mimicking the Biological Multienzyme Complex Phenomenon. *J Colloid Interface Sci* **2018**, *513*, 831–842. https://doi.org/10.1016/j.jcis.2017.11.064.

(168) Jiang, L.; Tinoco, M.; Fernández-García, S.; Sun, Y.; Traviankina, M.; Nan, P.; Xue, Q.; Pan, H.; Aguinaco, A.; González-Leal, J. M.; Blanco, G.; Blanco, E.; Hungría, A. B.; Calvino, J. J.; Chen, X. Enhanced Artificial Enzyme Activities on the Reconstructed Sawtoothlike Nanofacets of Pure and Pr-Doped Ceria Nanocubes. *ACS Appl Mater Interfaces* **2021**, *13* (32), 38061–38073. https://doi.org/10.1021/acsami.1c09992.

(169) Frerichs, H.; Pütz, E.; Pfitzner, F.; Reich, T.; Gazanis, A.; Panthöfer, M.; Hartmann, J.; Jegel, O.; Heermann, R.; Tremel, W. Nanocomposite Antimicrobials Prevent Bacterial Growth through the Enzyme-like Activity of Bi-Doped Cerium Dioxide (Ce1-: XBixO2- δ). *Nanoscale* **2020**, *12* (41), 21344–21358. https://doi.org/10.1039/d0nr06165d.

(170) Zhang, S.; Liu, Y.; Sun, S.; Wang, J.; Li, Q.; Yan, R.; Gao, Y.; Liu, H.; Liu, S.; Hao, W.; Dai, H.; Liu, C.; Sun, Y.; Long, W.; Mu, X.; Zhang, X. D. Catalytic Patch with Redox Cr/CeO2 Nanozyme of Noninvasive Intervention for Brain Trauma. *Theranostics* **2021**, *11* (6), 2806–2821. https://doi.org/10.7150/THNO.51912.

(171) Yue, Y.; Wei, H.; Guo, J.; Yang, Y. Ceria-Based Peroxidase-Mimicking Nanozyme with Enhanced Activity: A Coordination Chemistry Strategy. *Colloids Surf A Physicochem Eng Asp* **2021**, *610*, 125715. https://doi.org/10.1016/j.colsurfa.2020.125715.

(172) Liu, X.; Yang, J.; Cheng, J.; Xu, Y.; Chen, W.; Li, Y. Facile Preparation of Four-in-One Nanozyme Catalytic Platform and the Application in Selective Detection of Catechol and Hydroquinone. *Sens Actuators B Chem* **2021**, *337*, 129763. https://doi.org/10.1016/j.snb.2021.129763.

(173) Parmekar, M. V.; Salker, A. V. Highly Tuned Cobalt-Doped MnO2 Nanozyme as Remarkably Efficient Uricase Mimic. *Applied Nanoscience (Switzerland)* **2020**, *10* (1), 317–328. https://doi.org/10.1007/s13204-019-01118-x.

(174) Wang, X.; Cao, W.; Qin, L.; Lin, T.; Chen, W.; Lin, S.; Yao, J.; Zhao, X.; Zhou, M.; Hang, C.; Wei, H. Boosting the Peroxidase-like Activity of Nanostructured Nickel by Inducing Its 3+ Oxidation State in LaNiO3 Perovskite and Its Application for Biomedical Assays. *Theranostics* **2017**, *7* (8), 2277–2286. https://doi.org/10.7150/thno.19257.

(175) Mao, Y.; Jia, F.; Jing, T.; Li, T.; Jia, H.; He, W. Enhanced Multiple Enzymelike Activity of PtPdCu Trimetallic Nanostructures for Detection of Fe2+and Evaluation of Antioxidant Capability. *ACS Sustain Chem Eng* **2021**, *9* (1), 569–579. https://doi.org/10.1021/acssuschemeng.0c08230.

(176) Chen, C.; Wang, Y.; Zhang, D. Bifunctional Nanozyme Activities of Layered Double Hydroxide Derived Co-Al-Ce Mixed Metal Oxides for Antibacterial Application. *J Oceanol Limnol* **2020**, *38* (4), 1233–1245. https://doi.org/10.1007/s00343-020-0041-6.

(177) Xi, Z.; Gao, W.; Xia, X. Size Effect in Pd−Ir Core-Shell Nanoparticles as Nanozymes. *ChemBioChem* **2020**, *21* (17), 2440–2444. https://doi.org/10.1002/cbic.202000147.

(178) He, J.; He, D.; Yang, L.; Wu, G. L.; Tian, J.; Liu, Y.; Wang, W. Preparation of Urchin-like Pd-Pt-Ir Nanozymes and Their Application for the Detection of Ascorbic Acid and Hydrogen Peroxide. *Mater Lett* **2022**, *314*, 131851. https://doi.org/10.1016/j.matlet.2022.131851.

(179) Jin, L.; Sun, Y.; Shi, L.; Li, C.; Shen, Y. PdPt Bimetallic Nanowires with Efficient Oxidase Mimic Activity for the Colorimetric Detection of Acid Phosphatase in Acidic Media. *J Mater Chem B* **2019**, *7* (29), 4561–4567. https://doi.org/10.1039/c9tb00730j.

(180) Gharib, M.; Kornowski, A.; Noei, H.; Parak, W. J.; Chakraborty, I. Protein-Protected Porous Bimetallic AgPt Nanoparticles with PH-Switchable Peroxidase/Catalase-Mimicking Activity. *ACS Mater Lett* **2019**, *1* (3), 310–319. https://doi.org/10.1021/acsmaterialslett.9b00164.

(181) Shah, K.; Bhagat, S.; Varade, D.; Singh, S. Novel Synthesis of Polyoxyethylene Cholesteryl Ether Coated Fe-Pt Nanoalloys: A Multifunctional and Cytocompatible Bimetallic Alloy Exhibiting Intrinsic Chemical Catalysis and Biological Enzyme-like Activities. *Colloids Surf A Physicochem Eng Asp* **2018**, *553*, 50–57. https://doi.org/10.1016/j.colsurfa.2018.05.034.

(182) Wei, D.; Zhang, X.; Chen, B.; Zeng, K. Using Bimetallic Au@Pt Nanozymes as a Visual Tag and as an Enzyme Mimic in Enhanced Sensitive Lateral-Flow Immunoassays: Application for the Detection of Streptomycin. *Anal Chim Acta* **2020**, *1126*, 106–113. https://doi.org/10.1016/j.aca.2020.06.009.

(183) Wei, J.; Chen, X.; Shi, S.; Mo, S.; Zheng, N. An Investigation of the Mimetic Enzyme Activity of Two-Dimensional Pd-Based Nanostructures. *Nanoscale* **2015**, *7* (45), 19018–19026. https://doi.org/10.1039/c5nr05675f.

(184) Hu, B.; Xiao, X.; Chen, P.; Qian, J.; Yuan, G.; Ye, Y.; Zeng, L.; Zhong, S.; Wang, X.; Qin, X.; Yang, Y.; Pan, Y.; Zhang, Y. Enhancing Anti-Tumor Effect of Ultrasensitive Bimetallic RuCu Nanoparticles as Radio-sensitizers with Dual Enzyme-like Activities. *Biomaterials* **2022**, *290*, 121811. https://doi.org/10.1016/j.biomaterials.2022.121811.

(185) Xu, X.; Luo, P.; Yang, H.; Pan, S.; Liu, H.; Hu, X. Regulating the Enzymatic Activities of Metal-ATP Nanoparticles by Metal Doping and Their Application for H2O2 Detection. *Sens Actuators B Chem* **2021**, *335*, 129671. https://doi.org/10.1016/j.snb.2021.129671.

(186) Hu, S.; Shuai, Q.; Lin, Y.; Fu, Y.; Li, M. Chiral Fe XCu YSe Nanoparticles as Peroxidase Mimics for Colorimetric Detection of 3, 4-Dihydroxy-Phenylalanine Enantiomers. *Nanotechnology* **2022**, *33*, 135503. https://doi.org/10.1088/1361-6528/ac4306.

(187) Nie, F.; Ga, L.; Ai, J.; Wang, Y. Trimetallic PdCuAu Nanoparticles for Temperature Sensing and Fluorescence Detection of H2O2 and Glucose. *Front Chem* **2020**, *8*, 244. https://doi.org/10.3389/fchem.2020.00244.

(188) Sheng, R.; Liu, Y.; Cai, T.; Wang, R.; Yang, G.; Wen, T.; Ning, F.; Peng, H. Ultrafine FeCuAgCeGd–Based High–Entropy Nanozyme: Preparation, Catalytic Mechanism, and Point–of–Care Detection of Dopamine in Human Serum. *Chemical Engineering Journal* **2024**, *485*, 149913. https://doi.org/10.1016/j.cej.2024.149913.

(189) Feng, J.; Yang, X.; Du, T.; Zhang, L.; Zhang, P.; Zhuo, J.; Luo, L.; Sun, H.; Han, Y.; Liu, L.; Shen, Y.; Wang, J.; Zhang, W. Transition Metal High-Entropy Nanozyme: Multi-Site Orbital Coupling Modulated High-Efficiency Peroxidase Mimics. *Advanced Science* **2023**, *10*, 2303078. https://doi.org/10.1002/advs.202303078.

(190) Ai, Y.; He, M. Q.; Sun, H.; Jia, X.; Wu, L.; Zhang, X.; Sun, H. bin; Liang, Q. Ultra-Small High-Entropy Alloy Nanoparticles: Efficient Nanozyme for Enhancing Tumor Photothermal Therapy. *Advanced Materials* **2023**, *35*, 2302335. https://doi.org/10.1002/adma.202302335.

(191) Yu, F.; Huang, Y.; Cole, A. J.; Yang, V. C. The Artificial Peroxidase Activity of Magnetic Iron Oxide Nanoparticles and Its Application to Glucose Detection. *Biomaterials* **2009**, *30* (27), 4716–4722. https://doi.org/10.1016/j.biomaterials.2009.05.005.

(192) Cai, R.; Yang, D.; Yan, L.; Tian, F.; Zhang, J.; Lyu, Y.; Chen, K.; Hong, C.; Chen, X.; Zhao, Y.; Chen, Z.; Tan, W. Free-Floating 2D Nanosheets with a Superlattice Assembled from Fe3O4 Nanoparticles for Peroxidase-Mimicking Activity. *ACS Appl Nano Mater* **2018**, *1* (10), 5389–5395. https://doi.org/10.1021/acsanm.8b01380.

(193) Jiang, B.; Duan, D.; Gao, L.; Zhou, M.; Fan, K.; Tang, Y.; Xi, J.; Bi, Y.; Tong, Z.; Gao, G. F.; Xie, N.; Tang, A.; Nie, G.; Liang, M.; Yan, X. Standardized Assays for Determining the Catalytic Activity and Kinetics of Peroxidase-like Nanozymes. *Nat Protoc* **2018**, *13* (7), 1506–1520. https://doi.org/10.1038/s41596-018-0001-1.

(194) Kong, J.; Zheng, J.; Li, Z.; Huang, J.; Cao, F.; Zeng, Q.; Li, F. One-Pot Synthesis of AuAgPd Trimetallic Nanoparticles with Peroxidase-like Activity for Colorimetric Assays. *Anal Bioanal Chem* **2021**, *413*, 5383–5393. https://doi.org/10.1007/s00216-021-03514-1/Published.

(195) Ramankutty, C. G.; Sugunan, S. *Surface Properties and Catalytic Activity of Ferrospinels of Nickel, Cobalt and Copper, Prepared by Soft Chemical Methods*; 2001; Vol. 218.

(196) Zhong, Y.; Liang, X.; Tan, W.; Zhong, Y.; He, H.; Zhu, J.; Yuan, P.; Jiang, Z. A Comparative Study about the Effects of Isomorphous Substitution of Transition Metals (Ti, Cr, Mn, Co and Ni) on the UV/Fenton Catalytic Activity of Magnetite. *J Mol Catal A Chem* **2013**, *372*, 29–34. https://doi.org/10.1016/j.molcata.2013.01.038.

(197) Mei, S.; Liu, B.; Xiong, X.; Hun, X. One-Step Fabrication of Trimetallic Alloy Nanozyme Catalyzer for Luminol-H2O2 Chemiluminescence and Its Application for MiRNA-21 Detection Coupled with MiRNA Walking Machine. *J Pharm Biomed Anal* **2020**, *186*. https://doi.org/10.1016/j.jpba.2020.113280.

(198) Goyal, A.; Bansal, S.; Singhal, S. Facile Reduction of Nitrophenols: Comparative Catalytic Efficiency of MFe2O4 (M = Ni, Cu, Zn) Nano Ferrites. *Int J Hydrogen Energy* **2014**, *39* (10), 4895–4908. https://doi.org/10.1016/j.ijhydene.2014.01.050.

(199) Liang, X.; He, Z.; Wei, G.; Liu, P.; Zhong, Y.; Tan, W.; Du, P.; Zhu, J.; He, H.; Zhang, J. The Distinct Effects of Mn Substitution on the Reactivity of Magnetite in Heterogeneous Fenton Reaction and Pb(II) Adsorption. *J Colloid Interface Sci* **2014**, *426*, 181–189. https://doi.org/10.1016/j.jcis.2014.03.065.

(200) Wu, J.; Qin, K.; Yuan, D.; Tan, J.; Qin, L.; Zhang, X.; Wei, H. Rational Design of Au@Pt Multibranched Nanostructures as Bifunctional Nanozymes. *ACS Appl Mater Interfaces* **2018**, *10* (15), 12954–12959. https://doi.org/10.1021/acsami.7b17945.

(201) Tseng, C. W.; Chang, H. Y.; Chang, J. Y.; Huang, C. C. Detection of Mercury Ions Based on Mercury-Induced Switching of Enzyme-like Activity of Platinum/Gold Nanoparticles. *Nanoscale* **2012**, *4* (21), 6823–6830. https://doi.org/10.1039/c2nr31716h.

(202) Liu, C.; Yan, Y.; Zhang, X.; Mao, Y.; Ren, X.; Hu, C.; He, W.; Yin, J. J. Regulating the Pro- and Anti-Oxidant Capabilities of Bimetallic Nanozymes for the Detection of Fe2+ and Protection of: Monascus Pigments. *Nanoscale* **2020**, *12* (5), 3068–3075. https://doi.org/10.1039/c9nr10135g.

(203) Polarz, S.; Strunk, J.; Ischenko, V.; Van Den Berg, M. W. E.; Hinrichsen, O.; Muhler, M.; Driess, M. On the Role of Oxygen Defects in the Catalytic Performance of Zinc Oxide. *Angewandte Chemie - International Edition* **2006**, *45* (18), 2965–2969. https://doi.org/10.1002/anie.200503068.

(204) Xu, L.; Jiang, Q.; Xiao, Z.; Li, X.; Huo, J.; Wang, S.; Dai, L. Plasma-Engraved Co 3 O 4 Nanosheets with Oxygen Vacancies and High Surface Area for the Oxygen Evolution Reaction . *Angewandte Chemie* **2016**, *128* (17), 5363–5367. https://doi.org/10.1002/ange.201600687.

(205) Lee, H.; Kim, J. Y.; Lee, S. Y.; Hong, J. A.; Kim, N.; Baik, J.; Hwang, Y. J. Comparative Study of Catalytic Activities among Transition Metal-Doped IrO2 Nanoparticles. *Sci Rep* **2018**, *8* (1). https://doi.org/10.1038/s41598-018-35116-w.

(206) Feng, D.; Dong, Y.; Zhang, L.; Ge, X.; Zhang, W.; Dai, S.; Qiao, Z. A. Holey Lamellar High-Entropy Oxide as an Ultra-High-Activity Heterogeneous Catalyst for Solvent-Free Aerobic Oxidation of Benzyl Alcohol. *Angewandte Chemie - International Edition* **2020**, *59* (44), 19503–19509. https://doi.org/10.1002/anie.202004892.

(207) Shu, Y.; Bao, J.; Yang, S.; Duan, X.; Zhang, P. Entropy-Stabilized Metal-CeOx Solid Solutions for Catalytic Combustion of Volatile Organic Compounds. *AIChE Journal* **2020**, *67* (1).

(208) Wang, B.; Yao, Y.; Yu, X.; Wang, C.; Wu, C.; Zou, Z. Understanding the Enhanced Catalytic Activity of High Entropy Alloys: From Theory to Experiment. *J Mater Chem A Mater* **2021**, *9* (35), 19410–19438. https://doi.org/10.1039/d1ta02718b.

(209) Xin, Y.; Li, S.; Qian, Y.; Zhu, W.; Yuan, H.; Jiang, P.; Guo, R.; Wang, L. High-Entropy Alloys as a Platform for Catalysis: Progress, Challenges, and Opportunities. *ACS Catal* **2020**, *10* (19), 11280–11306. https://doi.org/10.1021/acscatal.0c03617.

(210) Shao, Q.; Wang, P.; Huang, X. Opportunities and Challenges of Interface Engineering in Bimetallic Nanostructure for Enhanced Electrocatalysis. *Advanced Functional Materials*. Wiley-VCH Verlag January 17, 2019. https://doi.org/10.1002/adfm.201806419.

(211) Yang, Y.; Luo, M.; Zhang, W.; Sun, Y.; Chen, X.; Guo, S. Metal Surface and Interface Energy Electrocatalysis: Fundamentals, Performance Engineering, and Opportunities. *Chem*. Elsevier Inc September 13, 2018, pp 2054–2083. https://doi.org/10.1016/j.chempr.2018.05.019.

(212) Luo, M.; Guo, S. Strain-Controlled Electrocatalysis on Multimetallic Nanomaterials. *Nature Reviews Materials*. Nature Publishing Group September 26, 2017. https://doi.org/10.1038/natrevmats.2017.59.

(213) Xia, Z.; Guo, S. Strain Engineering of Metal-Based Nanomaterials for Energy Electrocatalysis. *Chemical Society Reviews*. Royal Society of Chemistry June 21, 2019, pp 3265–3278. https://doi.org/10.1039/c8cs00846a.

(214) Liu; Zhang, A.; Wang, R.; Zhang, Q.; Cui, D. A Review on Metal- and Metal Oxide-Based Nanozymes: Properties, Mechanisms, and Applications. *Nano-Micro Letters*. Springer Science and Business Media B.V. December 1, 2021. https://doi.org/10.1007/s40820-021-00674-8.

(215) Yang, W.; Yang, X.; Zhu, L.; Chu, H.; Li, X.; Xu, W. Nanozymes: Activity Origin, Catalytic Mechanism, and Biological Application. *Coord Chem Rev* **2021**, *448*, 214170. https://doi.org/10.1016/j.ccr.2021.214170.

(216) Alizadeh, N.; Salimi, A. Multienzymes Activity of Metals and Metal Oxide Nanomaterials: Applications from Biotechnology to Medicine and Environmental Engineering. *Journal of Nanobiotechnology*. BioMed Central Ltd December 1, 2021. https://doi.org/10.1186/s12951-021-00771-1.

(217) Tian, R.; Ma, H.; Ye, W.; Li, Y.; Wang, S.; Zhang, Z.; Liu, S.; Zang, M.; Hou, J.; Xu, J.; Luo, Q.; Sun, H.; Bai, F.; Yang, Y.; Liu, J. Se-Containing MOF Coated Dual-Fe-Atom Nanozymes With Multi-Enzyme Cascade Activities Protect Against Cerebral Ischemic Reperfusion Injury. *Adv Funct Mater* **2022**, *32* (36). https://doi.org/10.1002/adfm.202204025.

(218) Li, L.; Hu, Y.; Shi, Y.; Liu, Y.; Liu, T.; Zhou, H.; Niu, W.; Zhang, L.; Zhang, J.; Xu, G. Triple-Enzyme-Mimicking AuPt3Cu Hetero-Structural Alloy Nanozymes towards Cascade Reactions in Chemodynamic Therapy. *Chemical Engineering Journal* **2023**, *463*, 142494. https://doi.org/10.1016/j.cej.2023.142494.

(219) Mu, X.; Wang, J.; Li, Y.; Xu, F.; Long, W.; Ouyang, L.; Liu, H.; Jing, Y.; Wang, J.; Dai, H.; Liu, Q.; Sun, Y.; Liu, C.; Zhang, X. D. Redox Trimetallic Nanozyme with Neutral Environment Preference for Brain Injury. *ACS Nano* **2019**, *13*, 1870–1884. https://doi.org/10.1021/acsnano.8b08045.

(220) Liang, Y.; Liao, C.; Guo, X.; Li, G.; Yang, X.; Yu, J.; Zhong, J.; Xie, Y.; Zheng, L.; Zhao, J. RhRu Alloy-Anchored MXene Nanozyme for Synergistic Osteosarcoma Therapy. *Small* **2023**, *19*, 2205511. https://doi.org/10.1002/smll.202205511.

(221) He, X.; Tan, L.; Chen, D.; Wu, X.; Ren, X.; Zhang, Y.; He, X.; Tang, F. Fe3O4-Au@mesoporous SiO2 Microspheres: An Ideal Artificial Enzymatic Cascade System. *Chemical Communications* **2013**, *49* (41), 4643–4645. https://doi.org/10.1039/c3cc40622a.

(222) Soh, M.; Kang, D.; Jeong, H.; Kim, D.; Kim, D. Y.; Yang, W.; Song, C.; Baik, S.; Choi, I.; Ki, S.; Kwon, H. J.; Kim, T.; Kim, C. K.; Lee, S.; Hyeon, T. Ceria–Zirconia Nanoparticles as an Enhanced Multi-Antioxidant for Sepsis Treatment. *Angewandte Chemie* **2017**, *129* (38), 11557–11561. https://doi.org/10.1002/ange.201704904.

(223) Ma, X.; Jin, H.; Ren, Y.; Shen, Z.; Wang, L.; Zhang, S.; Lu, Y.; Guan, S.; Zhou, S.; Qu, X. A Tripartite-Enzyme via Curcumin Regarded as Zymoexciter towards Highly Efficient Relieving Reperfusion Injury. *Chemical Engineering Journal* **2022**, *442*. https://doi.org/10.1016/j.cej.2022.136029.

(224) Xu, R.; Tan, X.; Li, T.; Liu, S.; Li, Y.; Li, H. Norepinephrine-Induced AuPd Aerogels with Peroxidase- and Glucose Oxidase-like Activity for Colorimetric Determination of Glucose. *Microchimica Acta* **2021**, *188* (11). https://doi.org/10.1007/s00604-021-05014-6.

(225) Fu, S.; Yang, R.; Zhang, L.; Liu, W.; Du, G.; Cao, Y.; Xu, Z.; Cui, H.; Kang, Y.; Xue, P. Biomimetic CoO@AuPt Nanozyme Responsive to Multiple Tumor Microenvironmental Clues for Augmenting Chemodynamic Therapy. *Biomaterials* **2020**, *257*, 120279. https://doi.org/10.1016/j.biomaterials.2020.120279.

(226) He, W.; Liu, Y.; Yuan, J.; Yin, J. J.; Wu, X.; Hu, X.; Zhang, K.; Liu, J.; Chen, C.; Ji, Y.; Guo, Y. Au@Pt Nanostructures as Oxidase and Peroxidase Mimetics for Use in Immunoassays. *Biomaterials* **2011**, *32* (4), 1139–1147. https://doi.org/10.1016/j.biomaterials.2010.09.040.

(227) Sun, M.; He, M.; Jiang, S.; Wang, Y.; Wang, X.; Liu, T.; Song, C.; Wang, S.; Rao, H.; Lu, Z. Multi-Enzyme Activity of Three Layers FeOx@ZnMnFeOy@Fe-Mn Organogel for Colorimetric Detection of Antioxidants and Norfloxacin with Smartphone. *Chemical Engineering Journal* **2021**, *425*. https://doi.org/10.1016/j.cej.2021.131823.

(228) Tran, V. K.; Gupta, P. K.; Park, Y.; Son, S. E.; Hur, W.; Lee, H. B.; Park, J. Y.; Kim, S. N.; Seong, G. H. Functionalized Bimetallic IrPt Alloy Nanoparticles: Multi-Enzyme Mimics for Colorimetric and Fluorometric Detection of Hydrogen Peroxide and Glucose. *J Taiwan Inst Chem Eng* **2021**, *120*, 336–343. https://doi.org/10.1016/j.jtice.2021.03.029.

(229) Wang, Q.; Zhang, L.; Shang, C.; Zhang, Z.; Dong, S. Triple-Enzyme Mimetic Activity of Nickel-Palladium Hollow Nanoparticles and Their Application in Colorimetric Biosensing of Glucose. *Chemical Communications* **2016**, *52* (31), 5410–5413. https://doi.org/10.1039/c6cc00194g.

(230) Tang, W.; An, Y.; Chen, J.; Row, K. H. Multienzyme Mimetic Activities of Holey CuPd@H–C3N4 for Visual Colorimetric and Ultrasensitive Fluorometric Discriminative Detection of Glutathione and Glucose in Physiological Fluids. *Talanta* **2022**, *241*. https://doi.org/10.1016/j.talanta.2022.123221.

(231) Wang, X.; Xu, Y.; Cheng, N.; Zhang, Q.; Yang, Z.; Liu, B.; Wang, X.; Huang, K.; Luo, Y. Pd@Pt Nanoparticles: Trienzyme Catalytic Mechanisms, Surface-Interface Effect with DNA and Application in Biosensing. *Sens Actuators B Chem* **2022**, *364*. https://doi.org/10.1016/j.snb.2022.131907.

(232) Liu, Y.; Qing, Y.; Jing, L.; Zou, W.; Guo, R. Platinum-Copper Bimetallic Colloid Nanoparticle Cluster Nanozymes with Multiple Enzyme-like Activities for Scavenging Reactive Oxygen Species. *Langmuir* **2021**, *37* (24), 7364–7372. https://doi.org/10.1021/acs.langmuir.1c00697.

(233) Jain, S.; Sharma, B.; Thakur, N.; Mishra, S.; Sarma, T. K. Copper Pyrovanadate Nanoribbons as Efficient Multienzyme Mimicking Nanozyme for Biosensing Applications. *ACS Appl Nano Mater* **2020**, *3* (8), 7917–7929. https://doi.org/10.1021/acsanm.0c01415.

(234) Guo, X.; Yang, F.; Jing, L.; Li, J.; Li, Y.; Ding, R.; Duan, B.; Zhang, X. In-Situ Generation of Highly Active and Four-in-One CoFe2O4/H2PPOP Nanozyme: Mechanism and Its Application for Fast Colorimetric Detection of Cr (VI). *J Hazard Mater* **2022**, *431*. https://doi.org/10.1016/j.jhazmat.2022.128621.

(235) Yang, H.; He, Q.; Pan, J.; Lin, M.; Lao, Z.; Li, Q.; Cui, X.; Zhao, S. PtCu Nanocages with Superior Tetra-Enzyme Mimics for Colorimetric Sensing and Fluorescent Sensing Dehydroepiandrosterone. *Sens Actuators B Chem* **2022**, *351*. https://doi.org/10.1016/j.snb.2021.130905.

(236) Liu, J.; Zhang, W.; Peng, M.; Ren, G.; Guan, L.; Li, K.; Lin, Y. ZIF-67 as a Template Generating and Tuning "Raisin Pudding"-Type Nanozymes with Multiple Enzyme-like Activities: Toward Online Electrochemical Detection of 3,4-Dihydroxyphenylacetic Acid in Living Brains. *ACS Appl Mater Interfaces* **2020**, *12* (26), 29631–29640. https://doi.org/10.1021/acsami.0c05667.

(237) George, E. P.; Raabe, D.; Ritchie, R. O. High-Entropy Alloys. *Nature Reviews Materials*. Nature Publishing Group August 1, 2019, pp 515–534. https://doi.org/10.1038/s41578-019-0121-4.

(238) Sun; Dai, S. High-Entropy Materials for Catalysis: A New Frontier. *Sci. Adv* **2021**, *7*, eabg1600.

(239) Xie, P.; Yao, Y.; Huang, Z.; Liu, Z.; Zhang, J.; Li, T.; Wang, G.; Shahbazian-Yassar, R.; Hu, L.; Wang, C. Highly Efficient Decomposition of Ammonia Using High-Entropy Alloy Catalysts. *Nat Commun* **2019**, *10*, 4011. https://doi.org/10.1038/s41467-019-11848-9.

(240) Yeh, J. W. Alloy Design Strategies and Future Trends in High-Entropy Alloys. *JOM* **2013**, *65* (12), 1759–1771. https://doi.org/10.1007/s11837-013-0761-6.

(241) Khorshidi, A.; Violet, J.; Hashemi, J.; Peterson, A. A. How Strain Can Break the Scaling Relations of Catalysis. *Nat Catal* **2018**, *1* (4), 263–268. https://doi.org/10.1038/s41929-018-0054-0.

(242) Schweidler, S.; Botros, M.; Strauss, F.; Wang, Q.; Ma, Y.; Velasco, L.; Cadilha Marques, G.; Sarkar, A.; Kübel, C.; Hahn, H.; Aghassi-Hagmann, J.; Brezesinski, T.; Breitung, B. High-Entropy Materials for Energy and Electronic Applications. *Nat Rev Mater* **2024**. https://doi.org/10.1038/s41578-024-00654-5.

(243) Gao, Y.; Liu, Y.; Yu, H.; Zou, D. High-Entropy Oxides for Catalysis: Status and Perspectives. *Applied Catalysis A: General*. Elsevier B.V. February 5, 2022. https://doi.org/10.1016/j.apcata.2022.118478.

(244) Tsai, K.-Y.; Tsai, M.-H.; Yeh, J.-W. Sluggish Diffusion in Co-Cr-Fe-Mn-Ni High-Entropy Alloys. *Acta Mater* **2013**, *61* (13), 4887–4897. https://doi.org/10.1016/j.actamat.2013.04.058.

(245) Yao, Y.; Liu, Z.; Xie, P.; Huang, Z.; Li, T.; Morris, D.; Finfrock, Z.; Zhou, J.; Jiao, M.; Gao, J.; Mao, Y.; Miao, J.; Zhang, P.; Shahbazian-Yassar, R.; Wang, C.; Wang, G.; Hu, L. *Computationally Aided, Entropy-Driven Synthesis of Highly Efficient and Durable Multi-Elemental Alloy Catalysts*; 2020; Vol. 6. http://advances.sciencemag.org/.

(246) Ye, Y. F.; Wang, Q.; Lu, J.; Liu, C. T.; Yang, Y. High-Entropy Alloy: Challenges and Prospects. *Materials Today*. Elsevier B.V. July 1, 2016, pp 349–362. https://doi.org/10.1016/j.mattod.2015.11.026.

(247) Miracle, D. B.; Senkov, O. N. A Critical Review of High Entropy Alloys and Related Concepts. *Acta Materialia*. Elsevier Ltd January 1, 2017, pp 448–511. https://doi.org/10.1016/j.actamat.2016.08.081.

(248) Ranganathan, S. *Alloyed Pleasures: Multimetallic Cocktails*; 2003; Vol. 85.

(249) Edalati, P.; Wang, Q.; Razavi-Khosroshahi, H.; Fuji, M.; Ishihara, T.; Edalati, K. Photocatalytic Hydrogen Evolution on a High-Entropy Oxide. *J Mater Chem A Mater* **2020**, *8* (7), 3814–3821. https://doi.org/10.1039/c9ta12846h.

(250) Ye, H.; Yang, K.; Tao, J.; Liu, Y.; Zhang, Q.; Habibi, S.; Nie, Z.; Xia, X. An Enzyme-Free Signal Amplification Technique for Ultrasensitive Colorimetric Assay of Disease Biomarkers. *ACS Nano* **2017**, *11* (2), 2052–2059. https://doi.org/10.1021/acsnano.6b08232.

(251) Masud, M. K.; Yadav, S.; Islam, M. N.; Nguyen, N. T.; Salomon, C.; Kline, R.; Alamri, H. R.; Alothman, Z. A.; Yamauchi, Y.; Hossain, M. S. A.; Shiddiky, M. J. A. Gold-Loaded Nanoporous Ferric Oxide Nanocubes with Peroxidase-Mimicking Activity for Electrocatalytic and Colorimetric Detection of Autoantibody. *Anal Chem* **2017**, *89* (20), 11005–11013. https://doi.org/10.1021/acs.analchem.7b02880.

(252) Lv, F.; Gong, Y.; Cao, Y.; Deng, Y.; Liang, S.; Tian, X.; Gu, H.; Yin, J. J. A Convenient Detection System Consisting of Efficient Au@PtRu Nanozymes and Alcohol Oxidase for Highly Sensitive Alcohol Biosensing. *Nanoscale Adv* **2020**, *2* (4), 1583–1589. https://doi.org/10.1039/d0na00002g.

(253) Su, L.; Feng, J.; Zhou, X.; Ren, C.; Li, H.; Chen, X. Colorimetric Detection of Urine Glucose Based ZnFe2O4 Magnetic Nanoparticles. *Anal Chem* **2012**, *84* (13), 5753–5758. https://doi.org/10.1021/ac300939z.

(254) Shen, J.; Rees, T. W.; Zhou, Z.; Yang, S.; Ji, L.; Chao, H. A Mitochondria-Targeting Magnetothermogenic Nanozyme for Magnet-Induced Synergistic Cancer Therapy. *Biomaterials* **2020**, *251*. https://doi.org/10.1016/j.biomaterials.2020.120079.

(255) Wang, D.; Zhang, L.; Wang, C.; Cheng, Z.; Zheng, W.; Xu, P.; Chen, Q.; Zhao, Y. Missing-Linker-Confined Single-Atomic Pt Nanozymes for Enzymatic Theranostics of Tumor. *Angewandte Chemie - International Edition* **2023**, *62* (19). https://doi.org/10.1002/anie.202217995.

(256) Wang, H.; Wan, K.; Shi, X. Recent Advances in Nanozyme Research. *Advanced Materials* **2019**, *31* (45). https://doi.org/10.1002/adma.201805368.

(257) Wei, H.; Wang, E. Nanomaterials with Enzyme-like Characteristics (Nanozymes): Next-Generation Artificial Enzymes. *Chem Soc Rev* **2013**, *42* (14), 6060–6093. https://doi.org/10.1039/c3cs35486e.

(258) Costa, R. C. C.; Lelis, M. F. F.; Oliveira, L. C. A.; Fabris, J. D.; Ardisson, J. D.; Rios, R. R. V. A.; Silva, C. N.; Lago, R. M. Novel Active Heterogeneous Fenton System Based on Fe3-XM XO4 (Fe, Co, Mn, Ni): The Role of M2+ Species on the Reactivity towards H2O2 Reactions. *J Hazard Mater* **2006**, *129* (1–3), 171–178. https://doi.org/10.1016/j.jhazmat.2005.08.028.

(259) Liang, X.; Zhong, Y.; He, H.; Yuan, P.; Zhu, J.; Zhu, S.; Jiang, Z. The Application of Chromium Substituted Magnetite as Heterogeneous Fenton Catalyst for the Degradation of Aqueous Cationic and Anionic Dyes. *Chemical Engineering Journal* **2012**, *191*, 177–184. https://doi.org/10.1016/j.cej.2012.03.001.

(260) Zhong, Y.; Liang, X.; Zhong, Y.; Zhu, J.; Zhu, S.; Yuan, P.; He, H.; Zhang, J. Heterogeneous UV/Fenton Degradation of TBBPA Catalyzed by Titanomagnetite: Catalyst Characterization, Performance and Degradation Products. *Water Res* **2012**, *46* (15), 4633–4644. https://doi.org/10.1016/j.watres.2012.06.025.

(261) He, W.; Cai, J.; Zhang, H.; Zhang, L.; Zhang, X.; Li, J.; Yin, J. J. Formation of PtCuCo Trimetallic Nanostructures with Enhanced Catalytic and Enzyme-like Activities for Biodetection. *ACS Appl Nano Mater* **2018**, *1* (1), 222–231. https://doi.org/10.1021/acsanm.7b00109.

(262) Ni, C.; O'Connor, K. M.; Trach, J.; Butler, C.; Rieger, B.; Veinot, J. G. C. Facile Synthesis of High-Entropy Alloy Nanoparticles on Germanane, Ge Nanoparticles and Wafers. *Nanoscale Horiz* **2023**, *8* (9), 1217–1225. https://doi.org/10.1039/d3nh00178d.

(263) Liu, Y.-H.; Hsieh, C.-J.; Hsu, L.-C.; Lin, K.-H.; Hsiao, Y.-C.; Chi, C.-C.; Lin, J.-T.; Chang, C.-W.; Lin, S.-C.; Wu, C.-Y.; Gao, J.-Q.; Pao, C.-W.; Chang, Y.-M.; Lu, M.-Y.; Zhou, S.; Yang, T.-H. *Toward Controllable and Predictable Synthesis of High-Entropy Alloy Nanocrystals*; 2023. https://www.science.org.

(264) Chen, H.; Fu, J.; Zhang, P.; Peng, H.; Abney, C. W.; Jie, K.; Liu, X.; Chi, M.; Dai, S. Entropy-Stabilized Metal Oxide Solid Solutions as CO Oxidation Catalysts with High-Temperature Stability. *J Mater Chem A Mater* **2018**, *6* (24), 11129–11133. https://doi.org/10.1039/c8ta01772g.

(265) Lv, Z. Y.; Liu, X. J.; Jia, B.; Wang, H.; Wu, Y.; Lu, Z. P. Development of a Novel High-Entropy Alloy with Eminent Efficiency of Degrading Azo Dye Solutions. *Sci Rep* **2016**, *6*, 34213. https://doi.org/10.1038/srep34213.

(266) Xie, M.; Fang, W.; Qu, Z.; Hu, Y.; Zhang, Y.; Chao, J.; Shi, J.; Wang, L.; Wang, L.; Tian, Y.; Fan, C.; Liu, H. High-Entropy Alloy Nanopatterns by Prescribed Metallization of DNA Origami Templates. *Nat Commun* **2023**, *14*, 1745. https://doi.org/10.1038/s41467-023-37333-y.

(267) Phan-Xuan, T.; Schweidler, S.; Hirte, S.; Schüller, M.; Lin, L.; Khandelwal, A.; Wang, K.; Schützke, J.; Reischl, M.; Kübel, C.; Hahn, H.; Bello, G.; Kirchmair, J.; Aghassi-Hagmann, J.; Brezesinski, T.; Breitung, B.; Dailey, L. A. Using the High-Entropy Approach to Obtain Multimetal Oxide Nanozymes: Library Synthesis, In Silico Structure-Activity, and Immunoassay Performance. *ACS Nano* **2024**. https://doi.org/10.1021/acsnano.4c03053.

(268) Shannon, R. D. Revised Effective Ionic Radii and Systematic Studies of Interatomie Distances in Halides and Chaleogenides. *Acta Cryst* **1976**, *32*, 751.

(269) Ramankutty, C. G.; Sugunan, S.; Thomas, B. Study of Cyclohexanol Decomposition Reaction over the Ferrospinels, A1−xCuxFe2O4 (A=Ni or Co and X=0, 0.3, 0.5, 0.7 and 1), Prepared by 'Soft' Chemical Methods. *J Mol Catal A Chem* **2002**, *187* (1), 105–117. https://doi.org/10.1016/S1381-1169(02)00121-8.

(270) Yuan, B.; Chou, H. L.; Peng, Y. K. Disclosing the Origin of Transition Metal Oxides as Peroxidase (and Catalase) Mimetics. *ACS Applied Materials and Interfaces*. American Chemical Society May 25, 2022, pp 22728–22736. https://doi.org/10.1021/acsami.1c13429.

(271) Li, M.; Liu, J.; Xu, Y.; Qian, G. Phosphate Adsorption on Metal Oxides and Metal Hydroxides: A Comparative Review. *Environmental Reviews* **2016**, *24* (3), 319–332. https://doi.org/10.1139/er-2015-0080.

(272) Muthukumaran, T.; Philip, J. Effect of Phosphate and Oleic Acid Capping on Structure, Magnetic Properties and Thermal Stability of Iron Oxide Nanoparticles. *J Alloys Compd* **2016**, *689*, 959–968. https://doi.org/10.1016/j.jallcom.2016.08.067.

(273) Ng, Y. H.; Chin, S. F.; Pang, S. C.; Ng, S. M. Utilising the Interface Interaction on Tris(Hydroxymethy)Aminomethane-Capped Carbon Dots to Enhance the Sensitivity and Selectivity towards the Detection of Co(II) Ions. *Sens Actuators B Chem* **2018**, *273*, 83–92. https://doi.org/10.1016/j.snb.2018.05.178.

(274) Raineri, M.; Winkler, E. L.; Torres, T. E.; Vasquez Mansilla, M.; Nadal, M. S.; Zysler, R. D.; Lima, E. Effects of Biological Buffer Solutions on the Peroxidase-like Catalytic Activity of Fe3O4 Nanoparticles. *Nanoscale* **2019**, *11* (39), 18393–18406. https://doi.org/10.1039/c9nr05799d.

(275) Sahoo, Y.; Pizem, H.; Fried, T.; Golodnitsky, D.; Burstein, L.; Sukenik, C. N.; Markovich, G. Alkyl Phosphonate/Phosphate Coating on Magnetite Nanoparticles: A Comparison with Fatty Acids. *Langmuir* **2001**, *17*, 7907–7911. https://doi.org/10.1021/la010703.

(276) Ferreira, C. M. H.; Pinto, I. S. S.; Soares, E. V.; Soares, H. M. V. M. (Un)Suitability of the Use of PH Buffers in Biological, Biochemical and Environmental Studies and Their Interaction with Metal Ions-a Review. *RSC Advances*. Royal Society of Chemistry 2015, pp 30989–31003. https://doi.org/10.1039/c4ra15453c.

(277) Dong, H.; Du, W.; Dong, J.; Che, R.; Kong, F.; Cheng, W.; Ma, M.; Gu, N.; Zhang, Y. Depletable Peroxidase-like Activity of Fe3O4 Nanozymes Accompanied with Separate Migration of Electrons and Iron Ions. *Nat Commun* **2022**, *13* (1). https://doi.org/10.1038/s41467-022-33098-y.

(278) Zhang, R.; Wang, C.; Zou, P.; Lin, R.; Ma, L.; Yin, L.; Li, T.; Xu, W.; Jia, H.; Li, Q.; Sainio, S.; Kisslinger, K.; Trask, S. E.; Ehrlich, S. N.; Yang, Y.; Kiss, A. M.; Ge, M.; Polzin, B. J.; Lee, S. J.; Xu, W.; Ren, Y.; Xin, H. L. Compositionally Complex Doping for Zero-Strain Zero-Cobalt Layered Cathodes. *Nature* **2022**, *610* (7930), 67–73. https://doi.org/10.1038/s41586-022-05115-z.

(279) Fang, Y.; Chen, N.; Du, G.; Zhang, M.; Zhao, X.; Cheng, H.; Wu, J. High-Temperature Oxidation Resistance, Mechanical and Wear Resistance Properties of Ti(C,N)-Based Cermets with Al0.3CoCrFeNi High-Entropy Alloy as a Metal Binder. *J Alloys Compd* **2020**, *815*. https://doi.org/10.1016/j.jallcom.2019.152486.

(280) Su, L.; Qin, W.; Zhang, H.; Rahman, Z. U.; Ren, C.; Ma, S.; Chen, X. The Peroxidase/Catalase-like Activities of MFe2O4 (M=Mg, Ni, Cu) MNPs and Their Application in Colorimetric Biosensing of Glucose. *Biosens Bioelectron* **2015**, *63*, 384–391. https://doi.org/10.1016/j.bios.2014.07.048.

(281) Wu, L.; Wan, G.; Hu, N.; He, Z.; Shi, S.; Suo, Y.; Wang, K.; Xu, X.; Tang, Y.; Wang, G. Synthesis of Porous CoFe2O4 and Its Application as a Peroxidase Mimetic for Colorimetric Detection of H2O2 and Organic Pollutant Degradation. *Nanomaterials* **2018**, *8*, 451. https://doi.org/10.3390/nano8070451.

(282) Zhang, R.; Zhao, H.; Fan, K. Structure-Activity Mechanism of Iron Oxide Nanozymes. In *Nanozymes: Design, Synthesis, and Applications*; 2022; pp 1–35. https://doi.org/10.1021/bk-2022-1422.ch001.

(283) Hang, D. R.; Pan, Y. Q.; Sharma, K. H.; Chou, M. M. C.; Islam, S. E.; Wu, H. F.; Liang, C. Te. 2d Ctab-Mose2 Nanosheets and 0d Mose2 Quantum Dots: Facile Top-down Preparations and Their Peroxidase-like Catalytic Activity for Colorimetric Detection of Hydrogen Peroxide. *Nanomaterials* **2020**, *10* (10), 1–19. https://doi.org/10.3390/nano10102045.

(284) Vehtari, A.; Gelman, A.; Gabry, J. Practical Bayesian Model Evaluation Using Leave-One-out Cross-Validation and WAIC. *Stat Comput* **2017**, *27* (5), 1413–1432. https://doi.org/10.1007/s11222-016-9696-4.

(285) Reza Hormozi Jangi, S. A Comparative Study on Kinetics Performances of BSA-Gold Nanozymes for Nanozyme-Mediated Oxidation of 3,3',5,5'-Tetramethylbenzidine and 3,3'-Diaminobenzidine. **2023**. https://doi.org/10.20944/preprints202306.0387.v1.

(286) Shuai, Y. A Tumor-Microenvironment-Activated Nanoplatform of Modified SnFe2O4 Nanozyme in Scaffold for Enhanced PTT/PDT Tumor Therapy. *Heliyon* **2023**, *9* (7). https://doi.org/10.1016/j.heliyon.2023.e18019.

(287) Li, S.; Ding, H.; Chang, J.; Dong, S.; Shao, B.; Dong, Y.; Gai, S.; He, F.; Yang, P. Bimetallic Oxide Nanozyme-Mediated Depletion of Glutathione to Boost Oxidative Stress for Combined Nanocatalytic Therapy. *J Colloid Interface Sci* **2022**, *623*, 787–798. https://doi.org/10.1016/j.jcis.2022.05.059.

(288) Yin, S. Y.; Song, G.; Yang, Y.; Zhao, Y.; Wang, P.; Zhu, L. M.; Yin, X.; Zhang, X. B. Persistent Regulation of Tumor Microenvironment via Circulating Catalysis of MnFe2O4@Metal–Organic Frameworks for Enhanced Photodynamic Therapy. *Adv Funct Mater* **2019**, *29* (25). https://doi.org/10.1002/adfm.201901417.

(289) Fang, G.; Li, W.; Shen, X.; Perez-Aguilar, J. M.; Chong, Y.; Gao, X.; Chai, Z.; Chen, C.; Ge, C.; Zhou, R. Differential Pd-Nanocrystal Facets Demonstrate Distinct Antibacterial Activity against Gram-Positive and Gram-Negative Bacteria. *Nat Commun* **2018**, *9* (1). https://doi.org/10.1038/s41467-017-02502-3.

(290) Shen, X.; Wang, Z.; Gao, X. J.; Gao, X. Reaction Mechanisms and Kinetics of Nanozymes: Insights from Theory and Computation. *Advanced Materials*. John Wiley and Sons Inc March 7, 2024. https://doi.org/10.1002/adma.202211151.

(291) Shen, X.; Wang, Z.; Gao, X.; Zhao, Y. Density Functional Theory-Based Method to Predict the Activities of Nanomaterials as Peroxidase Mimics. *ACS Catal* **2020**, *10* (21), 12657–12665. https://doi.org/10.1021/acscatal.0c03426.

(292) Gumpelmayer, M.; Nguyen, M.; Molnár, G.; Bousseksou, A.; Meunier, B.; Robert, A. Magnetite Fe 3 O 4 Has No Intrinsic Peroxidase Activity, and Is Probably Not Involved in Alzheimer's Oxidative Stress . *Angewandte Chemie* **2018**, *130* (45), 14974–14979. https://doi.org/10.1002/ange.201807676.

(293) Xi, Z.; Wei, K.; Wang, Q.; Kim, M. J.; Sun, S.; Fung, V.; Xia, X. Nickel–platinum Nanoparticles as Peroxidase Mimics with a Record High Catalytic Efficiency. *J Am Chem Soc* **2021**, *143* (7), 2660–2664. https://doi.org/10.1021/jacs.0c12605.

(294) Guo, Z.; Hong, J.; Song, N.; Liang, M. Single-Atom Nanozymes: From Precisely Engineering to Extensive Applications. *Acc Mater Res* **2023**. https://doi.org/10.1021/accountsmr.3c00250.

(295) Kim, M. S.; Lee, J.; Kim, H. S.; Cho, A.; Shim, K. H.; Le, T. N.; An, S. S. A.; Han, J. W.; Kim, M. Il; Lee, J. Heme Cofactor-Resembling Fe–N Single Site Embedded Graphene as Nanozymes to Selectively Detect H2O2 with High Sensitivity. *Adv Funct Mater* **2020**, *30* (1). https://doi.org/10.1002/adfm.201905410.

(296) Ji, S.; Jiang, B.; Hao, H.; Chen, Y.; Dong, J.; Mao, Y.; Zhang, Z.; Gao, R.; Chen, W.; Zhang, R.; Liang, Q.; Li, H.; Liu, S.; Wang, Y.; Zhang, Q.; Gu, L.; Duan, D.; Liang, M.; Wang, D.; Yan, X.; Li, Y. Matching the Kinetics of Natural Enzymes with a Single-Atom Iron Nanozyme. *Nat Catal* **2021**, *4* (5), 407–417. https://doi.org/10.1038/s41929-021-00609-x.

(297) Zhang, S.; Li, Y.; Sun, S.; Liu, L.; Mu, X.; Liu, S.; Jiao, M.; Chen, X.; Chen, K.; Ma, H.; Li, T.; Liu, X.; Wang, H.; Zhang, J.; Yang, J.; Zhang, X. D. Single-Atom Nanozymes Catalytically Surpassing Naturally Occurring Enzymes as Sustained Stitching for Brain Trauma. *Nat Commun* **2022**, *13* (1). https://doi.org/10.1038/s41467-022-32411-z.

(298) Pamela A., W.; Jose, C.; Alison, W.; Hayley C., A.; Dijana Matak, V.; Harren, J. Crystal Structure of Human P450 2C9 with bound Warfarin. *Nature* **2003**, *424* (6947), 464–468. https://doi.org/10.1038/nature01817.

(299) Wittenborn, E. C.; Cohen, S. E.; Merrouch, M.; Léger, C.; Fourmond, V.; Dementin, S.; Drennan, C. L. Structural Insight into Metallocofactor Maturation in Carbon Monoxide Dehydrogenase. *Journal of Biological Chemistry* **2019**, *294* (35), 13017–13026. https://doi.org/10.1074/jbc.RA119.009610.

(300) Einsle, O.; Rees, D. C. Structural Enzymology of Nitrogenase Enzymes. *Chemical Reviews*. American Chemical Society June 24, 2020, pp 4969–5004. https://doi.org/10.1021/acs.chemrev.0c00067.

(301) Zhao, M.; Yang, R.; Wei, Y.; Su, J.; Wang, X.; Zhang, N.; Sun, P.; Chen, D.; Zhao, Y. Dual Isolated Bimetal Single-Atom Catalysts for Tumor ROS Cycle and Parallel Catalytic Therapy. *Nano Today* **2022**, *44*. https://doi.org/10.1016/j.nantod.2022.101493.

(302) Chen, Q.; Liu, Y.; Lu, Y.; Hou, Y.; Zhang, X.; Shi, W.; Huang, Y. Atomically Dispersed Fe/Bi Dual Active Sites Single-Atom Nanozymes for Cascade Catalysis and Peroxymonosulfate Activation to Degrade Dyes. *J Hazard Mater* **2022**, *422*. https://doi.org/10.1016/j.jhazmat.2021.126929.

(303) Ma, C. B.; Xu, Y.; Wu, L.; Wang, Q.; Zheng, J. J.; Ren, G.; Wang, X.; Gao, X.; Zhou, M.; Wang, M.; Wei, H. Guided Synthesis of a Mo/Zn Dual Single-Atom Nanozyme with Synergistic Effect and Peroxidase-like Activity. *Angewandte Chemie - International Edition* **2022**, *61* (25). https://doi.org/10.1002/anie.202116170.

(304) Lei, X.; Tang, Q.; Zheng, Y.; Kidkhunthod, P.; Zhou, X.; Ji, B.; Tang, Y. High-Entropy Single-Atom Activated Carbon Catalysts for Sustainable Oxygen Electrocatalysis. *Nat Sustain* **2023**, *6* (7), 816–826. https://doi.org/10.1038/s41893-023-01101-z.

(305) Rao, P.; Deng, Y.; Fan, W.; Luo, J.; Deng, P.; Li, J.; Shen, Y.; Tian, X. Movable Type Printing Method to Synthesize High-Entropy Single-Atom Catalysts. *Nat Commun* **2022**, *13* (1). https://doi.org/10.1038/s41467-022-32850-8.

(306) Liu, Y.; Zhan, L.; Qin, Z.; Sackrison, J.; Bischof, J. C. Ultrasensitive and Highly Specific Lateral Flow Assays for Point-of-Care Diagnosis. *ACS Nano*. American Chemical Society March 23, 2021, pp 3593–3611. https://doi.org/10.1021/acsnano.0c10035.

(307) Wang, W.; Yang, X.; Rong, Z.; Tu, Z.; Zhang, X.; Gu, B.; Wang, C.; Wang, S. Introduction of Graphene Oxide-Supported Multilayer-Quantum Dots Nanofilm into Multiplex Lateral Flow Immunoassay: A Rapid and Ultrasensitive Point-of-Care Testing Technique for Multiple Respiratory Viruses. *Nano Res* **2023**, *16* (2), 3063–3073. https://doi.org/10.1007/s12274-022-5043-6.